MAXIMUM A POSTERIORI VELOCITY ESTIMATION FOR MULTI-FREQUENCY COHERENT DOPPLER SONAR

JEREMY ALAN DILLON


CENTRE FOR NFLD. STUDIES
MEMORIAL UNIVERSITY
OF NEWFOUNDLAND

Maximum A Posteriori Velocity Estimation for Multi-Frequency Coherent Doppler Sonar

by

© Jeremy Alan Dillon

A thesis submitted to the
School of Graduate Studies
in partial fulfilment of the
requirements for the degree of
Doctor of Philosophy

Department of Physics and Physical Oceanography
Memorial University of Newfoundland

August 2011

St. John's Newfoundland

Abstract

Pulse-to-pulse coherent Doppler sonar is a promising tool for measuring near-bed turbulence and sediment transport in energetic environments such as the bottom boundary layer. However, turbulence measurements are limited by measurement noise caused by pulse-to-pulse backscatter decorrelation, and by the requirement to resolve velocity ambiguity in the presence of measurement noise. Existing methods address these limitations separately. This thesis presents an algorithm for velocity estimation that optimally fuses multi-frequency and multi-transducer measurements to simultaneously suppress noise and resolve velocity ambiguity. Data fusion is achieved using a probabilistic approach, whereby measurements are combined numerically to derive a velocity likelihood function evaluated on a discrete grid. Maximum A Posteriori (MAP) estimation is used to produce a velocity time series in which measurement noise is suppressed while high frequency turbulent fluctuations are retained. The algorithm is validated with numerical simulations of a multi-frequency coherent Doppler sonar. Results are presented from a turbulent round jet and a towing tank grid turbulence experiment where both velocity ambiguity and backscatter decorrelation were present. Time series and spectra from MAP velocity estimation are compared to those obtained with conventional Doppler signal processing. In addition to robustly resolving velocity ambiguity, the MAP velocity estimator is shown to lower the noise floor in measured turbulence spectra.

Acknowledgements

Thank you to my advisor, Len Zedel, for the opportunity to work on a project that was ideally suited to my background and interests. Len's MATLAB model taught me more about coherent Doppler sonar than I could learn in any book or journal. His programming style and documentation allowed me to focus clearly on the underlying concepts. Len's door was always open for discussion, debate, or friendly conversation. I particularly enjoyed our discussions in front of his chalkboard.

I thoroughly enjoyed working with Richard Cheel, Alex Hay, and Len Zedel in the Ocean Acoustics Laboratory at Dalhousie University. Together, we overcame numerous technical challenges to achieve a lot in a very short time. Richard and Alex were excellent hosts in Halifax. Our outings to local restaurants and pubs were a fine reward for a long day's work. Wes Paul and Robert Craig deserve special thanks for their role in the development of the multi-frequency Doppler sonar. I very much appreciate their efforts.

Financial support from the Natural Sciences and Engineering Research Council of Canada, the Link Foundation, the IEEE Oceanic Engineering Society, and the School of Graduate Studies at Memorial University is gratefully acknowledged. Without this support, it would not have been possible to pursue this thesis on a full-time basis.

Most importantly, thank you to my family for believing in me. Tracy and Jodie, you make it all worthwhile.

Contents

List of Figures

List of Tables

Nomenclature

The page numbers listed below indicate the place of first reference within the thesis.

Abbreviations

ADCP	Acoustic Doppler Current Profiler, p. 27
FFT	Fast Fourier Transform, p. 178
FIR	Finite Impulse Response, p. 113
LDV	Laser Doppler Velocimetry, p. 25
MAP	Maximum A Posteriori, p. 10
MFDop	Multi-Frequency Doppler Sonar, p. 30
MMSE	Minimum Mean Square Error, p. 23
Nd:YAG	Neodymium-doped Yttrium Aluminum Garnet, p. 120
PDF	Probability Density Function, p. 23
PIV	Particle Image Velocimetry, p. 25
PRF	Pulse Repetition Frequency, p. 19
RMS	Root Mean Square, p. 14
RPM	Revolutions Per Minute, p. 119
SNR	Signal-to-Noise Ratio, p. 17
WSS	Wide-Sense Stationary, p. 13

Symbols

$*$	Complex conjugation, p. 14
α	Parameter for Pearson Type VII distribution, p. 84
β_2	Kurtosis, p. 85
γ	Baseline tilt angle with respect to x-axis, p. 43

Γ	Gamma function, p. 68
δ	"Hit-or-miss" error threshold, p. 36
ϵ	Estimator error, p. 34
ε	Autocorrelation parameter for limit $\rho \to 1$, p. 83
ζ_n	Sample from a complex Gaussian distribution, p. 56
$\boldsymbol{\zeta}$	Vector of samples from a complex Gaussian distribution, p. 57
η	Signal-to-noise ratio, p. 79
θ	Half-angle between transmitter, scatterer, and receiver, p. 39
θ	Unknown parameter, p. 22
$\hat{\theta}$	Estimate of unknown parameter, p. 23
κ	Skewness coefficient for 2D Gaussian distribution, p. 183
λ_0	Wavelength of transmitted sound wave, p. 39
λ_S	Wavelength of scattered sound wave, p. 40
μ	Denominator of asymptotic autocorrelation coefficient, p. 54
$\boldsymbol{\mu}$	Vector of autocorrelation phase and magnitude measurements, p. 37
μ_k	k^{th} moment, p. 85
$\hat{\mu}_k$	k^{th} sample moment, p. 88
ξ_n	Sample from a discrete-time white Gaussian noise process, p. 113
ρ	Autocorrelation coefficient, p. 14
$\hat{\rho}$	Estimated autocorrelation coefficient, p. 15
$\hat{\rho}_\infty$	Asymptotic autocorrelation coefficient, p. 53
σ	Smoothing parameter for the MAP velocity estimator, p. 113
σ^2	Backscatter variance, p. 51
σ_ψ^2	Variance of phase difference, p. 85
σ_f^2	Spectral variance, p. 13
σ_p^2	Equivalent phase variance from Zrnić (1977), p. 79
σ_v^2	Velocity variance, p. 14
σ_x^2	Horizontal velocity variance, p. 46
σ_z^2	Vertical velocity variance, p. 46
τ	Pulse-to-pulse interval, p. 14

ϕ	Autocorrelation phase angle, p. 13
$\hat{\phi}$	Estimated autocorrelation phase, p. 14
ψ	Phase difference, p. 82
a	Argument of single pulse-pair phase distribution, p. 82
$\mathbf{a}$	Vector of quadratic coefficients for Gaussian interpolation, p. 184
a_i	Quadratic coefficients for Gaussian interpolation, p. 182
A	Autocorrelation amplitude, p. 13
c	Speed of sound, p. 11
$\mathcal{C}$	Cost function, p. 34
$\mathbf{C}_\xi$	Covariance matrix of velocity increment, p. 144
$\mathbf{C}_X$	Covariance matrix of real-valued random vector, p. 97
$\mathbf{C}_z$	Backscatter covariance matrix, p. 56
d	Dimension of velocity vector, p. 144
$\mathbf{d}$	Mean particle displacement, p. 177
D	Spacing between elements of turbulence-generating grid, p. 25
E	Expectation operator, p. 23
$\mathcal{E}$	Elliptic integral of the second kind, p. 70
$\mathbf{E}$	Complete elliptic integral of the second kind, p. 54
f_0	Frequency of transmitted sound wave, p. 11
f_D	Doppler frequency shift, p. 12
$\overline{f_D}$	Mean Doppler frequency, p. 13
f_N	Lowest frequency of noise floor, p. 116
f_R	Frequency of received sound wave, p. 11
f_S	Frequency of scattered sound wave, p. 39
F	Hypergeometric function, p. 68
G	Particle image velocimetry Gaussian window function, p. 178
H	Particle image velocimetry high pass filter, p. 178
$\mathbf{H}$	Matrix of coordinates for Gaussian interpolation, p. 184
i	Square root of -1, p. 13
$\mathcal{I}$	Imaginary part, p. 15

$\mathbf{I}$	Identity matrix, p. 57
I_0	Modified Bessel function of the first kind, p. 54
k	Coefficient for Gaussian window width, p. 178
K_0	Modified Bessel function of the second kind, p. 54
L	Number of pulses per ensemble, p. 14
m	Parameter for Pearson Type VII distribution, p. 84
M	Number of pulse-pairs per ensemble, p. 14
N	Time series length, p. 24
N_f	Number of acoustic carrier frequencies, p. 111
N_t	Number of acoustic transducers, p. 143
p	Probability density function, p. 23
p_i	Samples of the likelihood function for Gaussian interpolation, p. 180
p_n^b	Backward time predicted velocity likelihood, p. 114
$\overline{p}_n^b$	Backward time posterior velocity PDF, p. 114
p_n^f	Forward time predicted velocity likelihood, p. 113
$\overline{p}_n^f$	Forward time posterior velocity PDF, p. 113
$\overline{p}_n^s$	Smoother posterior velocity PDF, p. 115
P_{zz}	Backscatter power spectral density, p. 52
$\mathbf{r}_B$	Unit vector directed toward bistatic baseline, p. 38
$\mathbf{r}_j$	Unit vector for bistatic velocity component ($j = 1, 2, 3$), p. 44
$\mathbf{r}_R$	Unit vector directed from scatterer to receiver, p. 38
$\mathbf{r}_T$	Unit vector directed from scatterer to transmitter, p. 38
R	Autocorrelation function, p. 13
R	Bayes risk, p. 34
$\mathcal{R}$	Real part, p. 15
$\mathbf{R}$	Matrix of baseline unit vectors, p. 44
$\hat{R}$	Estimated autocorrelation function, p. 15
R_k	Backscatter autocorrelation sequence, p. 56
t	Time, p. 13
T	Matrix transpose, p. 44

T_o	Period of sinusoidal oscillation, p. 148
T_p	Time between laser pulses, p. 177
u_p	Estimate of the velocity likelihood function peak location, p. 185
$\mathbf{U}$	Cholesky decomposition of autocorrelation matrix, p. 57
v	Radial velocity component, p. 11
$\hat{v}$	Estimate of radial velocity component, p. 111
$\mathbf{v}$	Velocity vector, p. 37
$\hat{\mathbf{v}}$	Estimate of velocity vector, p. 37
v_a	Ambiguity velocity, p. 16
$v_{a_{\mathrm{mf}}}$	Multi-frequency ambiguity velocity, p. 22
v_B	Velocity component toward bistatic baseline, p. 41
v_j	Velocity component toward bistatic baseline ($j = 1, 2, 3$), p. 44
$\mathbf{v}_j$	Vector of velocity components, p. 44
v_p	Estimate of the velocity likelihood function peak location, p. 182
v_x	Horizontal velocity component, p. 44
v_z	Vertical velocity component, p. 44
V	Amplitude of sinusoidal velocity, p. 148
W	Particle image velocimetry window size, p. 178
x	Backscatter real part, p. 51
$\mathbf{x}$	Measurement vector, p. 23
$\mathbf{X}$	Real-valued random vector, p. 96
y	Backscatter imaginary part, p. 51
z	Backscatter (complex value), p. 51
z_n	Backscatter sample, p. 14
$\mathbf{z}$	Vector of backscatter samples, p. 56

Chapter 1

Introduction

1.1 Motivation

The ocean has been described as Earth's "final frontier" in a vision statement on ocean exploration (National Oceanic and Atmospheric Administration, 2000). The search for new insight and understanding is motivated by the fact that our environmental and economic security depends critically on the ocean and the freshwater bodies that drain into it. As the vast majority of the ocean is unknown and unexplored, there is great potential for scientific discovery beneath the sea surface (McNutt, 2002). The development of remote and *in situ* sensors forms a cornerstone of this vision for exploring ocean dynamics and interactions at new scales.

It has long been known that sound waves propagate well in water, whereas light and other electromagnetic waves attenuate rapidly with depth (Urick, 1983, chap. 1). The backscatter, or echo, from transmitted underwater sound contains information about the location, size, distribution, and velocity of objects and organisms either

suspended in the water column or resting on the seabed. Analysis of underwater sound propagation can also be used to infer properties of the medium, such as its temperature, drift speed, and stratification, as well as geophysical properties of the seabed (Medwin and Clay, 1998, chap. 1). Underwater acoustics is therefore an ideal tool for remote sensing in the ocean and in freshwater bodies such as lakes, rivers, and streams.

Pulse-to-pulse coherent Doppler sonar has been widely used to study transport and mixing processes in the ocean. Examples include tidal flows (Lhermitte, 1983; Lu and Lueck, 1999a; Souza et al., 2004), surface boundary layer processes (Gargett, 1989), surface wave breaking (Veron and Melville, 1999; Gemmrich and Farmer, 2004), internal waves (Plueddemann, 1992; Scotti and Pineda, 2004; Bourgault et al., 2007), sediment transport (Smyth et al., 2002; Williams et al., 2003), and turbulence measurement (Lohrmann et al., 1990; Stacey et al., 1999; Trowbridge and Elgar, 2001; Rippeth et al., 2002). High frequency (1 to 10 MHz) coherent Doppler sonar is a promising tool for obtaining near-bed profiles of shear stress and sediment flux in the ocean bottom boundary layer (Grant and Madsen, 1986; Thorne and Hanes, 2002). Recent studies have focused on the estimation of bottom friction from near-bed turbulence profiles (Smyth and Hay, 2003; Newgard and Hay, 2007; Hay, 2008). Coherent Doppler sonar has also been used in freshwater applications such as river discharge measurement (Lane et al., 1998), open channel flow (Lhermitte and Lemmin, 1994; Voulgaris and Trowbridge, 1998), and the study of internal waves in lakes (Umlauf and Lemmin, 2005).

The performance and limitations of coherent Doppler sonar have been extensively explored through numerical simulations (Mo and Cobbold, 1992; Zhang et al., 1994;

Zedel, 2008) and in the laboratory (Garbini et al., 1982b; Zedel et al., 1996; Lemmin and Rolland, 1997; Voulgaris and Trowbridge, 1998; Zedel and Hay, 1999; Veron and Melville, 1999; Zedel and Hay, 2002). Measurement errors have been found to be caused by pulse-to-pulse backscatter decorrelation from (i) scatterer advection through the sample volume, (ii) velocity shear and turbulence within the sample volume, (iii) phase distortion of the transmitted wave, and (iv) electronic noise in the receiver circuitry (Zedel et al., 1996; Hurther and Lemmin, 2001). Measurement errors introduce biases when calculating turbulence statistics from the fluctuating component of velocity measurements (Lu and Lueck, 1999b; Hay, 2008). Coherent Doppler sonar measurements are also limited by the existence of range and velocity ambiguities (Lhermitte and Serafin, 1984). In particular, velocity aliasing occurs when the radial component of scatterer velocity exceeds one quarter wavelength per pulse-to-pulse interval (a Nyquist sampling criterion).

Multi-frequency coherent Doppler sonar is a recent development where multiple acoustic carrier frequencies are transmitted simultaneously using a wide bandwidth acoustic transducer. Measurements from multiple receiver channels can be combined to resolve velocity ambiguity and reduce measurement errors. In medical ultrasound, a multi-frequency approach has been used for both noise reduction (Eriksson et al., 1995) and velocity ambiguity resolution (Nitzpon et al., 1995). A profiling sonar developed for sediment transport applications employs four carrier frequencies and five acoustic transducers (Hay et al., 2008). Multi-frequency acoustic backscatter has also been used to infer the concentration and size of suspended sediment particles (Hay, 1991; Hay and Sheng, 1992). Thus, multi-frequency coherent Doppler sonar has the potential to obtain simultaneous profiles of sediment velocity, concentration,

and particle size using a single instrument.

The use of multiple carrier frequencies in coherent Doppler sonar produces redundant velocity measurements. For example, the sonar described in Hay et al. (2008) collects twenty Doppler measurements for three independent components of velocity. An optimal algorithm for velocity estimation would extract all of the information available in redundant Doppler measurements while simultaneously resolving velocity ambiguity and attenuating measurement noise. Optimal velocity estimation would be especially useful for measurements in highly turbulent flow exhibiting backscatter decorrelation and velocity ambiguity.

The estimator presented in this thesis has been developed with the aim of improving instrumentation for studying near-bed turbulence and sediment dynamics in coastal areas. New instrumentation capabilities would also benefit researchers in related fields since transport processes in the benthic boundary layer are of biological, chemical, and geophysical importance (Lisle, 1989; Boudreau and Jørgensen, 2001; Jackson et al., 2002). Velocity ambiguity and measurement noise are also present in Doppler weather radar (Doviak et al., 1979), coherent Doppler lidar (Menzies and Hardesty, 1989), and medical ultrasound (York and Kim, 1999). New methods for multi-frequency Doppler signal processing may benefit these related fields as well.

1.2 Background

1.2.1 Sediment transport

The study of sediment transport in water sheds light on many forces that have shaped the Earth's topography. As rivers empty into the ocean, they deposit large quantities of sediment, forming river deltas that are rich in topsoil. These regions have supported some of the earliest civilizations such as the Egyptians at the Nile River delta and the Chinese at the Yangtze River delta (Graf, 1971). Even today these regions remain some of the most fertile on the planet. On geological time scales, sediment transport determines the evolution of river beds, estuaries, and coast lines.

Sedimentation plays a significant role in many present day engineering endeavours (Chien and Wan, 1999). Deposition of sediment in harbours and waterways reduces shipping capacity and leads to increased dredging costs. In many parts of the world, irrigation canals are indispensable for agriculture. Sedimentation in canal systems decreases irrigation capacity over time. Reservoirs built for flood control and hydroelectric power generation also lose capacity due to accumulation of sediment. Recognition of the effects of sediment transport has led to soil conservation practices and changes to design processes used in civil engineering (Shalash, 1982).

When sediment transport is measured, the total transport is often divided into three components: wash load, bed load, and suspended load (Fredsøe and Deigaard, 1992, chap. 7). Wash load consists of very fine particles that are carried by the flow essentially in permanent suspension. Thus, particles in the wash load may be of a different composition than the bed material since there is little to no interaction with

the bottom. It is useful to think of wash load as part of the fluid (such as water vapour in air) and neglect its contribution when considering entrainment, transport, and deposition. Bed load, in contrast, consists of much larger particles that roll or slide along in continuous contact with the bed. Dynamics of the bed load are primarily determined by shear stress of the flow acting on the bed. Suspended load consists of intermediate size particles that make intermittent contact with the bottom. Fluid turbulence serves to dislodge particles from the bed into the suspended load, where they are transported some distance before being deposited downstream.

Empirical correlations for predicted bed load and suspended load have been developed under idealized conditions in the laboratory. For example, an experiment might consider steady flow over a flat bed of uniform particles (Van Rijn, 1984). However, there are several complicating factors in a natural environment such as a river or coastal area. Flow may at times be unsteady, the bed may be uneven or sloped, particles may vary widely in composition and size, and sediment transport may be complicated by wave action in addition to steady fluid flow (Nielsen, 1992, chap. 1). Therefore, correlations developed in the laboratory provide at best a rough prediction of sediment transport in a natural environment. Direct measurement is necessary to obtain accuracy better than an order of magnitude approximation (Grant and Madsen, 1986).

1.2.2 Measurement techniques

Measurement techniques for sediment transport can be divided into *in situ* measurements and remote sensing techniques. *In situ* measurements consist of inserting a

probe or sensor into the flow to intercept sediment particles in a localized sampling region. Remote sensing techniques, on the other hand, encompass non-intrusive measurements such as optical or acoustic methods.

Mechanical instruments are often used to measure transport in the suspended load (Van Rijn, 2007, chap. 5). The challenge in making accurate measurements arises from the fact that a probe will inevitably disturb the flow. The probe must be designed so that the intake velocity matches the (possibly unknown) local flow velocity. Therefore, any probe will only make accurate concentration measurements over a limited range.

Optical sensors operate under the principle that suspended sediment particles will scatter light that is transmitted into the water. The principal advantage of optical sensors is that they provide a means of obtaining a time history of concentration without disturbing the flow at the point of measurement, which is a significant advantage compared to mechanical instruments. Optical transmission and optical backscatter sensors transmit light from a high-intensity source into the water and measure the intensity of light transmitted through a sample volume or backscattered from a sample volume using a photodetector. Calibration is required to relate intensity measurements at the photodetector to either the mass or volume concentration of sediment particles.

Optical backscatter sensors are particularly useful for sediment concentration measurement since the transmitter and detector can be combined in a single sensor head, resulting in a compact measurement unit. By time-gating the signal from the photodetector, the sensor can be tuned to operate over a large range of distances. Optical devices have been found to be reliable since there are no moving parts and

no small ports or nozzles that could clog easily.

The main disadvantage of optical backscatter (and transmission) sensors is that calibration strongly depends on particle size (Van Rijn, 2007, chap. 5). Calibration for each experiment or field trial must be performed for the expected particle size in the flow. This means that optical backscatter sensors are not well-suited to flows containing a wide range of sediment particle sizes (such as a mixture of clay, silt, and sand). Also, a sufficient number of scatterers must be present to produce a signal that exceeds the noise level of the photodetector.

Acoustic sensors operate in a similar fashion as optical sensors in that energy is transmitted into the flow, scattered from sediment particles, and measured by a detector. The speed of sound in water is approximately 1500 m s^{-1}, compared to 3×10^8 m s^{-1} for light. Due to the relatively low propagation speed of acoustic energy, it is possible to sample backscatter intensity sufficiently quickly to give a profile of concentration versus range. Thus, acoustic sensors are especially useful for boundary layer studies where it is of interest to measure the concentration profile as a function of height above the bed (Thorne and Hanes, 2002).

A second limitation of optical backscatter sensors is that they only provide a measurement of sediment concentration. In order to calculate the rate of sediment transport, it is necessary to know or measure the flow velocity through the sample volume. A flow meter or velocity probe placed into the flow may disturb the flow of sediment through the sample volume, or it may interfere with optical measurement of concentration. With an acoustic sensor, backscatter intensity is related to sediment concentration, while the Doppler shift of the transmitted waveform is related to the mean particle velocity. Furthermore, intensity and Doppler shift may be sampled

simultaneously to determine the instantaneous sediment flux.

The Doppler shift is a change in backscatter frequency (as compared to the transmitted frequency) caused by particles moving toward or away from the transmitter and receiver. A commonly used configuration consists of a stationary sensor measuring the speed of particles transported by a moving fluid. However, the sensor platform may also be moving, for example in the case of shipborne measurements. In all cases, the sensor measures the *relative* motion between the transmitter, scatterers, and receiver. In order to measure the magnitude and direction of sediment flux in a transverse flow, it is necessary to employ a minimum of three acoustic beams oriented independently to resolve three spatial components of velocity. For example, a Doppler velocimeter manufactured by Nortek uses four convergent beams to measure backscatter intensity and three components of velocity in a small sample volume (Nortek, 2009).

Acoustic sensors have two more advantages: they are rugged, and they can profile right up to a boundary such as the seabed. This makes it possible to collect acoustic sediment transport measurements in harsh environments. For example, in the tidal inlet experiment described in Williams et al. (2003), acoustic sensors were used to measure velocity while separate acoustic backscatter sensors were employed to measure concentration. Since acoustic sensors can operate without interference in different frequency ranges, it is possible to choose an operating frequency for each sensor that is optimal for the task at hand (e.g. velocity or concentration measurement).

For the majority of sand and silt particles in suspension, the acoustic wavelength is greater than the particle diameter. Lower frequency sensors can be used to measure the concentration of larger particles in suspension. Like optical sensors, calibration

is required to relate backscatter intensity to concentration. Multi-frequency acoustic systems have been developed to account for flows containing a distribution of particle sizes by exploiting the frequency dependence of the scattering cross section (Hay and Sheng, 1992), e.g. f^4 for Rayleigh scattering (Pierce, 1989, chap. 9). At high frequencies, the scattering cross section approaches the projected area of the particle whereas acoustic absorption in water increases as f^2 (Medwin and Clay, 1998, chap. 3). Thus, frequencies higher than 10 MHz are not often used in acoustic sensing of sediment transport due to the increasingly high absorption of acoustic energy at high frequency.

1.3 Literature review

Many of the signal processing techniques used in coherent Doppler sonar were originally developed for Doppler weather radar. Coherent Doppler systems have also been actively developed within the biomedical engineering community. This literature review therefore draws upon references from the fields of weather radar and medical ultrasound in addition to research that has been performed in oceanography and hydraulic engineering.

Methods for estimating mean scatterer velocity from observed Doppler frequency spectra are described in Section 1.3.1. In particular, the commonly used covariance method is discussed in detail, along with some of its limitations. Previous studies concerning improved Doppler velocity estimation have focused on noise suppression and velocity ambiguity resolution. These techniques are reviewed in Sections 1.3.2 and 1.3.3, respectively. Although Maximum A Posteriori (MAP) velocity estimation for Doppler sonar is a novel concept, there are similarities with other applications

of Bayesian estimation such as Kalman filtering, the forward-backward algorithm for hidden Markov models, and belief propagation. These related topics are reviewed in Section 1.3.4. In this thesis, performance of the MAP velocity estimator is evaluated via laboratory observations of grid turbulence and a turbulent jet. These flows have been extensively studied both theoretically and experimentally. Their significant properties are summarized in Section 1.3.5.

1.3.1 Doppler velocity estimation

A backscatter sonar transmits an acoustic signal into the water and records the backscatter, or echo, from particles, bubbles, and organic matter suspended in the water column. When scatterers are moving with radial speed v toward the sonar, the Doppler effect causes a transmitted acoustic wave of frequency f_0 to return as an echo with received frequency f_R given by (Medwin and Clay, 1998, chap. 3)

$$f_R = f_0 \left(\frac{c+v}{c-v} \right) \tag{1.1}$$

where c is the speed of sound wave propagation (approximately 1500 m s^{-1} in water). For the present discussion of basic concepts, the simple backscatter geometry of a collocated transmitter and receiver is considered. In Section 2.2, a more general version of (1.1) is derived for the case of a bistatic geometry (i.e. separated transmitter and receiver). For oceanographic applications, the speed v is typically on the order of 1 m s^{-1}. Therefore, (1.1) can be approximated with a Taylor series

$$\frac{1+x}{1-x} \approx 1 + 2x + \mathcal{O}(x^2) \tag{1.2}$$

when $x \ll 1$. Letting $x = v/c$ and retaining only first order terms yields

$$f_R = f_0 \left(1 + \frac{2v}{c}\right). \tag{1.3}$$

Equation (1.3) may be written in terms of the Doppler frequency shift $f_D = f_R - f_0$,

$$f_D = f_0 \frac{2v}{c}. \tag{1.4}$$

Scatterer velocity can therefore be determined by measuring the Doppler frequency shift of the received signal via

$$v = \frac{c}{2f_0} f_D. \tag{1.5}$$

Fourier analysis is one tool which is commonly used to examine the frequency content of a signal. Spectral estimation has also been performed using time domain methods (Woodman and Hagfors, 1969; Dotti et al., 1976; Barber et al., 1985; Bonnefous et al., 1986) and autoregressive parameter estimation (Marple, 1980; Ahn and Park, 1991). The performance and merits of various spectral estimation techniques have been compared for applications in Doppler weather radar (Sirmans and Bumgarner, 1975), coherent Doppler sonar (Lhermitte and Serafin, 1984), and medical ultrasound (Vaitkus and Cobbold, 1988; Vaitkus et al., 1988; David et al., 1991). For applications in oceanography and hydraulic engineering, the covariance method (Miller and Rochwarger, 1972) has been widely used due to its low computational complexity and unbiased estimation in the presence of white noise (Lhermitte and Lemmin, 1994).

Miller and Rochwarger (1972) analyzed the performance of the covariance method

in the presence of additive Gaussian noise. The backscatter signal was modelled as a complex Gaussian wide-sense stationary (WSS) stochastic process with autocorrelation function $R(t)$. The mean Doppler frequency $\overline{f_D}$ and spectral variance σ_f^2 of the signal were shown to be related to the autocorrelation function as follows:

$$\overline{f_D} = \frac{1}{2\pi i}\frac{\dot{R}(0)}{R(0)}, \tag{1.6}$$

$$\sigma_f^2 = -\frac{1}{4\pi^2}\left[\frac{\ddot{R}(0)}{R(0)} - \left(\frac{\dot{R}(0)}{R(0)}\right)^2\right]. \tag{1.7}$$

When the autocorrelation function is written in polar form

$$R(t) = A(t)\, e^{i\phi(t)} \tag{1.8}$$

where A and ϕ represent the amplitude and phase (in radians), respectively, the mean Doppler frequency and spectral variance take the form

$$\overline{f_D} = \frac{\dot{\phi}(0)}{2\pi}, \tag{1.9}$$

$$\sigma_f^2 = -\frac{1}{4\pi^2}\frac{\ddot{A}(0)}{A(0)}. \tag{1.10}$$

An alternative to direct measurement of Doppler frequency is the pulse-to-pulse coherent approach, where the sonar transmits acoustic pulses with constant phase offset. In actuality, pulsed Doppler systems measure changes in particle displacement rather than a frequency shift described by the classical Doppler effect (Cobbold, 2007, chap. 10). However, scatterer motion causes a shift in the mean frequency of

the pulse-to-pulse time series with the same velocity-frequency relationship as in (1.4) (Newhouse and Amir, 1983; Thomas and Leeman, 1993).

Thus, the pulse-to-pulse autocorrelation of the backscatter signal may be measured to approximate (1.9) and (1.10) with finite differences

$$\overline{f_D} \approx \frac{\phi(\tau) - \phi(0)}{2\pi\tau} = \frac{\phi}{2\pi\tau}, \tag{1.11}$$

$$\sigma_f^2 \approx \frac{1}{2\pi^2\tau^2}\left[1 - \frac{A(\tau)}{A(0)}\right] = \frac{1-\rho}{2\pi^2\tau^2}. \tag{1.12}$$

The time interval between successive pulses is denoted by τ. When written with no time dependence, ϕ denotes autocorrelation phase evaluated at a lag of τ. Also, ρ denotes the normalized autocorrelation coefficient $A(\tau)/A(0)$. With these approximations, radial velocity and its corresponding RMS uncertainty σ_v are given by

$$v = \frac{c}{4\pi f_0 \tau}\phi, \tag{1.13}$$

$$\sigma_v = \frac{c}{4\pi f_0 \tau}\sqrt{2(1-\rho)}. \tag{1.14}$$

In practice, autocorrelation is estimated from complex-valued backscatter samples $z_1, \ldots, z_L$ corresponding to an ensemble of $M = L - 1$ pulse-pairs (Zrnić, 1977),

$$R(\tau) \approx \hat{R}(\tau) = \frac{1}{M}\sum_{n=1}^{M} z_n^* z_{n+1} \tag{1.15}$$

where * denotes complex conjugation. The phase $\hat{\phi}$ of the autocorrelation estimate

$\hat{R}(\tau)$ is determined from real and imaginary components as follows:

$$\hat{\phi} = \angle \hat{R}(\tau) = \tan^{-1} \frac{\mathcal{I}(\hat{R}(\tau))}{\mathcal{R}(\hat{R}(\tau))}. \tag{1.16}$$

Also, the autocorrelation magnitude can be estimated as (Zedel et al., 1996)

$$\hat{\rho} = \frac{\left| \sum_{n=1}^{M} z_n^* z_{n+1} \right|}{\sum_{n=1}^{M} |z_n^* z_{n+1}|}. \tag{1.17}$$

The triangle inequality ensures that $0 \leq \hat{\rho} \leq 1$.

One limitation of the covariance method is that, strictly speaking, finite difference approximations in (1.11) and (1.12) are only valid in the limit $\tau \to 0$. However, the pulse transmission interval cannot be made arbitrarily small. Range measurements become ambiguous if backscatter at a given time is due to echoes from two or more acoustic transmissions. When range ambiguity is addressed, for example with phase-coded pulses (Sachidananda and Zrnić, 1999), the requirement for v to be finite in (1.13) implies that $\phi \to 0$ as $\tau \to 0$. Therefore, measurement errors in the phase resolving circuitry of the sonar become large relative to ϕ, causing the RMS velocity error to vary as $1/\tau$ (Zedel et al., 1996).

A long pulse-to-pulse interval, on the other hand, exacerbates the problem of backscatter decorrelation. Equation (1.14) predicts that velocity uncertainty will increase in the presence of backscatter decorrelation, as quantified by $1 - \rho$. An increase in measurement noise due to backscatter decorrelation has been quantified experimentally (Zedel et al., 1996).

Another limitation of the covariance method is that the autocorrelation phase

angle can only be measured modulo 2π radians. For example, a phase angle interval of $[-\pi, \pi]$ in (1.13) implies an ambiguity velocity v_a of (Lhermitte and Serafin, 1984)

$$v_a = \frac{c}{4f_0\tau}. \tag{1.18}$$

In other words, scatterer velocities of v_a and $-v_a$ are indistinguishable since the corresponding phase shifts of π and $-\pi$ are equivalent. Velocity ambiguity is a characteristic of coherent Doppler systems (whether or not the covariance method is used) since the Doppler frequency spectrum is sampled at a rate of $1/\tau$ samples per second. Therefore, Doppler frequencies can only be measured unambiguously up to the Nyquist frequency (Mitra, 1998, chap. 5)

$$|f_D| \leq \frac{1}{2\tau} \tag{1.19}$$

which is equivalent to (1.18) due to the velocity-frequency relationship expressed in (1.5).

1.3.2 Measurement noise suppression

Doppler measurement errors consist of both intermittent spurious measurements ("spikes") and continuous random fluctuations ("noise"). Spikes tend to be relatively rare and obviously distinct from good data, whereas noise is ubiquitous and difficult to separate from real fluctuating measurements. Both types of errors cause the measured velocity variance to exceed the true variance of scatterer velocity. In order to obtain accurate statistics, for example in turbulence measurement, it is necessary to suppress

both spikes and noise. Averaging and low pass filtering can be applied to attenuate measurement errors. However, there is a corresponding reduction in effective sample rate and bandwidth. The methods described below aim to improve velocity estimates while preserving the sample rate and bandwidth of the original data.

"Despiking" consists of identifying spurious measurements and replacing these values with interpolated data. For example, in a surf zone experiment (Elgar et al., 2005), empirical thresholds were applied to reject Doppler velocimeter measurements based on low values of signal-to-noise ratio (SNR), autocorrelation coefficient, and correlation with a collocated pressure sensor. In another application, coherent Doppler sonar observations of near-bed turbulence were subject to a despiking algorithm that rejected on average 2% of the measurements (Hay, 2008). Many heuristic despiking algorithms are simple yet effective; however, there is always the potential to miss some spikes or to inadvertently remove valid data points. In an approach known as phase-space thresholding (Goring and Nikora, 2002), velocity measurements and their first and second derivatives (as estimated from time series differencing) were represented as points in a three-dimensional space. Standard deviations of all three variables were used to define an ellipsoidal threshold surface where points lying outside the ellipsoid were replaced using cubic interpolation of the time series. When phase-space thresholding and four other despiking algorithms were applied to a contaminated data set, the resulting standard deviation was found to depend strongly on the method that was used.

Doppler noise suppression can be achieved when redundant measurements with uncorrelated measurement errors are available. An example of this approach is the use of two partially overlapping or non-overlapping sample domains (Garbini et al.,

1982a). Velocity measurements from two closely spaced regions along the acoustic beam were cross-correlated to attenuate uncorrelated noise sources. When sample regions overlapped, noise sources were partially correlated and therefore only partially attenuated. In turbulent flow, spatial decorrelation of velocity limits the allowable sample volume separation. Although the spatial cross-correlation method was shown to improve velocity measurements for a single beam sonar (Garbini et al., 1982b), the method has not been widely used for configurations employing multiple receivers.

Redundant measurements with uncorrelated errors may also be obtained with additional acoustic receivers. By using four receivers to measure three components of velocity, redundant vertical velocity calculations have been used to reduce the noise contribution in turbulence statistics (Hurther and Lemmin, 2001). With a refinement of this approach that determines redundant values for each receiver, an order of magnitude noise level reduction was demonstrated compared to uncorrected measurements (Blanckaert and Lemmin, 2006). Noise reduction for one-dimensional flow has also been considered by placing two receivers at different angles to the flow. In a simulation of Doppler ultrasound, noise sources were found to decorrelate when the receivers were oriented as little as 5° apart (Jones and Krishnamurthy, 2002). Redundant receivers have also been used in four-beam acoustic Doppler current profilers (Rowe et al., 1986) and a five-transducer profiling sonar (Hay et al., 2008).

Another method for obtaining redundant velocity measurements with uncorrelated noise sources involves simultaneous transmission of two closely spaced acoustic carrier frequencies (Hurther and Lemmin, 2008). Experiments in oscillating grid turbulence showed that a carrier frequency shift of 10% was sufficient to achieve an order of magnitude in noise suppression.

1.3.3 Velocity ambiguity resolution

As discussed in Section 1.3.1, velocity ambiguity is related to the Nyquist sampling criterion when a frequency shift due to scatterer motion is measured. In principle, velocity estimators base on time domain cross-correlation are not limited by velocity ambiguity (Bonnefous et al., 1986). However, in practice, the maximum achievable velocity is limited since correlation methods are prone to artifacts arising from false peaks in the cross-correlation function (Jensen, 1993).

Aliasing errors produce spurious data artifacts when the autocorrelation phase jumps discontinuously by $\pm 2\pi$. Consequently, unresolved velocity ambiguity leads to overestimation of the velocity variance in turbulence measurement. When using the covariance method for mean frequency estimation, velocity ambiguity may be avoided by choosing a sufficiently short pulse-to-pulse interval, or it may be resolved using existing methods from any of the following four categories: (i) temporal continuity, (ii) spatial continuity, (iii) staggered pulse repetition frequency (PRF), and (iv) multiple carrier frequencies.

From (1.13), autocorrelation phase is related to the pulse-to-pulse interval τ by

$$\phi = 4\pi f_0 \tau \frac{v}{c}. \tag{1.20}$$

Therefore, velocity ambiguity may be avoided by choosing τ to be sufficiently small so that phase is constrained to lie within the interval $[-\pi, \pi]$. However, a short pulse interval often results in range ambiguity. As discussed in Section 1.3.1, a short pulse interval also exacerbates the Doppler noise problem. When velocities are slowly

time-varying, as in many current measurement applications, averaging can be used to obtain satisfactory noise suppression.

Velocity ambiguity may be resolved by invoking the assumption that the velocity field is continuous in time and space. When using the covariance method, multiples of 2π have been added to the autocorrelation phase to minimize discontinuities in time (Smyth and Hay, 2003), space (Bergen and Albers, 1988; Eilts and Smith, 1990; Tabray et al., 2001; Gong et al., 2003; Gao and Droegemeier, 2004), or both simultaneously (Veron and Melville, 1999; James and Houze, 2001; Franca and Lemmin, 2006). In medical ultrasound applications employing the Fourier transform, ambiguous Doppler spectra have been successfully corrected by tracking changes in time (Tortoli, 1989) and across spatial samples (Torp and Kristoffersen, 1995). Two difficulties arise in applying temporal and spatial continuity methods. First, the algorithm must be initialized at a point where velocity is unambiguous, such as near a solid boundary. Otherwise, a constant offset might remain even though discontinuities have been eliminated. Second, the autocorrelation phase or Doppler spectrum may change rapidly if the flow is highly sheared or turbulent, or if a burst of low quality data is recorded (for example, in pockets of low scatterer concentration). Continuity methods therefore frequently suffer from a lack of robustness under highly time-varying conditions.

Another method for velocity ambiguity resolution involves varying the pulse-to-pulse interval τ to obtain two or more staggered pulse repetition frequencies. The covariance method is applied to each data stream separately. From (1.20), the phase

ϕ_i and pulse interval τ_i for each data stream are related by

$$\phi_i = 4\pi f_0 \tau_i \frac{v}{c}. \tag{1.21}$$

When values ϕ_i are measured in a fixed interval such as $[-\pi, \pi]$, multiple offsets of 2π can be determined to best satisfy the linear relationship in (1.21). A dual-PRF approach has been widely used in Doppler weather radar (Doviak et al., 1979; Holleman and Beekhuis, 2003; Joe and May, 2003) and coherent Doppler sonar (Lhermitte and Serafin, 1984; Lohrmann et al., 1990). The main disadvantage with dual- and multi-PRF schemes is that additional sampling time is required, thus lowering the maximum achievable sample rate. Another difficulty arises if large measurement errors obscure the correct linear fit to (1.21).

The multi-frequency approach to velocity ambiguity resolution involves transmitting pulses with multiple carrier frequencies. As in the staggered PRF method, the covariance method may be applied to each data stream separately to obtain phase shifts ϕ_i proportional to carrier frequencies f_i,

$$\phi_i = 4\pi f_i \tau \frac{v}{c}. \tag{1.22}$$

Once again, velocity ambiguity may be resolved by determining phase offsets to best satisfy the linear relationship in (1.22). One advantage compared to the staggered PRF method is that multiple carrier frequencies can be transmitted simultaneously using a wide bandwidth transducer so that there is no sample rate reduction. Multi-frequency coherent Doppler sonar has been used in medical ultrasound (Nitzpon et al.,

1995) and in a profiling sonar developed for sediment transport applications (Hay et al., 2008). For two carrier frequencies $f_i < f_j$, (1.22) implies that

$$v = \frac{c\,(\phi_j - \phi_i)}{4\pi(f_j - f_i)\tau} = \frac{c}{4\pi\tau}\frac{\Delta\phi}{\Delta f}. \tag{1.23}$$

If the phase difference $\Delta\phi$ is constrained to lie in the interval $[-\pi, \pi]$, the multi-frequency ambiguity velocity is given by

$$v_{a_{mf}} = \frac{c}{4\tau\Delta f} \tag{1.24}$$

where Δf is the frequency difference $f_j - f_i$. Letting f_0 denote the nominal centre frequency of the acoustic transducer, (1.24) represents an ambiguity velocity improvement by a factor of $f_0/\Delta f$ compared to (1.18). Extensions to multiple (i.e. more than two) frequencies have been developed based on nonlinear least squares estimation (Zhang et al., 2004), adaptive filtering (Zhang et al., 2005), and by phase extrapolation based on the slope $\Delta\phi/\Delta f$ (Zedel and Hay, 2010). As noted in Zedel and Hay (2010), the ambiguity limit cannot be raised arbitrarily in the limit $\Delta f \to 0$ since, in practice, phase measurements are corrupted with noise.

1.3.4 Bayesian estimation

Maximum A Posteriori (MAP) estimation is one of several parameter estimation methods based on Bayesian inference (Kay, 1993, chap. 10). In contrast with classical statistical estimation, Bayesian methods treat a parameter θ to be estimated as a random variable rather than a deterministic but unknown constant (Box and Tiao, 1973).

The motivation for the Bayesian approach is that prior knowledge of the probability density function (PDF) $p(\theta)$ may be used to improve estimator performance. Once observations $\mathbf{x}$ have been made, Bayes' theorem permits calculation of the posterior PDF $p(\theta \mid \mathbf{x})$ which expresses the likelihood of a particular value of θ given that $\mathbf{x}$ have been observed. The estimated value $\hat{\theta}$ is then calculated as a function of the posterior PDF, for example as the posterior mean, median, or maximum value.

The MAP velocity estimator developed in this thesis shares many conceptual similarities with Kalman filtering. A Kalman filter is a sequential estimator that combines measurements with prior knowledge from a linear dynamic model to achieve a minimum mean square error (MMSE) optimal estimate (Kalman, 1960). In the discrete-time *filtering problem*, the time-varying parameter θ_n is estimated from measurements $\mathbf{x}_1, \ldots, \mathbf{x}_n$. A useful property of the Kalman filter is that the estimate $\hat{\theta}_{n-1}$ incorporates all of the information contained in the measurements $\mathbf{x}_1, \ldots, \mathbf{x}_{n-1}$. The estimator may therefore be implemented in the recursive form $\hat{\theta}_n = E(\theta_n \mid \hat{\theta}_{n-1}, \mathbf{x}_n)$ where E is the expectation operator. A dynamic model is used to generate a prediction of θ_n from $\hat{\theta}_{n-1}$ which is then corrected by the measurement $\mathbf{x}_n$. For each iteration in the sequence, the filter produces its own performance measure via the estimated covariance of $\hat{\theta}$. If the unknown parameter and measurement noise are assumed to have a jointly Gaussian PDF, the Kalman filter can be interpreted as a Bayesian MMSE estimator (Meinhold and Singpurwalla, 1983). Alternatively, if only the first and second moments (mean and covariance) of the PDF are specified, then the Kalman filter is optimal in the class of linear estimators (Kay, 1993, chap. 13).

Like any other causal filter, the Kalman filter tends to exhibit estimator lag when tracking a time-varying parameter. If estimation can be deferred until all measure-

ments have been collected, then the *smoothing problem* can be solved to estimate θ_n from $\mathbf{x}_1, \ldots, \mathbf{x}_N$ where $n \leq N$. A Kalman smoother can be implemented by combining the result from a forward filter operating on the measurements $\mathbf{x}_1, \ldots, \mathbf{x}_n$ with the output of a filter operating backward in time on the measurements $\mathbf{x}_N, \ldots, \mathbf{x}_n$ (Fraser and Potter, 1969). Together, the forward and backward filters use all of the available data to optimally estimate θ_n. The corresponding smoother uncertainty is less than that obtained by forward or backward filtering alone (Gelb, 1974, chap. 5).

Two other Bayesian estimation methods related to MAP velocity estimation are the forward-backward algorithm for hidden Markov models (Rabiner and Juang, 1986) and belief propagation (Pearl, 1986). Like the Kalman smoother, the forward-backward algorithm separately processes measurements forward from $\mathbf{x}_1$ to $\mathbf{x}_N$ and backward from $\mathbf{x}_N$ to $\mathbf{x}_1$. The results from each pass are then combined to calculate the probability of the measurement sequence given an underlying hidden Markov model. Belief propagation is a message passing algorithm for network-based models consisting of random variable nodes in a graph. Relationships between variables are quantified via conditional probabilities along edges of the graph. For example, measurements of a velocity time series could be modelled using a graph of nodes connected in a line segment to express their temporal relationship. In the initialization phase of belief propagation, prior knowledge and nodal measurements are used to define an initial belief function that expresses the likelihood of a particular state. Conditional probability "messages" are then passed iteratively between nodes until the network converges to a most likely state. In addition to its original applications in information theory and artificial intelligence, belief propagation has been used for surface reconstruction in computer vision (Petrovic et al., 2001) and bathymetric

synthetic aperture sonar (Barclay et al., 2003; Hayes and Barclay, 2003). Conditional probabilities between nodes (i.e. image pixels) express the expected continuity of the physical surface.

1.3.5 Grid turbulence and the turbulent round jet

In laboratory turbulent flows, prior experimental results are available for comparison with coherent Doppler sonar. For example, grid turbulence has been studied extensively using hot-wire anemometry (Taylor, 1935b; Batchelor and Townsend, 1947; Comte-Bellot and Corrsin, 1966; Mohamed and LaRue, 1990), laser Doppler velocimetry (LDV) (George and Lumley, 1973), and particle image velocimetry (PIV) (Westerweel et al., 1997). Likewise, the turbulent round jet has been studied using hot-wire anemometry (Gibson, 1963; Wygnanski and Fiedler, 1969; Crow and Champagne, 1971; Panchapakesan and Lumley, 1993), hot-film anemometry (Zedel and Hay, 1999), LDV (Hussein et al., 1994), and PIV (Westerweel et al., 2002).

Grid turbulence is formed by passing a steady flow through a rectangular grid of wires or bars spaced a distance D apart. Within a downstream distance of approximately $20D$, wakes from individual grid elements merge to form a turbulent flow that is approximately isotropic and homogeneous, and therefore amenable to theoretical analysis (Taylor, 1935a). In the "initial period" of decay beginning at $20D$ (Batchelor and Townsend, 1948a), turbulent kinetic energy decays downstream according to a universal self-similar power law independent of Reynolds number, mesh size, solidity, grid rod shape, and surface roughness (Mohamed and LaRue, 1990). In the "final period" of decay beyond a distance of approximately $400D$, inertial forces become

negligible and viscous forces dominate. The final period of decay has also been shown to exhibit self-similar behaviour (Batchelor and Townsend, 1948b).

Discharge from a round jet into an ambient fluid produces a turbulent flow that is statistically stationary and axisymmetric. Symmetry dictates that Reynolds shear stresses are zero on the jet centre line. Throughout the flow, however, the Reynolds stress tensor is anisotropic and inhomogeneous: shear stress is non-zero away from the axis of symmetry, and streamwise normal stress exceeds transverse normal stress (Hussein et al., 1994). Turbulent transport of momentum causes the jet to entrain fluid and spread with downstream distance. A key observation is that upon non-dimensionalization, cross-jet velocity profiles collapse to a single self-similar profile (Wygnanski and Fiedler, 1969).

1.4 Objectives

Existing methods for Doppler velocity estimation have considered noise suppression and velocity ambiguity separately. However, the presence of measurement noise complicates ambiguity resolution, and vice versa, velocity ambiguity presents a challenge for noise suppression methods. The primary objective of this thesis is to apply MAP estimation to multi-frequency coherent Doppler sonar for the purpose of resolving velocity ambiguity and suppressing measurement noise *simultaneously*, rather than separately. It will then be possible to effectively use coherent Doppler sonar under challenging conditions where both backscatter decorrelation and velocity ambiguity are present, such as in a highly turbulent boundary layer. In Section 1.3.2, it was stated that measurements with additional receivers and multiple acoustic carrier

frequencies can be combined to suppress noise. The resulting MAP velocity estimator will therefore optimally combine redundant measurements to minimize velocity uncertainty.

The MAP velocity estimator will share the following similarities with a Kalman smoother: (i) the estimator processes a time series sequentially using a recursive formulation, (ii) a model is used to provide prior statistical knowledge, (iii) the estimator produces its own performance measure, and (iv) estimator lag is eliminated via forward and backward filtering. However, unlike the Kalman smoother, the MAP velocity estimator will make use of non-Gaussian PDFs and it will be inherently nonlinear. The motivation for using MAP estimation is that velocity ambiguity causes the velocity likelihood function to be multi-modal; thus a Gaussian representation is inappropriate. Also, secondary peaks in the likelihood function would bias a MMSE estimator, whereas MAP estimation correctly selects the most likely peak of the posterior PDF.

This thesis will develop an estimation framework that accommodates commonly used coherent Doppler sonar geometries such as one-dimensional single beam systems, ADCPs with divergent beams, three-dimensional velocity point sensors, and profiling sonars. The aim is to develop an estimator that depends solely on physical parameters of the sonar and is free from empirically determined instrument-specific and application-specific thresholds and constants. While the focus of this thesis is on multi-frequency coherent Doppler sonar, the results will be equally applicable to staggered PRF systems in light of the discussion in Section 1.3.3.

The secondary objective of this thesis is to evaluate MAP velocity estimation using numerical simulations and laboratory experiments under realistic and challenging op-

erating conditions. In particular, laboratory evaluation will include highly turbulent flows with both backscatter decorrelation and velocity ambiguity, i.e. conditions in which coherent Doppler sonar does not normally perform well.

The long-term goal of this work is to develop improved signal processing for oceanographic and hydraulic instrumentation that will contribute to new insights into the dynamics of near-bed turbulence and sediment transport.

1.5 Overview

The results of this thesis are presented in the form of four research papers. Some relevant theory associated with MAP estimation and the Doppler shift for multistatic (i.e. multiple receiver) sonar geometries is included in Chapter 2 prior to presentation of the research results. Although the information in Chapter 2 is not new, it has been included as background material for Chapters 5 and 6. The research contributions of this thesis appear in Chapters 3 to 6.

In order to optimally combine measurements, a data quality metric is needed to appropriately weight each measurement. For coherent Doppler sonar, data quality is evaluated using the magnitude of an autocorrelation coefficient. In Chapter 3, a new formula is derived for the asymptotic form of the magnitude of an autocorrelation coefficient for coherent Doppler sonar. The autocorrelation magnitude is shown to be a biased estimator for finite pulse-pair averages and in the limit of infinite ensemble length. However, the distribution of observed autocorrelation coefficients is well-predicted by a Gaussian random process once the autocorrelation bias has been removed. This work has been published in the *Journal of Atmospheric and Oceanic*

Technology (Dillon et al., 2011a).

One of the inputs to the MAP velocity estimator is a family of probability distributions that describe the likelihood of a particular value of velocity given observations of autocorrelation phase and magnitude. In Chapter 4, the distribution of velocity measurements from coherent Doppler sonar is analyzed using a combination of theory and numerical simulation. It is shown that the velocity distribution exhibits non-normal behaviour for ensemble lengths of less than ten pulse-pairs. Simulation results indicate the range of autocorrelation coefficients for which perturbation analysis may be used to predict velocity standard deviation. This work has been submitted to the *IEEE Journal of Oceanic Engineering* (Dillon et al., 2011c).

In Chapter 5, the MAP velocity estimator is described and evaluated. A method is presented for automatically determining the estimator smoothing parameter from examination of the spectrum of a representative segment of the measurement time series. Measurement noise suppression is evaluated using results from a laboratory turbulent jet in which velocity was measured simultaneously with multi-frequency coherent Doppler sonar and particle image velocimetry. This work has been published in the *Proceedings of the IEEE/OES 10th Current, Waves, and Turbulence Measurement Workshop* (Dillon et al., 2011b).

In Chapter 6, results are presented for a towing tank experiment that used a rectangular grid to generate turbulence upstream of the sonar. It is shown that the MAP velocity estimator simultaneously resolves velocity ambiguity and suppresses measurement noise. The one-dimensional velocity estimator from Chapter 5 is generalized to higher dimensions to show how measurements from multiple transducers may be combined probabilistically. This work has been submitted to the *Journal of*

Atmospheric and Oceanic Technology (Dillon et al., 2011d). Finally, conclusions of this thesis appear in Chapter 7, including directions for future work.

1.6 Instrumentation

Each research paper presents numerical simulations or experimental results for a multi-frequency coherent Doppler profiler known as the MFDop (Hay et al., 2008). The geometry of this multistatic sonar is shown schematically in Figures 2.2, 3.4, 5.2, and 6.4. The sonar normally operates in a downward looking configuration to measure horizontal and vertical velocity components as close as possible to a bottom boundary such as the seabed. Velocity components are measured along a vertical profile extending from about 30 to 50 cm below the transmitter. To resolve the vertical gradients observed in bottom boundary layer flows, the sonar vertical resolution is on the order of 3 to 6 mm whereas the horizontal resolution is approximately 2 cm. The design trade-offs and the rationale for the chosen sample volume geometry are discussed in Hay et al. (2008).

Each MFDop acoustic transducer is a flat circular disk with a diameter of approximately 2 cm. Such disk transducers are comparatively simple to manufacture but have characteristic sidelobes that can introduce deceptive (sidelobe) signals from strong scattering surfaces. In the turbulent jet and grid turbulence experiments, the sonar was oriented to avoid receiving spurious signals from transducer sidelobes or from multipath propagation, for example by tilting the sonar relative to a solid boundary to avoid receiving reflected signals.

Transducer and receiver bandwidth are specified in terms of the frequency interval

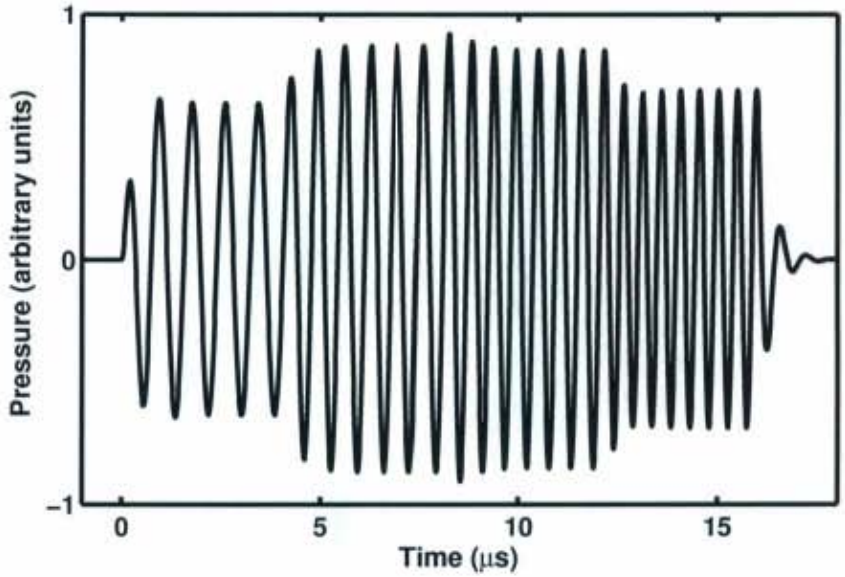

Figure 1.1: Example multi-frequency transmit pulse for carrier frequencies of 1.2, 1.5, 1.8, and 2.1 MHz. Each component is 4 μs in duration. The effects of the transducer bandwidth (1 MHz) and centre frequency (1.7 MHz) have been simulated by applying a first order bandpass filter to a constant amplitude waveform.

between half power points. Properties of the transducers were common throughout all simulations and experiments, namely a bandwidth of 1 MHz and a nominal centre frequency of 1.7 MHz. However, the receiver demodulation bandwidth was adjusted to match the frequency content of the transmitted pulses. A four-tone transmit signal such as the one shown in Figure 1.1 was used throughout the thesis. The pulse length and carrier frequencies for each simulation or experiment are listed in the relevant sections (e.g. Tables 3.1, 4.1, 5.1, and 6.1).

1.7 Co-authorship statement

Authorship for all four research papers presented in Chapters 3 to 6 is listed in the following order: Mr. Jeremy Dillon (thesis author), Dr. Len Zedel (thesis supervisor), and Dr. Alex E. Hay (collaborator). Dr. Zedel is an Associate Professor with the Department of Physics and Physical Oceanography at Memorial University. Dr. Hay is a Professor with the Department of Oceanography at Dalhousie University.

Mr. Dillon was responsible for the conception and development of the ideas contained in each research paper. The towing tank and turbulent jet experiments were performed jointly by all three authors and Mr. Richard Cheel, a research assistant with the Department of Oceanography at Dalhousie University. Numerical simulation and data analysis were performed by Mr. Dillon. Also, Mr. Dillon performed all duties associated with the preparation of each manuscript. Dr. Zedel and Dr. Hay critically reviewed each manuscript and suggested minor revisions.

Chapter 2

Theory

2.1 Bayesian estimation

The basic idea of Bayesian estimation is that prior knowledge can be used to improve estimator performance. Prior knowledge and information obtained from measurements are combined to form the posterior PDF $p(\theta \mid \mathbf{x})$. The posterior PDF expresses the likelihood of the unknown parameter θ taking a particular value given that measurements $\mathbf{x}$ have been observed. The concepts of Bayes risk and cost functions for optimal estimation are introduced in Section 2.1.1. It is shown that an estimator may be formed by minimizing Bayes risk, and that the form of the estimator depends on the cost function. In Section 2.1.2, the "hit-or-miss" cost function is shown to correspond with MAP estimation which maximizes the posterior PDF. The following discussion of Bayesian estimation is based on Kay (1993, chap. 11).

2.1.1 Bayes risk

Let $\hat{\theta}$ represent an estimate of the unknown parameter θ. Estimator error is the difference $\epsilon = \theta - \hat{\theta}$. In order to construct an optimal estimator, it is necessary to specify a non-negative cost function $\mathcal{C}(\epsilon)$. For example, the choice $\mathcal{C}(\epsilon) = \epsilon^2$ is common; however, other symmetric functions such as $\mathcal{C}(\epsilon) = |\epsilon|$ are also useful. The cost function is a deterministic function of the random variable ϵ. Therefore, $\mathcal{C}(\epsilon)$ takes on a different value for each realization of the underlying random process. Estimator performance is quantified by Bayes risk R which expresses the *average* cost

$$\mathsf{R} = E(\mathcal{C}(\epsilon)). \tag{2.1}$$

Bayes risk is therefore a deterministic quantity which can be minimized by appropriate choice of the estimate $\hat{\theta}$.

Expectation in (2.1) is taken with respect to the joint probability distribution $p(\mathbf{x}, \theta)$. Bayes' theorem relates the joint PDF to the conditional probability distribution $p(\theta \,|\, \mathbf{x})$ as follows:

$$p(\mathbf{x}, \theta) = p(\theta \,|\, \mathbf{x})\, p(\mathbf{x}). \tag{2.2}$$

Equation (2.1) becomes

$$\begin{aligned} \mathsf{R} &= \iint \mathcal{C}(\epsilon)\, p(\mathbf{x}, \theta)\, d\theta\, d\mathbf{x} \\ &= \int \left[\int \mathcal{C}(\epsilon)\, p(\theta \,|\, \mathbf{x})\, d\theta \right] p(\mathbf{x})\, d\mathbf{x}. \end{aligned} \tag{2.3}$$

Since $p(\mathbf{x}) \geq 0$ for all $\mathbf{x}$, Bayes risk will be minimized when the inner integral of

(2.3) is minimized for each $\mathbf{x}$. The optimal estimate is therefore found by solving the following equation for $\hat{\theta}$:

$$\frac{\partial}{\partial\hat{\theta}}\int_{-\infty}^{\infty} C(\epsilon)\, p(\theta\,|\,\mathbf{x})\, d\theta = 0. \tag{2.4}$$

For example, substituting a quadratic cost function $C(\epsilon) = \epsilon^2$ in (2.4) yields

$$\begin{aligned} 0 = \frac{\partial}{\partial\hat{\theta}}\int_{-\infty}^{\infty} (\theta-\hat{\theta})^2\, p(\theta\,|\,\mathbf{x})\, d\theta &= -2\int_{-\infty}^{\infty} (\theta-\hat{\theta})\, p(\theta\,|\,\mathbf{x})\, d\theta \\ &= -2\int_{-\infty}^{\infty} \theta\, p(\theta\,|\,\mathbf{x})\, d\theta + 2\hat{\theta}\int_{-\infty}^{\infty} p(\theta\,|\,\mathbf{x})\, d\theta. \end{aligned} \tag{2.5}$$

Observing that $\int_{-\infty}^{\infty} p(\theta\,|\,\mathbf{x})\, d\theta = 1$, (2.5) results in the Bayesian minimum mean square error (MMSE) estimator

$$\hat{\theta} = \int_{-\infty}^{\infty} \theta\, p(\theta\,|\,\mathbf{x})\, d\theta \tag{2.6}$$

which is seen to be the *mean* of the posterior PDF $p(\theta\,|\,\mathbf{x})$.

For the cost function $C(\epsilon) = |\epsilon|$, the inner integral of (2.3) is

$$\int_{-\infty}^{\infty} |\theta-\hat{\theta}|\, p(\theta\,|\,\mathbf{x})\, d\theta = \int_{-\infty}^{\hat{\theta}} (\hat{\theta}-\theta)\, p(\theta\,|\,\mathbf{x})\, d\theta + \int_{\hat{\theta}}^{\infty} (\theta-\hat{\theta})\, p(\theta\,|\,\mathbf{x})\, d\theta. \tag{2.7}$$

Using the Leibniz integral rule, the derivative of (2.7) is

$$\frac{\partial}{\partial\hat{\theta}}\int_{-\infty}^{\infty} |\theta-\hat{\theta}|\, p(\theta\,|\,\mathbf{x})\, d\theta = \int_{-\infty}^{\hat{\theta}} p(\theta\,|\,\mathbf{x})\, d\theta - \int_{\hat{\theta}}^{\infty} p(\theta\,|\,\mathbf{x})\, d\theta. \tag{2.8}$$

Setting the right hand side of (2.8) equal to zero, the Bayesian estimator for $C(\epsilon) = |\epsilon|$

is the *median* of the posterior PDF, i.e. the value $\hat{\theta}$ that satisfies

$$\int_{-\infty}^{\hat{\theta}} p(\theta \,|\, \mathbf{x})\, d\theta = \int_{\hat{\theta}}^{\infty} p(\theta \,|\, \mathbf{x})\, d\theta. \tag{2.9}$$

In general, the posterior mean and median do not coincide. The form of the optimal estimator therefore depends on the cost function used to calculate Bayes risk.

2.1.2 Maximum a posteriori estimation

Another candidate cost function is the so-called "hit-or-miss" function

$$\mathcal{C}(\epsilon) = \begin{cases} 0 & \text{if } |\epsilon| < \delta \\ 1 & \text{otherwise} \end{cases} \tag{2.10}$$

where δ is an error threshold. The corresponding inner integral of (2.3) is

$$\begin{aligned} \int_{-\infty}^{\infty} \mathcal{C}(\theta - \hat{\theta})\, p(\theta \,|\, \mathbf{x})\, d\theta &= \int_{-\infty}^{\hat{\theta}-\delta} p(\theta \,|\, \mathbf{x})\, d\theta + \int_{\hat{\theta}+\delta}^{\infty} p(\theta \,|\, \mathbf{x})\, d\theta \\ &= 1 - \int_{\hat{\theta}-\delta}^{\hat{\theta}+\delta} p(\theta \,|\, \mathbf{x})\, d\theta \end{aligned} \tag{2.11}$$

where the identity $\int_{-\infty}^{\infty} p(\theta \,|\, \mathbf{x})\, d\theta = 1$ has been used. Bayes risk is therefore minimized by maximizing

$$\int_{\hat{\theta}-\delta}^{\hat{\theta}+\delta} p(\theta \,|\, \mathbf{x})\, d\theta. \tag{2.12}$$

In the limit $\delta \to 0$, the optimal estimate $\hat{\theta}$ is the posterior *mode*, i.e. the location of the maximum of the posterior PDF $p(\theta \,|\, \mathbf{x})$. This estimator, known as the Maximum A Posteriori (MAP) estimator, minimizes the Bayes risk for the "hit-or-miss" cost

function in the limit $\delta \to 0$. The following notation will be used to denote the MAP estimate:

$$\hat{\theta} = \arg \max_{\theta} p(\theta \,|\, \mathbf{x}). \tag{2.13}$$

From Bayes' theorem, the posterior PDF $p(\theta \,|\, \mathbf{x})$ can be expressed as

$$p(\theta \,|\, \mathbf{x}) = \frac{p(\mathbf{x} \,|\, \theta)\, p(\theta)}{p(\mathbf{x})}. \tag{2.14}$$

Since the denominator does not depend on θ, an equivalent formulation of the MAP estimator is

$$\hat{\theta} = \arg \max_{\theta} p(\mathbf{x} \,|\, \theta)\, p(\theta). \tag{2.15}$$

The term $p(\mathbf{x} \,|\, \theta)$ expresses the probability of observing measurements $\mathbf{x}$ when the unknown parameter takes the value θ. The term $p(\theta)$ describes any prior knowledge that exists before measurements $\mathbf{x}$ have been observed.

The above discussion has shown that there are at least three different Bayesian estimators to choose from (posterior mean, median, and mode), and each one is optimal with respect to a particular cost function. For Doppler velocity estimation, the unknown parameter θ is either the radial velocity component v (for monostatic sonar) or the velocity vector $\mathbf{v}$ (for multistatic sonar). Measurements $\mathbf{x}$ correspond to the vector $\boldsymbol{\mu}$ of multi-frequency and multi-transducer autocorrelation phase and magnitude. From (2.15), the MAP velocity estimator takes the form

$$\hat{\mathbf{v}} = \arg \max_{\mathbf{v}} p(\boldsymbol{\mu} \,|\, \mathbf{v})\, p(\mathbf{v}). \tag{2.16}$$

2.2 Multistatic geometry

The relationship between scatterer velocity and Doppler frequency shift is developed in Section 2.2.1 for the bistatic case where the transmitter and receiver are not collocated. The derivation generalizes the monostatic velocity-frequency relationship that was presented in Section 1.3.1. It is shown that each transmitter-receiver pair measures a velocity component in the direction of the bistatic baseline along the bisector of the angle subtended by the transmitter, scatterer, and receiver. A transformation from Cartesian to transducer coordinates is derived in Section 2.2.2. An inverse coordinate transformation based on least squares estimation is developed in Section 2.2.3. The inverse transformation is used in Chapter 6 to calculate a velocity vector from measurements obtained using conventional pulse-pair processing.

2.2.1 Bistatic Doppler shift

The Doppler frequency shift due to scatterer motion depends on relative positions of the scatterer, transmitter, and receiver. A bistatic geometry is depicted in Figure 2.1, where scatterer, transmitter, and receiver positions are indicated by S, T, and R, respectively. In the following derivation, R and T are fixed whereas the scatterer is moving with velocity vector $\mathbf{v}$. Unit vectors directed from the scatterer to the transmitter and receiver are denoted by $\mathbf{r}_T$ and $\mathbf{r}_R$. The transmitter-receiver pair measures a velocity component in the direction of the bistatic baseline, i.e. toward the line segment RT and along the bisector of the angle $\angle RST$. Let $\mathbf{r}_B$ denote a unit vector directed toward the baseline in the direction $\mathbf{r}_T + \mathbf{r}_R$ as shown in Figure 2.1.

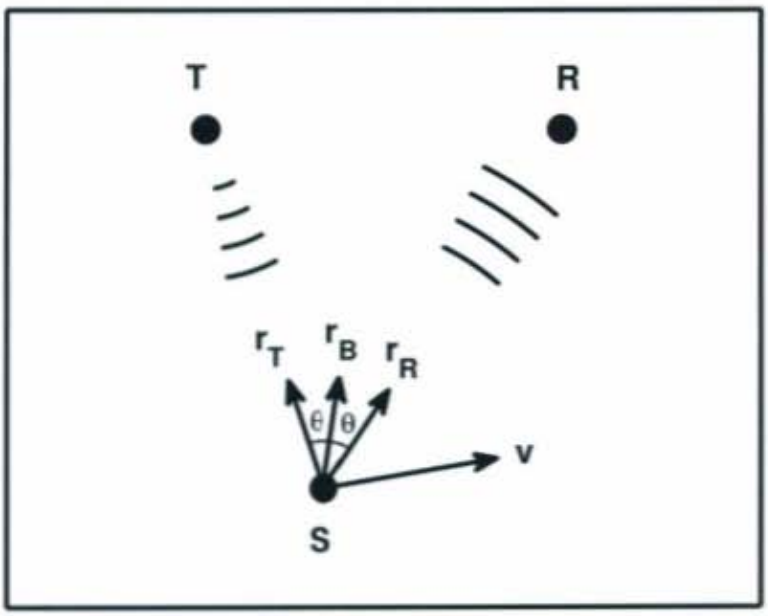

Figure 2.1: Schematic diagram of a scatterer S, transmitter T, and receiver R. The scatterer is moving with velocity vector $\mathbf{v}$. Unit vectors $\mathbf{r}_T$, $\mathbf{r}_R$, and $\mathbf{r}_B$ are directed from the scatterer to the transmitter, to the receiver, and toward the bistatic baseline RT, respectively.

The angle subtended by vectors $\mathbf{r}_T$ and $\mathbf{r}_R$ is denoted by 2θ.

A sinusoidal acoustic source of frequency f_0 is assumed to emanate from the transmitter with a corresponding acoustic wavelength given by

$$\lambda_0 = \frac{c}{f_0}. \tag{2.17}$$

The wavelength λ_0 determines the spacing of surfaces of constant phase that propagate toward the scatterer with speed c. The frequency f_S of acoustic waves impinging upon the scatterer is determined by relative velocity between S and T, i.e. by the

speed of motion across a surface of constant phase, given by

$$f_S = \frac{c + \mathbf{v} \cdot \mathbf{r}_T}{\lambda_0}. \tag{2.18}$$

Using (2.17), substitution for λ_0 results in

$$f_S = \frac{f_0}{c} \left(c + \mathbf{v} \cdot \mathbf{r}_T \right). \tag{2.19}$$

In the scattering process, reflected acoustic waves are produced with frequency f_S. However, motion of the scatterer S causes a change in wavelength compared to the transmitted wavelength λ_0. Relative to the scatterer, the acoustic medium is moving with velocity $-\mathbf{v}$. Wavelength compression or dilation is determined by the relative speed $c - \mathbf{v} \cdot \mathbf{r}_R$ of wave propagation in the direction $\mathbf{r}_R$. Waves scattered in the direction $\mathbf{r}_R$ have a wavelength given by

$$\lambda_S = \frac{c - \mathbf{v} \cdot \mathbf{r}_R}{f_S}. \tag{2.20}$$

Relative to the stationary receiver, however, scattered acoustic waves propagate with speed c. Combining (2.19) and (2.20), the observed frequency f_R at the receiver is given by

$$f_R = \frac{c}{\lambda_S} = f_0 \left(\frac{c + \mathbf{v} \cdot \mathbf{r}_T}{c - \mathbf{v} \cdot \mathbf{r}_R} \right). \tag{2.21}$$

For the monostatic case with collocated transmitter and receiver, (2.21) simplifies to

$$f_R = f_0 \left(\frac{c + v}{c - v} \right) \tag{2.22}$$

which was stated as (1.1) of Section 1.3.1 in terms of the radial velocity component v toward the transducer.

As discussed in Section 1.3.1, $|v| \ll c$ for oceanographic applications. Therefore, (2.21) may be replaced with the first order Taylor series approximation

$$f_R = f_0 \left(1 + \frac{\mathbf{v} \cdot \mathbf{r}_T + \mathbf{v} \cdot \mathbf{r}_R}{c} \right). \tag{2.23}$$

The corresponding Doppler frequency shift $f_D = f_R - f_0$ is

$$f_D = f_0 \left(\frac{\mathbf{v} \cdot \mathbf{r}_T + \mathbf{v} \cdot \mathbf{r}_R}{c} \right). \tag{2.24}$$

In the plane defined by points R, S, and T, the vector $\mathbf{r}_T + \mathbf{r}_R$ lies along the bisector of the angle $\angle RST$. The following relationship holds:

$$\mathbf{r}_T + \mathbf{r}_R = 2\,\mathbf{r}_B \cos\theta. \tag{2.25}$$

Equation (2.24) therefore becomes

$$f_D = f_0 \left(\frac{2\,\mathbf{v} \cdot \mathbf{r}_B \cos\theta}{c} \right) \tag{2.26}$$

which is a bistatic version of (1.4). Thus, a bistatic configuration measures the velocity component $v_B = \mathbf{v} \cdot \mathbf{r}_B$ toward the bistatic baseline according to the Doppler velocity-frequency relationship

$$v_B = \frac{c}{2 f_0 \cos\theta} f_D. \tag{2.27}$$

When the covariance method is used to estimate Doppler frequency, autocorrelation phase and the velocity component v_B are related by

$$\phi = 4\pi f_0 \tau \frac{v_B}{c} \cos\theta \tag{2.28}$$

which is a bistatic version of (1.20).

2.2.2 Cartesian coordinate transformation

A bistatic sonar measures a velocity component in a direction determined by the relative locations of the transmitter, scatterer, and receiver. In current measurement applications, divergent monostatic beams are often used to produce a velocity profile assuming spatial homogeneity between beams (Rowe et al., 1986; Lohrmann et al., 1990). To make a point measurement of a 2D or 3D velocity vector, it is necessary employ multiple intersecting beams, for example with independent transmitter-receiver pairs (Fox and Gardiner, 1988) or by recording sound scattered from a single transmitter toward multiple receivers (Kraus et al., 1994; Zedel and Hay, 2002). The following derivation relates the velocity vector to the components measured by the MFDop (Hay et al., 2008). An inverse transformation is developed in Section 2.2.3.

A symmetric two-dimensional multistatic sonar geometry is shown in Figure 2.2. The advantages of a symmetric configuration over an asymmetric configuration have been described in Zedel (2008). Acoustic signals are transmitted from transducer 3 and backscatter is received by all three transducers. Velocity measurement occurs in the region where transducer beam patterns overlap (Zedel and Hay, 2002), as indicated with dashed lines in Figure 2.2.

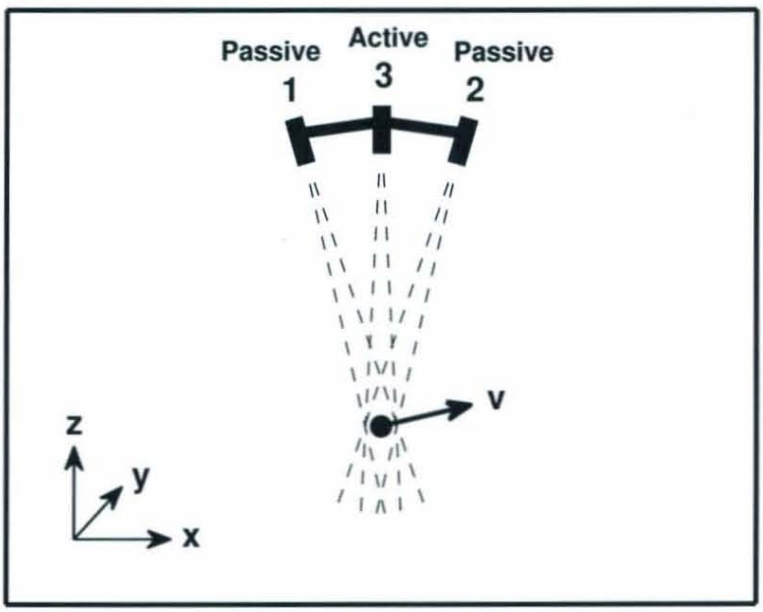

Figure 2.2: Schematic diagram of a symmetric multistatic sonar. Sound is transmitted from transducer 3 and backscatter is received by all transducers. Beam patterns are indicated by dashed lines. The angle between the centre transducer and transducers 1 and 2 is 2γ. Bistatic baselines are tilted by γ from the x-axis.

The arrangement in Figure 2.2 can be extended to three dimensions with additional receivers 4 and 5 out of the plane of the page. For example, transducers 4 and 5 may be located symmetrically in the $-y$ and $+y$ directions by rotating transducers 1 and 2 about the transducer 3 axis.

Each receiver forms a bistatic configuration with the transmitter to measure the velocity component toward the corresponding bistatic baseline. Let γ denote the tilt angle of the transducer 1 and 2 baselines with respect to the x-axis in Figure 2.2 ($\gamma = 7°$ for the MFDop). For the isosceles geometry in Figure 2.2, $\theta = \gamma$ for a scatterer at the beam intersection point. Velocity components measured by each

receiver are denoted by v_j $(j = 1, 2, 3)$ with unit vectors $\mathbf{r}_j$ directed from the beam intersection point toward the corresponding baselines for $j = 1, 2$ and toward the centre transducer for $j = 3$. Unit vectors may be specified in vector form $\mathbf{r} = [r_x \; r_z]^T$ and assembled into a matrix $\mathbf{R}$,

$$\mathbf{R} = \begin{bmatrix} \mathbf{r}_1^T \\ \mathbf{r}_2^T \\ \mathbf{r}_3^T \end{bmatrix} = \begin{bmatrix} -\sin\gamma & \cos\gamma \\ \sin\gamma & \cos\gamma \\ 0 & 1 \end{bmatrix}. \tag{2.29}$$

If the velocity vector is specified in Cartesian coordinates as $\mathbf{v} = [v_x \; v_z]^T$, velocity components $v_j = \mathbf{v} \cdot \mathbf{r}_j$ are given by

$$\begin{aligned} v_1 &= -v_x \sin\gamma + v_z \cos\gamma \\ v_2 &= v_x \sin\gamma + v_z \cos\gamma \\ v_3 &= v_z. \end{aligned} \tag{2.30}$$

2.2.3 Pseudo-inverse coordinate transformation

Equation (2.30) can be written in the matrix form

$$\mathbf{v}_j = \mathbf{R}\mathbf{v} \tag{2.31}$$

where $\mathbf{v}_j$ is the vector of velocity components. If the velocity vector is measured along three linearly independent vectors, then $\mathbf{R}$ is a 3×3 matrix which may be inverted to

obtain $\mathbf{v}$ from $\mathbf{v}_j$,

$$\mathbf{v} = \mathbf{R}^{-1}\mathbf{v}_j. \tag{2.32}$$

When velocity is measured redundantly (i.e. when the number of receivers exceeds the number of velocity components), a pseudo-inverse can be used to determine Cartesian velocity components from transducer measurements. If columns of $\mathbf{R}$ are linearly independent, then the inverse $(\mathbf{R}^T\mathbf{R})^{-1}$ exists and (2.31) may be pseudo-inverted in a least squares sense (Luenberger, 1969, chap. 4),

$$\mathbf{v} = (\mathbf{R}^T\mathbf{R})^{-1}\mathbf{R}^T\mathbf{v}_j. \tag{2.33}$$

When transducers 1, 2, and 3 are used to measure velocity components v_x and v_z, (2.31) takes the form

$$\begin{bmatrix} v_1 \\ v_2 \\ v_3 \end{bmatrix} = \begin{bmatrix} -\sin\gamma & \cos\gamma \\ \sin\gamma & \cos\gamma \\ 0 & 1 \end{bmatrix} \begin{bmatrix} v_x \\ v_z \end{bmatrix} \tag{2.34}$$

which may be pseudo-inverted as in (2.33) to obtain

$$\begin{aligned} v_x &= \frac{v_2 - v_1}{2\sin\gamma} \\ v_z &= \frac{v_3 + (v_1 + v_2)\cos\gamma}{1 + 2\cos^2\gamma}. \end{aligned} \tag{2.35}$$

If each transducer measurement has variance σ_v^2, the corresponding horizontal and

vertical velocity variances are

$$\sigma_x^2 = \frac{\sigma_v^2}{2\sin^2\gamma},$$
$$\sigma_z^2 = \frac{\sigma_v^2}{1+2\cos^2\gamma}. \tag{2.36}$$

Equation (2.36) shows that the ratio of horizontal and vertical measurement error (standard deviation) is given by

$$\frac{\sigma_x}{\sigma_z} = \sqrt{\frac{1+2\cos^2\gamma}{2\sin^2\gamma}}. \tag{2.37}$$

Equation (2.37) is plotted in Figure 2.3, showing that vertical velocity is measured more accurately than horizontal velocity when using a symmetric multistatic geometry. For example, when γ is 7°, the ratio σ_x/σ_z is approximately equal to 10.

While a small angle γ maximizes the beam pattern overlap in Figure 5.2, it becomes difficult to estimate horizontal velocity when the unit vectors $\mathbf{r}_1$ and $\mathbf{r}_2$ are nearly parallel (the so-called "baseline instability" problem). An analysis of the trade-offs, sensitivity, and accuracy for the design of a bistatic sonar may be found in Zedel and Hay (2002).

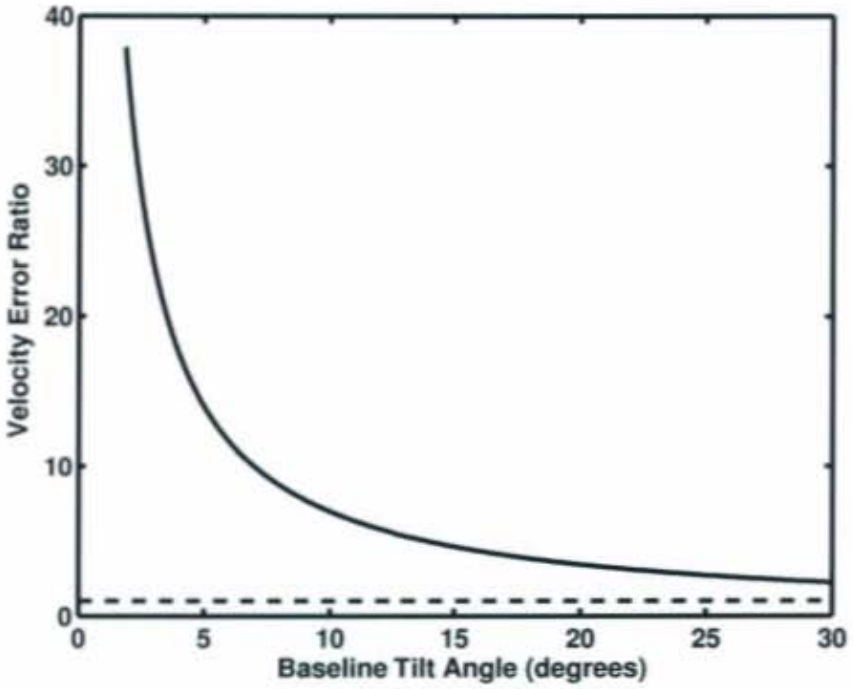

Figure 2.3: Ratio of horizontal to vertical measurement error σ_x/σ_z as a function of baseline tilt angle γ. The dashed line represents a ratio of one.

Chapter 3 Preamble

The magnitude of an autocorrelation coefficient is used as a measure of data quality for coherent Doppler sonar. In this chapter, the autocorrelation magnitude is shown to be a biased estimator. However, once the bias is corrected, the distribution of observed autocorrelation measurements is well-predicted by a Gaussian random process. The results of this chapter are used in Chapters 5 and 6 to determine the probabilty density function of velocity measurements when autocorrelation magnitude is estimated from a finite number of pulse-pairs.

This chapter presents a paper titled "Asymptotic Properties of an Autocorrelation Coefficient for Coherent Doppler Sonar." It has been published in the *Journal of Atmospheric and Oceanic Technology* (Dillon et al., 2011a).

Chapter 3

Autocorrelation Estimation

3.1 Abstract

A new formula is derived for the asymptotic form of the magnitude of an autocorrelation coefficient for coherent Doppler sonar. The autocorrelation magnitude is shown to be a biased estimator in the limit of infinite ensemble length. Numerical simulation of a Gaussian random process is used to verify the asymptotic formula and to show that a bias persists for finite pulse-pair averages. Validity of the asymptotic formula is also confirmed using a high fidelity coherent Doppler sonar simulation, and from sonar measurements in a towing tank. It is shown that the distribution of observed autocorrelation coefficients is well-predicted by a Gaussian random process once the autocorrelation bias has been removed.

3.2 Introduction

Backscatter autocorrelation is the fundamental measurement in pulse-to-pulse coherent Doppler sonar (Garbini et al., 1982; Lhermitte and Serafin, 1984). While velocity is determined from the phase of the complex autocorrelation coefficient, the coefficient magnitude is often used as a measure of data quality. Corresponding to each velocity measurement, many commercially available instruments provide a measure of autocorrelation, for example, as a coefficient between 0% and 100%. Recommended minimum values for the autocorrelation coefficient assist the user in collecting high quality measurements and in diagnosing instrumentation problems when necessary. In addition to qualitative assessment, autocorrelation can also provide quantitative information on the expected magnitude of measurement errors. For example, pulse-to-pulse autocorrelation has been used to identify and replace spurious Doppler velocimeter measurements in the surf zone (Elgar et al., 2005). Also, the relationship between velocity measurement error and autocorrelation has been determined through laboratory testing of a coherent Doppler sonar (Zedel et al., 1996).

For a sequence $\{z_n\}$ of complex-valued backscatter samples, the autocorrelation at a lag of k pulse-to-pulse intervals is

$$R(k\tau) = E(z_n^* z_{n+k}) \tag{3.1}$$

where E denotes expected value, * denotes complex conjugation, and τ is the time interval between successive acoustic transmissions. The autocorrelation coefficient is

defined as

$$\rho = \left|\frac{R(\tau)}{R(0)}\right| = \frac{1}{\sigma^2}\left|E(z_n^* z_{n+1})\right| \tag{3.2}$$

where σ^2 is the variance of the sequence $\{z_n\}$. By definition, ρ is a number between zero and one that expresses the degree of pulse-to-pulse autocorrelation.

In practice, autocorrelation is estimated from a finite sequence $z_1, \ldots, z_L$ corresponding to an ensemble of $M = L - 1$ pulse-pairs (Zrnić, 1977),

$$\hat{R}(\tau) = \frac{1}{M}\sum_{n=1}^{M} z_n^* z_{n+1}. \tag{3.3}$$

Zedel et al. (1996) define the following autocorrelation coefficient as an estimate of ρ:

$$\hat{\rho} = \frac{\left|\sum_{n=1}^{M} z_n^* z_{n+1}\right|}{\sum_{n=1}^{M} |z_n^* z_{n+1}|}. \tag{3.4}$$

The above expression has the desirable property that $\hat{\rho}$ is a number between zero and one. Also, the numerator resembles (3.2) in the sense that expected value has been replaced with a finite sum.

For applications in sediment transport, current measurement, and medical ultrasound, scatterers consist of a large number of particles. Each backscatter sample z is therefore well-described by a complex Gaussian distribution, i.e. $z = x + iy$ where x and y are independent normally distributed random variables with equal variances. In general, a time series of backscatter samples is a non-stationary random process since Doppler frequency, autocorrelation, and amplitude are functions of time. However, in the analysis of coherent Doppler systems, backscatter samples are frequently modelled as being drawn from a wide-sense stationary (WSS) random process with Gaussian

power spectral density (Garbini et al., 1982; Lhermitte and Serafin, 1984; Zedel et al., 1996)

$$P_{zz} = \frac{\sigma^2}{\sigma_f\sqrt{2\pi}} e^{-\frac{(f-f_D)^2}{2\sigma_f^2}} \tag{3.5}$$

where f_D is the mean Doppler frequency and σ_f denotes the spectral width. In this chapter, the term "Gaussian distribution" refers to the probability distribution of a single backscatter sample. The term "Gaussian random process" refers to a time series where (i) each sample obeys a Gaussian distribution, and (ii) the power spectrum of the time series is a Gaussian function as in (3.5).

Autocorrelation is determined from the inverse Fourier transform of the power spectral density

$$\begin{aligned} R(t) &= \frac{\sigma^2}{\sigma_f\sqrt{2\pi}} \int_{-\infty}^{\infty} e^{-\frac{(f-f_D)^2}{2\sigma_f^2}} e^{i2\pi ft}\, df \\ &= \sigma^2 e^{-2\pi^2\sigma_f^2 t^2} e^{i2\pi f_D t}. \end{aligned} \tag{3.6}$$

At an autocorrelation lag of one pulse-to-pulse interval, the autocorrelation coefficient ρ is

$$\rho = \left|\frac{R(\tau)}{R(0)}\right| = e^{-2\pi^2\sigma_f^2\tau^2}. \tag{3.7}$$

Therefore, ρ determines the width of the Doppler spectrum, and hence the variance of velocity measurements.

To compare coherent Doppler sonar observations with expected performance based on a Gaussian random process, it is necessary to examine the relationship between the true autocorrelation coefficient ρ and its estimate $\hat{\rho}$. As increasingly more pulse-pairs are averaged, one would expect the accuracy of the autocorrelation estimate to

improve. Nevertheless, it is shown in this chapter that $\hat{\rho}$ is a biased estimator both for finite averages and in the limit of infinite ensemble length. However, the relationship between $\hat{\rho}$ and ρ may be inverted to obtain unbiased estimates of autocorrelation from biased samples of $\hat{\rho}$. The results presented in this chapter allow theoretical predictions of velocity variance, such as those in Zrnić (1977), to be expressed in terms of the observed autocorrelation estimate rather than the true (but typically unknown) autocorrelation ρ. Since the effectiveness of pulse-pair averaging depends on the correlation between successive measurements, a sonar designer may wish to know how much averaging is required to sufficiently attenuate measurement errors for a given observed coefficient $\hat{\rho}$.

This chapter is organized as follows. In Section 3.3, a new formula is presented for the asymptotic estimator $\hat{\rho}_\infty = \lim_{M\to\infty} \hat{\rho}$. In Section 3.4, properties of $\hat{\rho}$ are determined for finite pulse-pair averages via numerical simulation. Sections 3.5 and 3.6 describe the apparatus and methods employed in a towing tank experiment. Experimental results appear in Section 3.7, followed by a discussion in Section 3.8. Our conclusions are summarized in Section 3.9.

3.3 Theory

The autocorrelation coefficient in (3.4) may be written as

$$\hat{\rho} = \frac{\left| \frac{1}{M} \sum_{n=1}^{M} z_n^* z_{n+1} \right|}{\frac{1}{M} \sum_{n=1}^{M} |z_n| \, |z_{n+1}|}. \tag{3.8}$$

As $M \to \infty$, the numerator converges to $|R(\tau)| = \rho\sigma^2$. Assuming that each sample z_n is described by a Gaussian distribution, the denominator converges to the mean μ of the product of two dependent Rayleigh random variables $|z_n|$ and $|z_{n+1}|$. The product $|z_n|\,|z_{n+1}|$ is described by the probability distribution (Simon, 2002, chap. 6)

$$p(r) = \frac{4r}{\sigma^4(1-\rho^2)} K_0\left(\frac{2r}{\sigma^2(1-\rho^2)}\right) I_0\left(\frac{2r\rho}{\sigma^2(1-\rho^2)}\right) \tag{3.9}$$

where $r = |z_n|\,|z_{n+1}|$, K_0 is a modified Bessel function of the second kind, and I_0 is a modified Bessel function of the first kind. The mean μ is determined from

$$\begin{aligned}\mu &= \int_0^\infty r\,p(r)\,dr \\ &= \frac{4}{\sigma^4(1-\rho^2)} \int_0^\infty r^2 K_0\left(\frac{2r}{\sigma^2(1-\rho^2)}\right) I_0\left(\frac{2r\rho}{\sigma^2(1-\rho^2)}\right) dr.\end{aligned} \tag{3.10}$$

In Appendix 3A, the integral is evaluated in terms of the complete elliptic integral of the second kind $\mathbf{E}(k)$,

$$\mu = \frac{\sigma^2(1+\rho)}{2}\,\mathbf{E}\left(\frac{2\sqrt{\rho}}{1+\rho}\right). \tag{3.11}$$

The asymptotic estimate is, therefore,

$$\hat{\rho}_\infty = \frac{\rho\sigma^2}{\mu} = \frac{2\rho}{(1+\rho)\,\mathbf{E}\left(\frac{2\sqrt{\rho}}{1+\rho}\right)}. \tag{3.12}$$

For small values of ρ, the first order Taylor series is

$$\hat{\rho}_\infty \approx \frac{4\rho}{\pi} \quad \text{as } \rho \to 0. \tag{3.13}$$

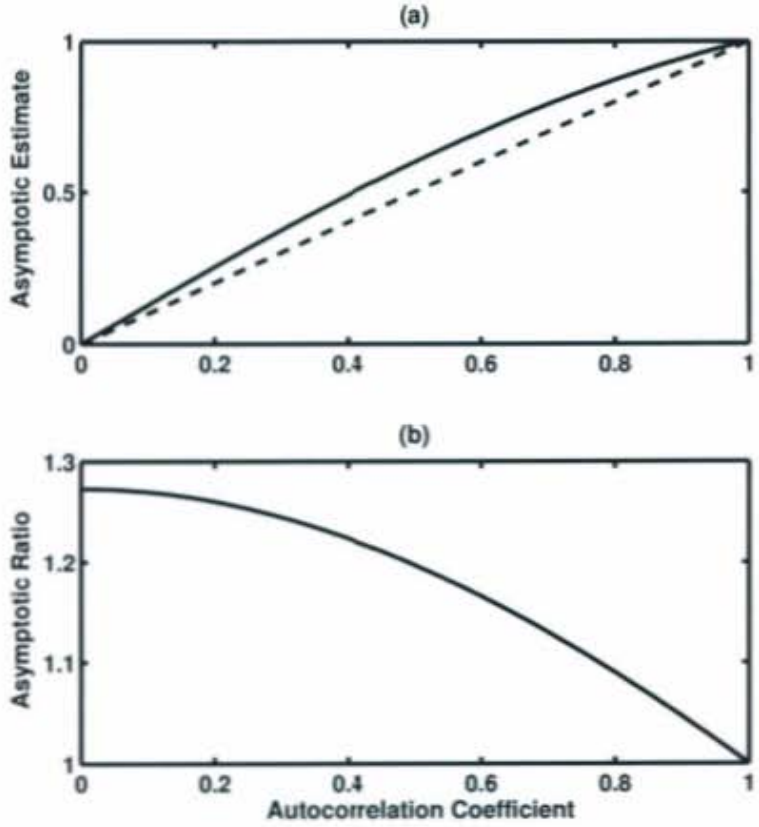

Figure 3.1: Asymptotic autocorrelation estimate $\hat{\rho}_\infty$ from (3.12) as a function of the actual autocorrelation coefficient ρ. In (a), the dashed line represents the ideal relation $\hat{\rho}_\infty = \rho$. In (b), the ratio $\hat{\rho}_\infty/\rho$ is displayed.

For values of ρ near one, the first order Taylor series is given by

$$\hat{\rho}_\infty \approx \frac{\rho+1}{2} \quad \text{as } \rho \to 1. \tag{3.14}$$

The asymptotic estimate and asymptotic ratio $\hat{\rho}_\infty/\rho$ are plotted in Figures 3.1a and 3.1b, respectively. It is evident that the asymptotic estimate is biased for $\rho < 1$.

3.4 Numerical simulation

3.4.1 Gaussian random process

Numerical simulations of a complex Gaussian process were performed using the MATLAB `randn` generator. Let $\zeta_1, \ldots, \zeta_L$ denote an ensemble of L independent identically distributed samples from a complex Gaussian distribution with zero mean and unit variance. For a Gaussian power spectrum, the backscatter autocorrelation sequence R_k is given by (3.6) and (3.7),

$$R_k = \sigma^2 \rho^{k^2} e^{i2\pi f_D \tau k}. \tag{3.15}$$

Let $\mathbf{z}$ denote samples $z_1, \ldots, z_L$ arranged as a vector. The corresponding covariance matrix $\mathbf{C}_z$ is given by (Kay, 1993, chap. 15)

$$\mathbf{C}_z = \begin{bmatrix} R_0 & R_{-1} & \cdots & R_{-(L-1)} \\ R_1 & R_0 & \cdots & R_{-(L-2)} \\ \vdots & \vdots & \ddots & \vdots \\ R_{L-1} & R_{L-2} & \cdots & R_0 \end{bmatrix}. \tag{3.16}$$

By definition, $\mathbf{C}_z$ is Hermitian positive definite and therefore can be written in terms of the Cholesky decomposition (Watkins, 2002, chap. 1)

$$\mathbf{C}_z = \mathbf{U}^* \mathbf{U}. \tag{3.17}$$

Here, $\mathbf{U}$ is an upper triangular matrix with positive diagonal entries and $\mathbf{U}^*$ denotes the conjugate transpose of $\mathbf{U}$. The vector $\boldsymbol{\zeta}$ of independent samples $\zeta_1, \ldots, \zeta_L$ has covariance matrix $E(\boldsymbol{\zeta}\boldsymbol{\zeta}^*) = \mathbf{I}$. Simulated backscatter samples were generated using the transformation

$$\mathbf{z} = \mathbf{U}^*\boldsymbol{\zeta}. \tag{3.18}$$

Therefore, $\mathbf{z}$ has covariance matrix given by

$$E(\mathbf{z}\mathbf{z}^*) = E(\mathbf{U}^*\boldsymbol{\zeta}\boldsymbol{\zeta}^*\mathbf{U}) = \mathbf{U}^*E(\boldsymbol{\zeta}\boldsymbol{\zeta}^*)\mathbf{U} = \mathbf{C}_z \tag{3.19}$$

as desired.

Samples of the autocorrelation estimate $\hat{\rho}$ were generated from 10^7 simulated pings for ensemble lengths of $L = 10$, 20, 40, and 100, and true autocorrelation coefficients ranging from 0.2 to 0.98 in increments of 0.02. For each pair (ρ, L), the mean autocorrelation estimate was calculated as an approximation to the expected value $E(\hat{\rho})$. The ratio $E(\hat{\rho})/\rho$ is plotted in Figure 3.2, where the dashed line is the asymptotic ratio $\hat{\rho}_\infty/\rho$ from (3.12). Although the asymptotic ratio is only strictly valid for $L \to \infty$, simulations for larger values of L indicated that in the interval of $\rho \geq 0.2$, the autocorrelation ratio is within 1% of the asymptotic ratio when L is greater than or equal to 600.

3.4.2 Coherent Doppler sonar model

Numerical simulation of steady flow was also performed with the coherent Doppler sonar model described in Zedel (2008). The model simulates pulse-to-pulse coherent

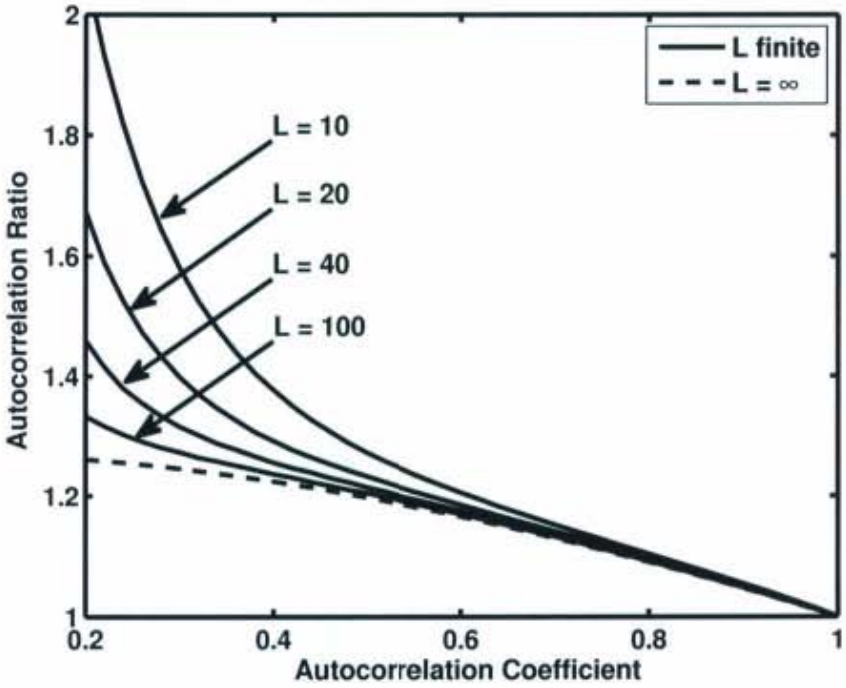

Figure 3.2: Estimated autocorrelation coefficients from simulation of a Gaussian random process. Each curve represents the ratio $E(\hat{\rho})/\rho$ plotted as a function of the true autocorrelation coefficient ρ for a fixed ensemble length L. The dashed line is the asymptotic ratio $\hat{\rho}_\infty/\rho$ from (3.12).

scattering from a cloud of moving particles for arbitrary multistatic sonar geometries. Physical effects such as spherical spreading, acoustic absorption, frequency-dependent beam patterns, transducer frequency response, and receiver noise are included in the model. The model supports simulation of arbitrary pulse shapes, including the use of multiple carrier frequencies.

Simulations were performed for a monostatic sonar measuring horizontal velocities of 0.5, 1.5, 3.0, and 4.5 m s^{-1}. In the model, the sonar was tilted 5° from vertical to reproduce the geometry of the towing tank experiment described in Section 3.5. Parameters for the coherent Doppler sonar simulation are listed in Tables 3.1 and 3.2.

Table 3.1: Coherent Doppler sonar parameters.

Parameter	Value
Transducer centre frequency	1.7 MHz
Transducer bandwidth	1.0 MHz
Receiver bandwidth	250 kHz
Carrier frequency	1.8 MHz
Transmit pulse length	4 μs
Ping interval	1.5 ms
Transducer diameter	2 cm

Table 3.2: Parameters for the coherent Doppler sonar simulation.

Parameter	Value
Particle number density	4720 L^{-1}
Receiver signal-to-noise ratio	10 dB
Simulation time step	12.5 ns
Simulation time	300 s

The model was configured to record the result from each ping in addition to calculating pulse-pair averages. The true autocorrelation coefficient was approximated by averaging over all simulated pings,

$$\rho \approx \frac{1}{\sigma^2}\left|\frac{1}{N-1}\sum_{n=1}^{N-1} z_n^* z_{n+1}\right|, \tag{3.20}$$

where σ^2 is the variance of the backscatter sequence $\{z_n\}$ and $N = 2\times 10^5$ is the total number of simulated pings. The mean autocorrelation estimate $E(\hat{\rho})$ was calculated for ensemble lengths of L = 10, 20, 40, 100, and 1000. Figure 3.3 shows the ratio $E(\hat{\rho})/\rho$ corresponding to each velocity. As L is increased, the ratio converges toward the asymptotic ratio $\hat{\rho}_\infty/\rho$ specified by (3.12).

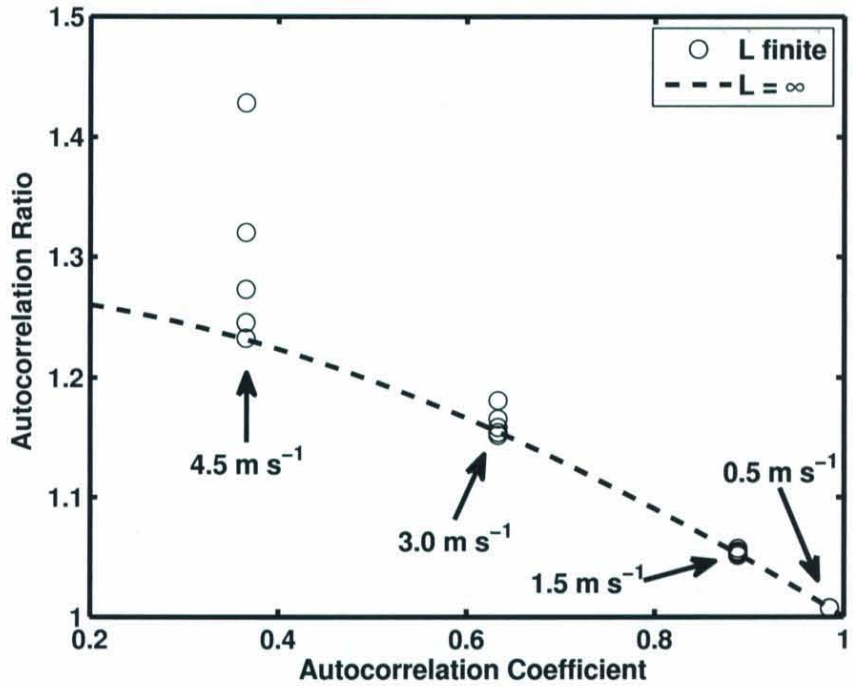

Figure 3.3: Estimated autocorrelation coefficients from the coherent Doppler sonar simulation. Each circle represents the ratio $E(\hat{\rho})/\rho$ plotted as a function of the true autocorrelation coefficient ρ for ensemble lengths of $L = 10$, 20, 40, 100, and 1000. The dashed line is the asymptotic ratio $\hat{\rho}_\infty/\rho$ from (3.12). For increasing values of L, circles converge downward to the dashed line.

3.5 Apparatus

A towing tank experiment was performed using the multi-frequency coherent Doppler sonar described in Hay et al. (2008). Each circular piezo-composite transducer has a diameter of 2 cm, a nominal centre frequency of 1.7 MHz, and a bandwidth of approximately 1 MHz. Carrier frequencies, profiling range, range resolution, pulse length, pulse-to-pulse interval, and ensemble length are configurable in software. The dimensions of each sample volume are determined by the beam pattern, carrier

frequency, and range resolution. Nominally, each sample point has a diameter of 2 cm and a height of 3 mm. The parameters in Table 3.1 also apply for the sonar used in the towing tank experiment.

The experiment was performed in the Marine Craft Model Towing Tank at Dalhousie University. The tank has horizontal dimensions of 30 m $\times$ 1 m and a depth of 1 m. An instrumented carriage is propelled by an electric motor along rails mounted above the tank. Carriage speed is computer-controlled and programmable over a range of 0 to 3.0 m s^{-1}. Constant speed is sustained over a rail length of approximately 25 m. The towing carriage and instrumentation are shown schematically in Figure 3.4. The sonar was rotated to point 5° aft (i.e. counter-clockwise in Figure 3.4) to avoid receiving multiple reflections from the tank bottom. The sonar was located on the tank centre line with the centre transducer 56 cm above the bottom. Water in the tank was seeded with agricultural lime. Prior to each run, approximately 0.5 kg of lime was added to replace scatterers lost to settling. An order of magnitude estimate of sediment concentration was 1 g L^{-1}.

3.6 Experimental procedure

Carriage speed was varied from 0.05 to 3.0 m s^{-1} by programming the desired speed into the towing tank control system. Results are presented in Section 3.7 for velocities of 0.5, 1.5, and 3.0 m s^{-1}. The control system software automatically calculated an acceleration and deceleration profile to maximize the time at constant speed subject to the tank length constraint. Two runs were performed for each speed with a duration of 55 s, or the time elapsed in traversing the entire tank length, whichever was less.

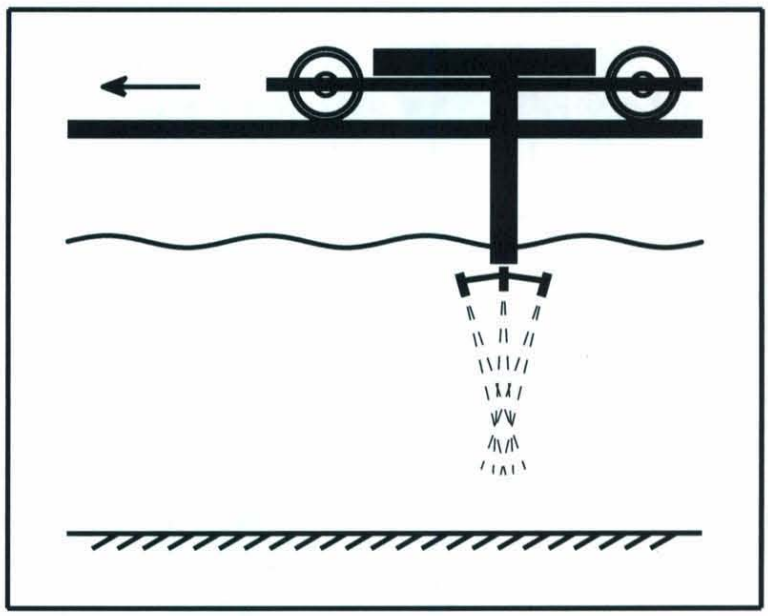

Figure 3.4: Side view schematic of the towing tank showing the multi-frequency coherent Doppler sonar. Instrumentation was attached to a carriage that moved along rails mounted above the water. Transducer beam patterns are indicated with dashed lines.

Carriage speed was recorded by the control system.

Autocorrelation coefficients were recorded by the sonar data acquisition system using a fixed ensemble length of $L = 10$. Since it was not possible to simultaneously record data with multiple ensemble lengths, an indirect approach was taken to assess the validity of simulations in Section 3.4. For each carriage speed, the $L = 10$ curve from Figure 3.2 was used to infer the true autocorrelation coefficient ρ from the mean of the observed estimates $\hat{\rho}$. Histograms of towing tank autocorrelation coefficients were compared with those from a Gaussian random process, as described in Section 3.7.

3.7 Results

In Table 3.3, the mean autocorrelation estimate $E(\hat{\rho})$ was calculated for towing carriage speeds of 0.5, 1.5, and 3.0 m s^{-1} from the 41 cm range bin of the centre transducer receiver channel. Here, $E(\hat{\rho})$ represents the mean magnitude of observed autocorrelation coefficients, which is similar to the measure of data quality reported by commercial instruments. Table 3.3 also lists the corresponding true autocorrelation coefficients estimated from the $L = 10$ curve in Figure 3.2. These values of ρ were used to generate autocorrelation coefficients from a Gaussian random process, as described in Section 3.4.

Table 3.3: Estimated autocorrelation coefficients from towing tank data.

Velocity (m s^{-1})	$E(\hat{\rho})$	ρ **from Figure 3.2**
0.5	0.990	0.977
1.5	0.948	0.899
3.0	0.817	0.713

Distributions of towing tank autocorrelation coefficients are shown in Figure 3.5 for carriage speeds of 0.5, 1.5, and 3.0 m s^{-1}. Values of $\hat{\rho}$ from the centre transducer receiver channel were grouped in 30 equally spaced bins and plotted as histograms. Dotted lines in Figure 3.5 represent distributions of $\hat{\rho}$ from a Gaussian random process with $L = 10$ and ρ as listed in Table 3.3. Dashed lines in Figure 3.5 represent distributions of $\hat{\rho}$ that result from assuming that no bias exists, i.e. that $\rho \approx E(\hat{\rho})$. Histograms were generated from 10^7 simulated pings, with autocorrelation coefficients grouped in 200 equally spaced bins.

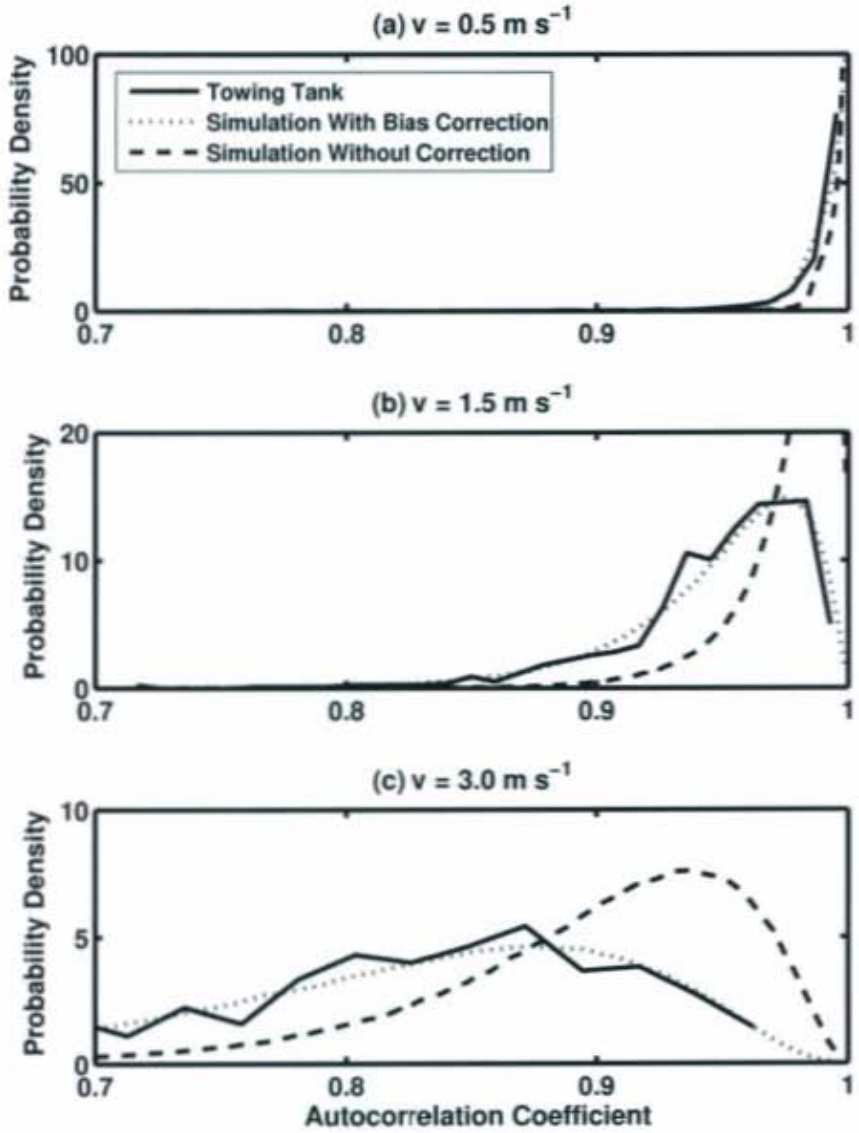

Figure 3.5: Distributions of measured and simulated autocorrelation coefficients. Each solid line is a histogram of $\hat{\rho}$ from the 41 cm range bin of the centre transducer 1.8 MHz receiver channel. Dotted lines represent the corresponding distributions from a Gaussian random process where the autocorrelation bias has been removed using the $L = 10$ curve in Figure 3.2. Dashed lines represent simulated distributions with no bias correction.

3.8 Discussion

The derivation of the asymptotic autocorrelation coefficient assumed a complex Gaussian probability distribution for each backscatter sample. However, it was not necessary to assume a Gaussian power spectrum for the time series since the asymptotic formula depends only on the expected autocorrelation at a lag of one pulse-to-pulse interval. The formula was presented in terms of an elliptic integral. Although $\mathbf{E}(k)$ cannot be expressed in terms of elementary functions, it may be evaluated numerically, for example, with the `ellipke` function in MATLAB.

Numerical simulation of a Gaussian random process showed that the bias of the autocorrelation coefficient increases for short ensemble lengths. For example, the degenerate case of a single pulse-pair results in a coefficient of one regardless of the actual pulse-to-pulse autocorrelation. A longer ensemble length is necessary to obtain meaningful autocorrelation estimates. As shown in Figure 3.2, a bias persists for all of the ensemble lengths, with convergence to the asymptotic formula occurring for L approximately equal to 600. The bias is more significant for small values of the autocorrelation coefficient. For practical applications where reasonably high quality data are obtained (say $\rho \geq 0.7$), there is negligible variation in the ratio $\hat{\rho}/\rho$ as L is varied. However, a bias is still present for $\rho \geq 0.7$, and in this case the bias is well described by the asymptotic formula (3.12).

The coherent Doppler sonar model in Zedel (2008) does not require any Gaussian assumption about the backscatter probability distribution or the time series power spectrum. The model describes the physics of coherent scattering and accounts for the sonar geometry and operating parameters, unlike the simulations of a Gaussian

random process in Section 3.4. Simulations of steady flow confirmed that the autocorrelation coefficient converges to the asymptotic formula as ensemble length is increased. However, similarity between Figures 3.2 and 3.3 shows that simulation of a Gaussian random process is sufficient to predict the bias of the autocorrelation coefficient.

In Table 3.3, the mean observed autocorrelation estimates from the towing tank satisfy $E(\hat{\rho}) > 0.8$, which is within the range of acceptable data quality for commercial instruments. Although the towing tank experiment was performed for a single ensemble length, results in Figure 3.5 validate the relationship between $\hat{\rho}$ and ρ for the $L = 10$ curve in Figure 3.2. When it is assumed that $\rho \approx E(\hat{\rho})$ instead of accounting for the autocorrelation bias, simulated histograms in Figure 3.5 do not match experimental observations. As expected, the discrepancy increased with velocity due to backscatter decorrelation from particle advection through the sonar sample volume. However, when the autocorrelation bias is removed, simulated distributions of the autocorrelation coefficient closely match experimental observations. The towing tank experiment confirms the validity of the Gaussian random process for predicting the bias of the autocorrelation coefficient. One would therefore expect towing tank observations to converge to the asymptotic formula as the ensemble length is increased.

It would be interesting to repeat the towing tank experiment with additional runs for each carriage speed while recording the result from each ping. Autocorrelation coefficients could be calculated for a range of ensemble lengths to demonstrate convergence to the asymptotic formula, as in Section 3.4, for the coherent Doppler sonar simulation. Reproduction of Figure 3.3 with experimental measurements would

require approximately 300 seconds of data for each speed. At 3.0 m s^{-1}, the carriage would need to travel 900 m, requiring 36 runs in the Dalhousie University towing tank. For such an endeavour, a longer tank or a continuously operated flume would be more suitable.

Finally, we remark that the definition of the autocorrelation coefficient is not unique. The coefficient considered in this chapter is an appropriate choice since $0 \leq \hat{\rho} \leq 1$ and the numerator $\sum z_n^* z_{n+1}$ is similar in form to the expected value in the definition of autocorrelation. However, any power or root of $\hat{\rho}$ also provides a measure of pulse-to-pulse autocorrelation while taking values in the interval $[0, 1]$. The method presented in Appendix 3A could be applied to analyze the asymptotic behaviour of other coefficients. If the analysis turns out to be intractable, one may resort to numerical simulation as in Section 3.4.

3.9 Conclusions

A new formula has been presented for the asymptotic form of an autocorrelation coefficient for coherent Doppler sonar. The derivation showed that the autocorrelation coefficient is a biased estimator in the limit of infinite ensemble length. Numerical simulation of a Gaussian random process indicated that the bias persists for finite pulse-pair averages. Furthermore, the bias increases for shorter ensemble lengths. Validity of the Gaussian random process was confirmed with numerical simulation using a high fidelity coherent Doppler sonar model, and from sonar measurements in a towing tank where the towing carriage travelled at constant speed. The experiment showed that the distribution of observed autocorrelation coefficients is well-predicted by a

Gaussian random process once the autocorrelation bias has been removed. Although other autocorrelation coefficients may be defined, the analysis and numerical methods developed in this chapter could be applied to derive their asymptotic behaviour.

3A Asymptotic autocorrelation bias

In Section 3.3, the asymptotic autocorrelation coefficient was shown to be

$$\hat{\rho}_\infty = \frac{\rho\sigma^2}{\mu} \tag{3.21}$$

where the denominator μ is given by

$$\mu = \frac{4}{\sigma^4(1-\rho^2)} \int_0^\infty r^2 \, K_0\left(\frac{2r}{\sigma^2(1-\rho^2)}\right) I_0\left(\frac{2r\rho}{\sigma^2(1-\rho^2)}\right) dr. \tag{3.22}$$

The following identity results from the integral 6.576-5 of Gradshteyn and Ryzhik (2007):

$$\int_0^\infty r^2 \, K_0(ar) \, I_0(br) \, dr = \frac{2\,\Gamma(\frac{3}{2})^2}{a^3\,\Gamma(1)} \, F\left(\frac{3}{2}, \frac{3}{2}; 1; \frac{b^2}{a^2}\right) \tag{3.23}$$

where $\Gamma(z) = \int_0^\infty t^{z-1} e^{-t} \, dt$ is the gamma function and F is the hypergeometric function (Ahlfors, 1966, chap. 8). Equation (3.23) is valid when $a > b$. The gamma function satisfies $\Gamma(1) = 1$ and $\Gamma(3/2) = \sqrt{\pi}/2$, resulting in

$$\int_0^\infty r^2 \, K_0(ar) \, I_0(br) \, dr = \frac{\pi}{2a^3} \, F\left(\frac{3}{2}, \frac{3}{2}; 1; \frac{b^2}{a^2}\right). \tag{3.24}$$

To apply (3.24) to (3.22), let

$$a = \frac{2}{\sigma^2(1-\rho^2)}, \tag{3.25}$$

$$b = \frac{2\rho}{\sigma^2(1-\rho^2)}. \tag{3.26}$$

Therefore, $b/a = \rho$ implies that $a > b$ is satisfied when $\rho < 1$. Equation (3.24) becomes

$$\int_0^\infty r^2 K_0(ar) I_0(br)\, dr = \frac{\pi\sigma^6(1-\rho^2)^3}{16} F\left(\frac{3}{2}, \frac{3}{2}; 1; \rho^2\right). \tag{3.27}$$

Substitution of (3.27) in (3.22) results in

$$\mu = \frac{\pi\sigma^2(1-\rho^2)^2}{4} F\left(\frac{3}{2}, \frac{3}{2}; 1; \rho^2\right). \tag{3.28}$$

The integral 9.112 of Gradshteyn and Ryzhik (2007) may be used to evaluate the hypergeometric function

$$F\left(\frac{3}{2}, \frac{3}{2}; 1; \rho^2\right) = \frac{1}{2\pi} \int_0^{2\pi} \frac{dx}{(1+\rho^2-2\rho\cos x)^{3/2}}. \tag{3.29}$$

The following identity appears as integral 2.575-4 in Gradshteyn and Ryzhik (2007):

$$\int \frac{dx}{(c-d\cos x)^{3/2}} = \frac{2}{(c-d)\sqrt{c+d}}\, \mathcal{E}(\delta, r) \tag{3.30}$$

where

$$\mathcal{E}(\varphi, k) = \int_0^\varphi \sqrt{1-k^2\sin^2 x}\, dx \tag{3.31}$$

is the elliptic integral of the second kind, and

$$\delta = \sin^{-1}\sqrt{\frac{(c+d)(1-\cos x)}{2(c-d\cos x)}}, \tag{3.32}$$

$$r = \sqrt{\frac{2d}{c+d}}. \tag{3.33}$$

Equation (3.30) is valid for $c > d > 0$ and $0 \leq x \leq \pi$. To apply (3.30) to (3.29), let

$$c = 1 + \rho^2, \tag{3.34}$$

$$d = 2\rho. \tag{3.35}$$

Therefore, $c > d > 0$ is satisfied when $0 < \rho < 1$. The parameter r is given by

$$r = \frac{2\sqrt{\rho}}{1+\rho}. \tag{3.36}$$

Symmetry of the integrand in (3.29) implies that

$$F\left(\frac{3}{2}, \frac{3}{2}; 1; \rho^2\right) = \frac{1}{\pi}\int_0^{\pi} \frac{dx}{(1+\rho^2-2\rho\cos x)^{3/2}}. \tag{3.37}$$

Since integration occurs over the interval $0 \leq x \leq \pi$, (3.30) may be used to obtain

$$F\left(\frac{3}{2}, \frac{3}{2}; 1; \rho^2\right) = \frac{2}{\pi(1-\rho)^2(1+\rho)}\,\mathcal{E}\left(\delta, \frac{2\sqrt{\rho}}{1+\rho}\right)\Bigg|_0^{\pi}. \tag{3.38}$$

Noting that $\delta(0) = 0$, $\delta(\pi) = \pi/2$, and $\mathcal{E}(0,k) = 0$, (3.38) reduces to

$$F\left(\frac{3}{2}, \frac{3}{2}; 1; \rho^2\right) = \frac{2}{\pi(1-\rho)^2(1+\rho)}\,\mathbf{E}\left(\frac{2\sqrt{\rho}}{1+\rho}\right) \tag{3.39}$$

where $\mathbf{E}(k) = \mathcal{E}\left(\frac{\pi}{2}, k\right)$ is the complete elliptic integral of the second kind. Combining (3.28) and (3.39) results in

$$\mu = \frac{\sigma^2(1+\rho)}{2}\,\mathbf{E}\left(\frac{2\sqrt{\rho}}{1+\rho}\right). \tag{3.40}$$

Substitution of (3.40) in (3.21) produces the final result,

$$\hat{\rho}_\infty = \frac{2\rho}{(1+\rho)\,\mathbf{E}\left(\frac{2\sqrt{\rho}}{1+\rho}\right)}. \tag{3.41}$$

Bibliography

Ahlfors, L. V. (1966). *Complex Analysis.* McGraw-Hill, second edition.

Elgar, S., Raubenheimer, B., and Guza, R. T. (2005). Quality control of acoustic Doppler velocimeter data in the surfzone. *Measurement Science and Technology*, 16(10):1889–1893.

Garbini, J. L., Forster, F. K., and Jorgensen, J. E. (1982). Measurement of fluid turbulence based on pulsed ultrasound techniques. Part 1. Analysis. *Journal of Fluid Mechanics*, 118:445–470.

Gradshteyn, I. S. and Ryzhik, I. M. (2007). *Tables of Integrals, Series, and Products.* Academic Press, seventh edition.

Hay, A. E., Zedel, L., Craig, R., and Paul, W. (2008). Multi-frequency, pulse-to-pulse coherent Doppler sonar profiler. In *Proceedings of the IEEE/OES 9th Working Conference on Current Measurement Technology*, pages 25–29.

Kay, S. M. (1993). *Fundamentals of Statistical Signal Processing: Estimation Theory*, volume 1. Prentice-Hall PTR.

Lhermitte, R. and Serafin, R. (1984). Pulse-to-pulse coherent Doppler sonar signal processing techniques. *Journal of Atmospheric and Oceanic Technology*, 1(4):293–308.

Simon, M. K. (2002). *Probability Distributions Involving Gaussian Random Variables: A Handbook for Engineers and Scientists.* Springer.

Watkins, D. S. (2002). *Fundamentals of Matrix Computations.* John Wiley & Sons, second edition.

Zedel, L. (2008). Modeling pulse-to-pulse coherent Doppler sonar. *Journal of Atmospheric and Oceanic Technology*, 25(10):1834–1844.

Zedel, L., Hay, A. E., Cabrera, R., and Lohrmann, A. (1996). Performance of a single-beam pulse-to-pulse coherent Doppler profiler. *IEEE Journal of Oceanic Engineering*, 21(3):290–297.

Zrnić, D. S. (1977). Spectral moment estimates from correlated pulse pairs. *IEEE Transactions on Aerospace and Electronic Systems*, AES-13(4):344–354.

Chapter 4 Preamble

In order to optimally combine coherent Doppler sonar measurements, a family of probability distributions is required to describe the likelihood of a particular value of velocity given observations of autocorrelation phase and magnitude. In this chapter, the distribution of velocity measurements is analyzed using a combination of theory and numerical simulation. It is shown that the velocity distribution exhibits non-normal behaviour for ensemble lengths of less than ten pulse-pairs. Probability density functions are expressed in terms of autocorrelation phase error, number of pulse-pairs per ensemble, and the magnitude of the autocorrelation coefficient. The results of this chapter are combined with the autocorrelation bias correction in Chapter 3 to determine velocity likelihood functions in Chapters 5 and 6.

This chapter presents a paper titled "On the Distribution of Velocity Measurements from Pulse-to-Pulse Coherent Doppler Sonar." It has been submitted to the *IEEE Journal of Oceanic Engineering* (Dillon et al., 2011c).

Chapter 4

Velocity Measurement Distribution

4.1 Abstract

The distribution of velocity measurements from pulse-to-pulse coherent Doppler sonar is analyzed for ensemble lengths consisting of less than ten pulse-pairs. A formula is presented for the probability distribution of velocity measurements from a single pulse-pair. The resulting distribution is shown to be non-normal for all values of the pulse-to-pulse autocorrelation coefficient. In particular, single pulse-pair velocity measurements obey a Pearson Type VII distribution in the limit of perfect pulse-to-pulse correlation. The Pearson Type VII distribution has a higher peak and broader tails compared to a normal distribution. Numerical simulation of a Gaussian random process is used to determine second and fourth moments of the multiple pulse-pair measurement distribution. Validity of the Gaussian random process is confirmed using a high fidelity coherent Doppler sonar simulation. Simulation results indicate the range of autocorrelation coefficients for which perturbation analysis may be used

to predict velocity standard deviation. For ensemble lengths less than four pulse-pairs, the ratio of standard deviation to that predicted by perturbation analysis differs from unity by at least 5% for all values of the autocorrelation coefficient. For lengths greater than six pulse-pairs, perturbation analysis is within 5% when the autocorrelation coefficient lies in the interval from 0.62 to 0.96. Calculation of kurtosis shows that multiple pulse-pair velocity measurements obey a non-normal distribution for ensembles containing less than six pulse-pairs. However, for ensemble lengths greater than six pulse-pairs, kurtosis is within 5% of that of a normal distribution for autocorrelation coefficients in the interval from 0.80 to 0.98.

4.2 Introduction

The covariance method is well-established as a suitable velocity estimator for pulse-to-pulse coherent Doppler sonar (Lhermitte and Serafin, 1984; Rowe et al., 1986; Lohrmann et al., 1990). Knowledge of the distribution of velocity measurements made with the covariance method is useful for the design and analysis of coherent Doppler systems. For example, successful resolution of velocity ambiguity with a staggered pulse repetition frequency (PRF) places upper bounds on the allowable magnitude of measurement errors (Lohrmann et al., 1990). Although pulse-pair averaging may be used to reduce errors, the effectiveness of averaging depends on the correlation between successive measurements. A sonar designer may therefore wish to know how much averaging is required to sufficiently reduce measurement errors while achieving the maximum possible sampling rate.

Multiple acoustic carrier frequencies have also been employed to measure velocity

beyond the Nyquist limit of a single frequency system (Nitzpon et al., 1995; Hay et al., 2008). However, as noted in Zedel and Hay (2010), the ambiguity limit cannot be extended arbitrarily when measurements are corrupted with noise. The designer of a multi-frequency system must know how velocity measurements are distributed to establish an acceptable trade-off between ambiguity velocity and the receiver bandwidth necessary to resolve ambiguity.

The covariance method is a time-domain estimator of mean Doppler frequency based on pulse-to-pulse autocorrelation (Miller and Rochwarger, 1972). For a sequence $\{z_n\}$ of complex-valued backscatter samples, the autocorrelation at a lag of k pulse-to-pulse intervals is

$$R(k\tau) = E(z_n^* z_{n+k}) \tag{4.1}$$

where E denotes expected value, * denotes complex conjugation, and τ is the time interval between successive acoustic transmissions. The autocorrelation coefficient is defined as

$$\rho = \left|\frac{R(\tau)}{R(0)}\right| = \frac{1}{\sigma^2}\left|E(z_n^* z_{n+1})\right| \tag{4.2}$$

where σ^2 is the variance of the sequence $\{z_n\}$. Radial velocity is determined from the phase $\phi = \angle R(\tau)$,

$$v = \frac{c}{4\pi f_0 \tau}\phi; \quad \phi \in [-\pi, \pi] \tag{4.3}$$

where c is the speed of acoustic wave propagation and f_0 is the carrier frequency of the transmitted signal. Phase may therefore be interpreted as a non-dimensional representation of velocity.

For applications in sediment transport and current measurement, scatterers con-

sist of a large number of particles. Each backscatter sample z is therefore well-described by a complex Gaussian distribution, i.e. $z = x + iy$ where x and y are independent normally distributed random variables with equal variances. In general, a sequence of backscatter samples is a non-stationary random process since Doppler frequency, autocorrelation, and amplitude are functions of time. However, in the analysis of coherent Doppler systems, backscatter is frequently modelled as a wide-sense stationary (WSS) complex random process with Gaussian power spectral density (Lhermitte and Serafin, 1984; Garbini et al., 1982)

$$P_{zz} = \frac{\sigma^2}{\sigma_f \sqrt{2\pi}} e^{-\frac{(f-f_D)^2}{2\sigma_f^2}} \tag{4.4}$$

where σ_f is the spectral width and f_D denotes the mean Doppler frequency

$$f_D = f_0 \frac{2v}{c}. \tag{4.5}$$

In this chapter, the term "Gaussian random process" refers to a time series where (i) each sample obeys a complex Gaussian distribution, and (ii) the power spectrum of the time series is a Gaussian function as in (4.4).

Autocorrelation is determined from the inverse Fourier transform of the power spectral density

$$\begin{aligned} R(t) &= \frac{\sigma^2}{\sigma_f \sqrt{2\pi}} \int_{-\infty}^{\infty} e^{-\frac{(f-f_D)^2}{2\sigma_f^2}} e^{i2\pi ft}\, df \\ &= \sigma^2 e^{-2\pi^2 \sigma_f^2 t^2} e^{i2\pi f_D t}. \end{aligned} \tag{4.6}$$

At an autocorrelation lag of one pulse-to-pulse interval, the autocorrelation coefficient ρ is

$$\rho = \left| \frac{R(\tau)}{R(0)} \right| = e^{-2\pi^2 \sigma_f^2 \tau^2}. \tag{4.7}$$

Therefore, ρ determines the width of the Doppler spectrum, and hence the variance of velocity measurements.

Analyses of the covariance method have been published in the Doppler radar literature (Zrnić, 1977; Woodman and Hagfors, 1969; Lank et al., 1973). A probability distribution for the phase estimate has been derived for the limiting case of a large number of pulse-pairs (Woodman and Hagfors, 1969, eq. (10)). The limiting distribution is normal when the variance is sufficiently small (Woodman and Hagfors, 1969, eqs. (12), (13)).

In Zrnić (1977), variance of the mean frequency estimator was derived as a function of the pulse-to-pulse autocorrelation coefficient and signal-to-noise ratio (SNR) using perturbation analysis. The equivalent phase standard deviation σ_p is (Zrnić, 1977, eq. (9))

$$\sigma_p^2 = \frac{1}{2\rho^2 M} \left\{ (1-\rho^2) \left[1 + 2 \sum_{k=1}^{M-1} \left(1 - \frac{k}{M} \right) \rho^{2k^2} \right] + \frac{1}{\eta^2} + \frac{2}{\eta} \left(1 - \rho^4 + \frac{\rho^4}{M} \right) \right\} \tag{4.8}$$

where η is the SNR and M is the number of pulse-pairs in the autocorrelation estimate. In the limit of infinite SNR, (4.8) simplifies to

$$\sigma_p^2 = \frac{1-\rho^2}{2\rho^2 M} \left[1 + 2 \sum_{k=1}^{M-1} \left(1 - \frac{k}{M} \right) \rho^{2k^2} \right]. \tag{4.9}$$

The assumptions inherent in perturbation analysis are that the dwell time $M\tau$ is long

compared to the decorrelation time (Zrnić, 1977, eq. (B17a)),

$$2\pi M\sigma_f\tau \gg 1, \tag{4.10}$$

and that perturbations about the mean value are not excessive (Zrnić, 1977, eq. (B17b)),

$$\frac{(1+1/\eta)^2}{\rho^2 M} \ll 1. \tag{4.11}$$

Condition (4.10) is satisfied for sufficiently large spectral widths. However, for a single pulse-pair ($M = 1$), condition (4.11) is never satisfied since $\rho \leq 1$. For multiple pulse-pairs, the inequalities in (4.10) and (4.11) do not indicate how much smaller or larger than unity the corresponding terms must be for the analysis to be valid.

In practice, autocorrelation is estimated from an ensemble of backscatter samples $z_1, \ldots, z_L$ corresponding to $M = L - 1$ pulse pairs (Zrnić, 1977),

$$\hat{R}(\tau) = \frac{1}{M}\sum_{n=1}^{M} z_n^* z_{n+1}. \tag{4.12}$$

Phase is determined from the real and imaginary components of (4.12),

$$\hat{\phi} = \angle \hat{R}(\tau) = \tan^{-1}\frac{\mathcal{I}(\hat{R}(\tau))}{\mathcal{R}(\hat{R}(\tau))}. \tag{4.13}$$

The phase estimate $\hat{\phi}$ is a random variable defined on the interval $[-\pi, \pi]$ radians. We wish to know how $\hat{\phi}$ deviates from the true value ϕ.

In this chapter, theoretical analysis and numerical simulation are employed to precisely determine the conditions for which perturbation analysis correctly predicts

phase standard deviation. In sonar applications, the maximum achievable sampling rate is often limited by range ambiguity and power considerations. Short ensemble lengths are therefore of interest for turbulence measurement, where it is desirable to maximize the sampling rate to resolve the inertial subrange. We focus on ensemble lengths of less than ten pulse-pairs to investigate conditions for which perturbation analysis fails to predict phase standard deviation. It is found that velocity measurements from short ensembles exhibit non-normal probability distributions.

For applications in sediment transport and turbulence measurement, broadening of the Doppler spectrum arises from scatterer advection through the sample volume and velocity shear and turbulence within the sample volume (Newhouse et al., 1976, 1977). Equation (4.8) indicates that phase variance due to receiver noise is negligible when the SNR is on the order of 20 dB (see Zrnić (1977, Fig. 2), and also Kay (1993, Fig. 9.2)). Laboratory testing of a 1.7 MHz coherent Doppler sonar in Zedel et al. (1996) also provides an example where the variance contribution from random phase changes in the receiver was negligible under typical operating conditions. This chapter therefore focuses on the case where velocity measurement error is dominated by the effect of spectral width rather than receiver noise.

The remainder of the chapter is organized as follows. In Section 4.3, a formula is presented for the single pulse-pair phase distribution. Second and fourth moments are calculated to show that the resulting distribution is non-normal for all values of the pulse-to-pulse autocorrelation coefficient. In particular, single pulse-pair measurements obey a Pearson Type VII distribution in the limit of perfect pulse-to-pulse correlation. Derivation of the single pulse-pair distribution is included in Appendix 4A. The limiting form of the distribution is derived in Appendix 4B. In Section 4.4,

standard deviation and kurtosis of the multiple pulse-pair phase distribution are determined via numerical simulation of a Gaussian random process. Validation of the Gaussian random process is performed using a high fidelity coherent Doppler sonar simulation in Section 4.5. Results are discussed in Section 4.6, followed by a summary of our conclusions in Section 4.7.

4.3 Theory

For a single pulse-pair, the autocorrelation estimate from (4.12) simplifies to

$$\hat{R}(\tau) = z_1^* z_2, \tag{4.14}$$

with autocorrelation phase given by

$$\hat{\phi} = \angle z_2 - \angle z_1. \tag{4.15}$$

The phase distribution $p(\hat{\phi})$ is well known in the synthetic aperture radar literature (Just and Bamler, 1994). A derivation is included in Appendix 4A. The resulting distribution is a symmetric function of the phase difference $\psi = \hat{\phi} - \phi$,

$$p(\psi) = \frac{1-\rho^2}{2\pi(1-a^2)}\left[1 + \frac{a}{\sqrt{1-a^2}}\left(\pi - \cos^{-1} a\right)\right] \tag{4.16}$$

where $a = \rho\cos\psi$. Equation (4.16) is plotted in Figure 4.1 for four representative values of ρ.

The behaviour of (4.16) in the limit $\rho \to 0$ is obtained from a first order Taylor

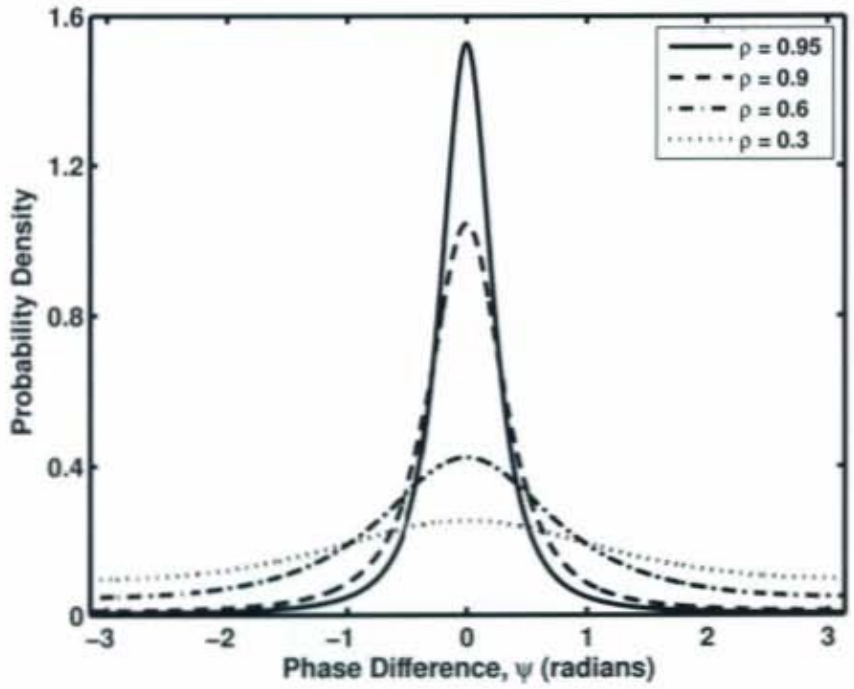

Figure 4.1: Phase distribution of a single pulse-pair. Equation (4.16) is plotted for four values of the autocorrelation coefficient ρ.

series in the variable a,

$$p(\psi) \approx \frac{1}{2\pi} + \frac{\rho \cos\psi}{4}. \tag{4.17}$$

As expected, the phase distribution converges to a uniform distribution on the interval $[-\pi, \pi]$ as $\rho \to 0$.

To examine the limit $\rho \to 1$, let $\varepsilon = \sqrt{1-\rho^2}$ so that $\varepsilon \to 0$ as $\rho \to 1$. The behaviour of (4.16) in the limit $\rho \to 1$ is shown in Appendix 4B to be

$$p(\psi) \approx \frac{1}{2\varepsilon} \frac{1}{(1+(\psi/\varepsilon)^2)^{3/2}}. \tag{4.18}$$

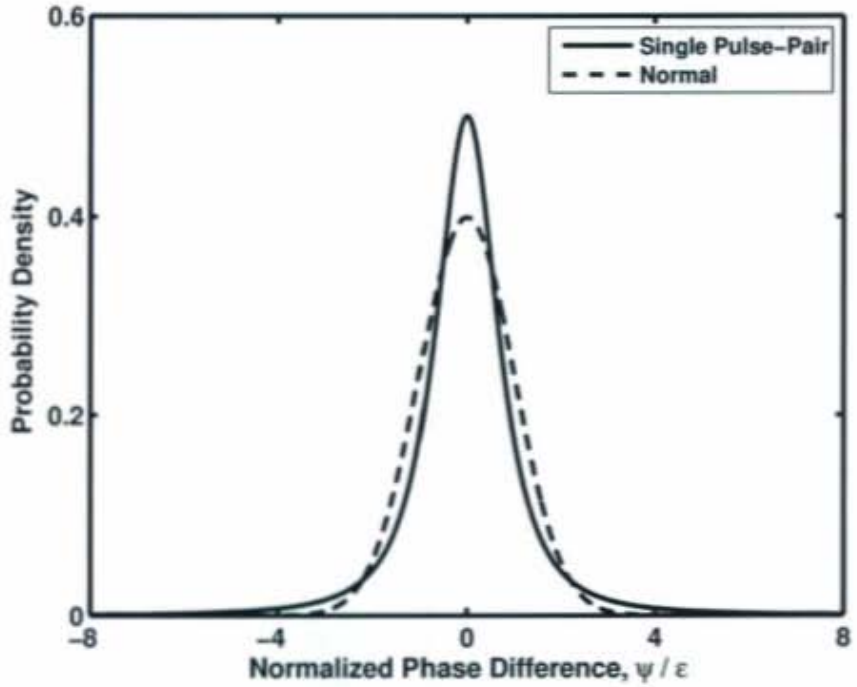

Figure 4.2: Comparison of the single pulse-pair phase distribution with a standard normal distribution in the limit $\rho \to 1$. Phase is normalized by ε.

Equation (4.18) is a Pearson Type VII distribution (Pearson, 1916)

$$p(x) = \frac{\Gamma(m)}{\alpha\sqrt{\pi}\,\Gamma(m-\frac{1}{2})}\left[1+\left(\frac{x}{\alpha}\right)^2\right]^{-m} \tag{4.19}$$

with parameters m and α given by $3/2$ and ε, respectively.

As $\varepsilon \to 0$, the peak value of (4.18) tends to infinity, resulting in an impulse at $\psi = 0$. To visualize the shape of the limiting distribution, let x represent the normalized phase difference ψ/ε, so that

$$p(x) = \frac{1}{2(1+x^2)^{3/2}}. \tag{4.20}$$

Equation (4.20) is compared with a standard normal distribution in Figure 4.2. It is evident that in the limit $\rho \to 1$, the single pulse-pair phase distribution has a higher peak and broader tails compared to a normal distribution.

In Figure 4.3, moments of the single pulse-pair phase distribution were evaluated by numerically integrating expressions of the form

$$\mu_k = \int_{-\pi}^{\pi} \psi^k \, p(\psi) \, d\psi \tag{4.21}$$

where μ_k denotes the k^{th} moment and $p(\psi)$ is given by (4.16). An analytical expression for the second moment can also be found in Bamler and Hartl (1998). In Figure 4.3a, the standard deviation

$$\sigma_\psi = \sqrt{\mu_2} \tag{4.22}$$

is compared with σ_p from perturbation analysis, i.e. (4.9) with $M = 1$. The ratio σ_ψ / σ_p is plotted in Figure 4.3b.

Kurtosis of a probability distribution is defined as (Abramowitz and Stegun, 1972, p. 928)

$$\beta_2 = \frac{\mu_4}{(\mu_2)^2}. \tag{4.23}$$

Kurtosis is a useful statistic for identifying non-normal distributions since β_2 is 3 for all normal distributions. The kurtosis of (4.16) tends to infinity as $\rho \to 1$. It is therefore more convenient to plot the reciprocal of kurtosis $1/\beta_2$ in Figure 4.4. Although β_2 is 3 when ρ equals 0.56, the normalized sixth moment is 12.2 rather than 15 characteristic of a normal distribution. The single pulse-pair phase distribution is therefore non-normal for all values of ρ.

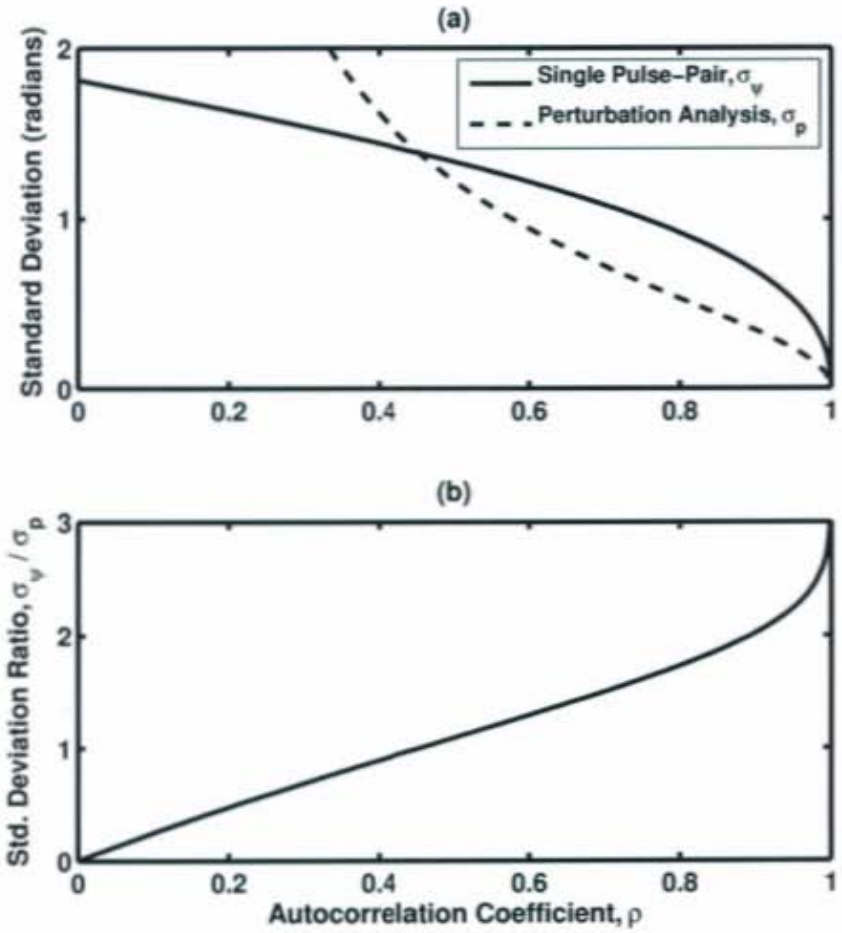

Figure 4.3: Standard deviation of the single pulse-pair phase distribution. In (a), the solid line represents σ_ψ for the distribution specified by (4.16). The dashed line represents σ_p from perturbation analysis, i.e. (4.9) with $M = 1$. In (b), the ratio σ_ψ/σ_p is plotted.

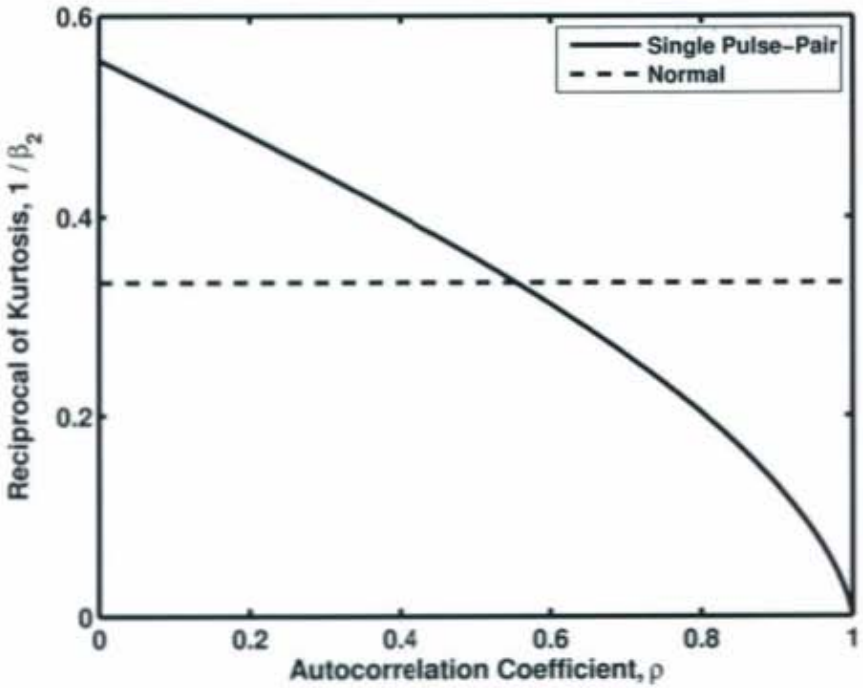

Figure 4.4: Reciprocal of kurtosis for the single pulse-pair phase distribution. The solid line represents (4.23) for the distribution specified by (4.16). The dashed line represents the kurtosis of a normal distribution.

4.4 Simulation of a Gaussian random process

Numerical simulation of a Gaussian random process was performed using the `randn` generator in MATLAB, as described in Dillon et al. (2011). For a Gaussian power spectrum, the backscatter autocorrelation sequence R_k is given by (4.6) and (4.7),

$$R_k = \sigma^2 \rho^{k^2} e^{i\phi k}. \tag{4.24}$$

Let $\boldsymbol{\zeta} = [\zeta_1 \ldots \zeta_L]^T$ denote an ensemble of L independent identically distributed samples from a complex Gaussian distribution with zero mean and unit variance, where the superscript T denotes the matrix transpose. Simulated backscatter samples $\mathbf{z} = [z_1 \ldots z_L]^T$ were generated using the transformation $\mathbf{z} = \mathbf{U}^*\boldsymbol{\zeta}$ where $\mathbf{U}^*$ is obtained from Cholesky decomposition of the desired covariance matrix $\mathbf{C}_z$ (Kay, 1993, chap. 15),

$$\mathbf{C}_z = \begin{bmatrix} R_0 & R_{-1} & \cdots & R_{-(L-1)} \\ R_1 & R_0 & \cdots & R_{-(L-2)} \\ \vdots & \vdots & \ddots & \vdots \\ R_{L-1} & R_{L-2} & \cdots & R_0 \end{bmatrix}. \tag{4.25}$$

Phase estimates were generated from 3×10^7 simulated ensembles with length M equal to 1, 2, 3, 5, 7, and 9 pulse-pairs. In order to obtain time series for the phase difference, ϕ was set to zero in (4.24) so that $\psi_n = \hat{\phi}_n$. Autocorrelation coefficients included the interval from 0 to 0.98 in increments of 0.02, and additional values of 0.99, 0.995, and 0.999. For each pair (ρ, M), second and fourth sample moments were calculated from the time series $\{\psi_n\}$ as follows:

$$\hat{\mu}_k = \frac{1}{N}\sum_{n=1}^{N}(\psi_n)^k \tag{4.26}$$

where N is the total number of simulated pings. Phase standard deviation and kurtosis were calculated from (4.22) and (4.23) using estimated moments from (4.26). Phase standard deviation σ_ψ and the ratio σ_ψ/σ_p are plotted as a function of the autocorrelation coefficient in Figure 4.5. The reciprocal of kurtosis is plotted in Figure 4.6.

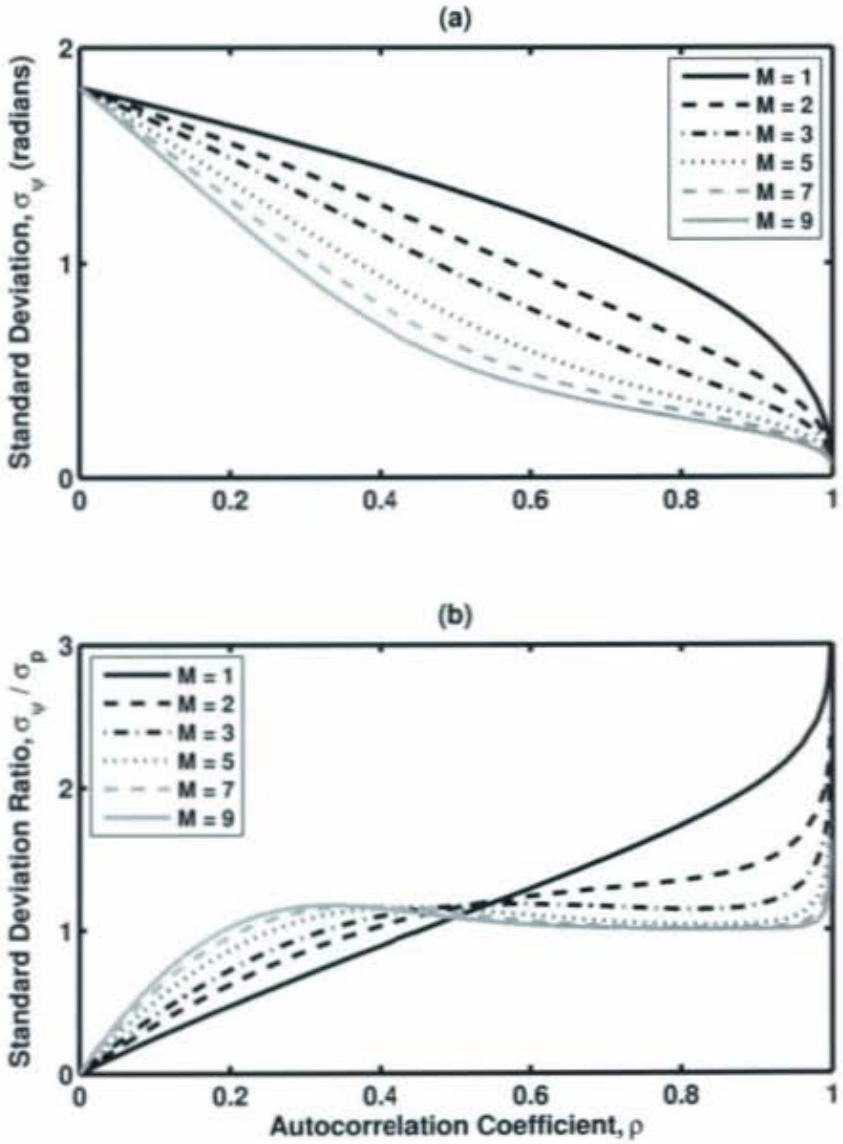

Figure 4.5: Phase standard deviation from simulations of a Gaussian random process. In (a), the standard deviation σ_ψ is estimated from the second sample moment. In (b), the ratio σ_ψ/σ_p is plotted, where σ_p is given by (4.9).

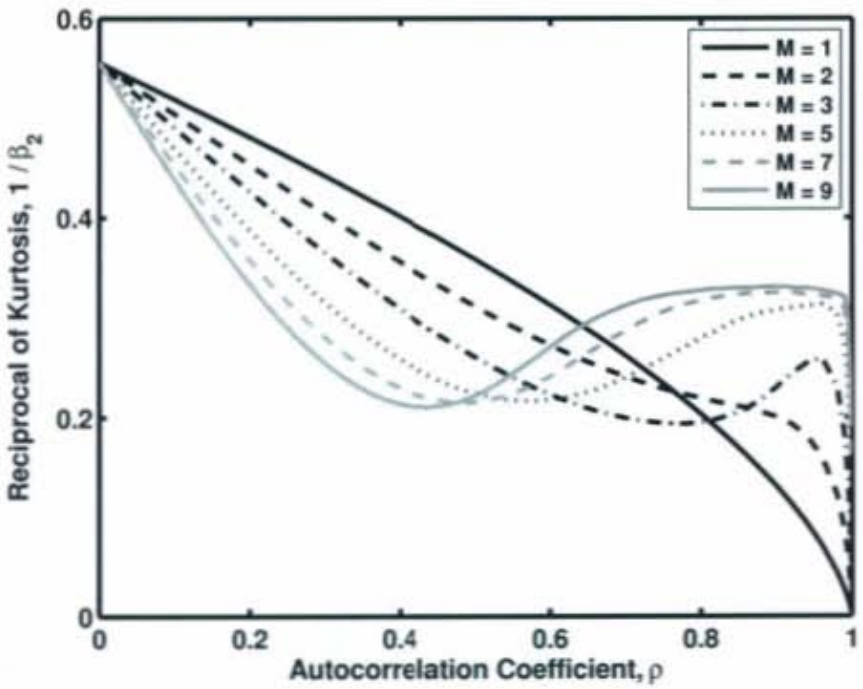

Figure 4.6: Reciprocal of phase kurtosis from simulations of a Gaussian random process. Kurtosis is estimated from second and fourth sample moments of the time series.

4.5 Coherent Doppler sonar model

Numerical simulation of steady flow was performed using the coherent Doppler sonar model described in Zedel (2008). The model simulates pulse-to-pulse coherent scattering from a cloud of moving particles for arbitrary multistatic sonar geometries. Physical effects such as spherical spreading, acoustic absorption, frequency-dependent beam patterns, transducer frequency response, and receiver noise are included in the model. The model supports simulation of arbitrary pulse shapes, including the use of multiple carrier frequencies.

Simulations were performed for a monostatic sonar measuring horizontal velocities of 0.5, 1.5, 3.0, and 4.5 m s^{-1}. In the model, the sonar was tilted 5° from vertical and the receiver SNR was set to 20 dB. Parameters for the coherent Doppler sonar simulation are listed in Table 4.1.

Table 4.1: Parameters for the coherent Doppler sonar simulation.

Parameter	**Value**
Transducer centre frequency	1.7 MHz
Transducer bandwidth	1.0 MHz
Receiver bandwidth	250 kHz
Carrier frequency	1.8 MHz
Transmit pulse length	4 μs
Ping interval	1.5 ms
Transducer diameter	2 cm
Sonar tilt angle	5°
Particle number density	4720 L^{-1}
Receiver signal-to-noise ratio	20 dB
Simulation time step	12.5 ns
Simulation time	300 s

The model was configured to record the result from each ping in addition to calculating pulse-pair averages. For each flow speed, the autocorrelation coefficient was approximated by averaging over all simulated pings,

$$\rho \approx \frac{1}{\sigma^2}\left|\frac{1}{N-1}\sum_{n=1}^{N-1} z_n^* z_{n+1}\right|, \tag{4.27}$$

where σ^2 is the variance of the backscatter sequence $\{z_n\}$ and $N = 2 \times 10^5$ is the total number of simulated pings. The autocorrelation coefficient for each flow speed is listed in Table 4.2.

Table 4.2: Estimated autocorrelation coefficients from coherent Doppler sonar simulation.

Speed (m s^{-1})	Autocorrelation Coefficient
0.5	0.985
1.5	0.888
3.0	0.633
4.5	0.366

In order to calculate phase differences $\psi_n = \hat{\phi}_n - \phi$, the pulse-to-pulse phase shift ϕ was approximated by averaging over all simulated pings,

$$\phi \approx \angle \left(\frac{1}{N-1} \sum_{n=1}^{N-1} z_n^* z_{n+1} \right). \tag{4.28}$$

Standard deviation σ_ψ of the time series $\{\psi_n\}$ is plotted in Figure 4.7 for ensemble lengths M from 1 to 9 pulse-pairs. Results from coherent Doppler sonar simulations are indicated with circles that lie on the corresponding curves for simulations of a Gaussian random process from Figure 4.5a.

4.6 Discussion

The derivation of the single pulse-pair phase distribution assumed a complex Gaussian probability distribution for each backscatter sample. However, it was not necessary to assume a Gaussian power spectrum for the time series since the formula only depends on the expected autocorrelation at a lag of one pulse-to-pulse interval. The resulting phase distribution describes a family of symmetric non-normal probability distributions defined on the interval $[-\pi, \pi]$. As the autocorrelation coefficient ρ varies from zero to one, the phase distribution transitions from a uniform distribution to a

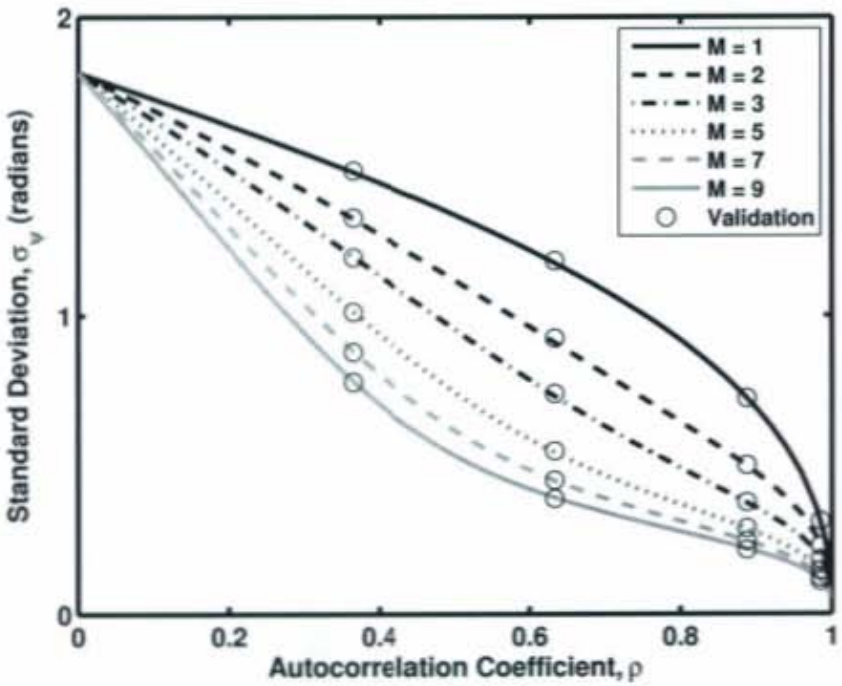

Figure 4.7: Phase standard deviation from coherent Doppler sonar simulations. Autocorrelation coefficients for flow speeds of 0.5, 1.5, 3.0, and 4.5 m s^{-1} are listed in Table 4.2. Results from coherent Doppler sonar simulations are indicated with circles that lie on the corresponding curves for simulations of a Gaussian random process in Figure 4.5a.

Pearson Type VII distribution.

Phase standard deviation and kurtosis were determined via numerical simulation of a Gaussian random process for ensemble lengths ranging from 1 to 9 pulse-pairs. Simulation results for single pulse-pairs ($M = 1$) match the theoretical predictions in Section 4.3. Figure 4.5b shows that the range of applicability of the perturbation analysis formula (4.9) increases with ensemble length. For M less than 4, the standard deviation ratio σ_ψ/σ_p differs from unity by at least 5% for all values of the autocorrelation coefficient. However, for M greater than 6, Figure 4.5b indicates that σ_ψ is

within 5% of σ_p in the interval $0.62 \leq \rho \leq 0.96$. The fact that σ_ψ and σ_p do not agree in the limit $\rho \to 1$ is usually not an area of concern when designing an instrument since capability limits are determined by the performance at low correlations.

The plot of kurtosis in Figure 4.6 demonstrates that the phase distribution is non-normal for all values of ρ when the ensemble length M is less than 6 pulse-pairs. For M greater than 6, kurtosis is within 5% of that of a normal distribution over the interval $0.80 \leq \rho \leq 0.98$. In the limit $\rho \to 1$ when pulse-pairs are perfectly correlated, the phase distribution is unaffected by averaging multiple pulse-pairs. Therefore, kurtosis tends to infinity in the limit $\rho \to 1$ for all values of M.

The coherent Doppler sonar model in Zedel (2008) does not assume that backscatter samples obey a Gaussian probability distribution with Gaussian power spectrum. For simulation of steady flow, no statistical assumptions about particle motion are made other than that particles move uniformly with constant velocity. The model describes the physics of coherent scattering and accounts for the sonar geometry and operating parameters, unlike the simulations of a Gaussian random process in Section 4.4. Simulations of steady flow confirmed the predictions of phase standard deviation from a Gaussian random process. Figure 4.7 shows that simulation with a Gaussian random process is sufficient to predict the reduction in standard deviation achieved by pulse-pair averaging. Since simulations of the Gaussian random process were performed without additive noise, agreement in Figure 4.7 also confirms that receiver noise with a 20 dB SNR does not affect phase standard deviation.

Non-normality of the phase distribution implies that any analytical expression for phase must account for the kurtosis observed in Figure 4.6. The Pearson Type VII distribution has the desirable property that standard deviation and kurtosis may be

specified independently. However, this distribution is defined on the entire real line, whereas phase measurements lie in the interval $[-\pi, \pi]$. Although the peak of the Pearson Type VII distribution is narrow as $\varepsilon \to 0$, higher order moments depend on the broad tails of the distribution. For example, second and fourth moments of (4.19) with m equal to 3/2 are infinite, whereas second and fourth moments of the phase distribution are necessarily bounded above by $\pi^2/3$ and $\pi^4/5$ for a uniform distribution. In order to represent the phase distribution for ensemble lengths less than 10 pulse-pairs, it would be useful to construct a family of symmetric probability distributions defined on a finite interval where standard deviation and kurtosis may be specified independently. A suitable re-parameterization of the single pulse-pair distribution (4.16) may provide such a family.

4.7 Conclusions

A formula has been presented for the distribution of a single pulse-pair phase measurement for coherent Doppler sonar. Evaluation of second and fourth moments showed that the single pulse-pair phase distribution is non-normal for all values of the autocorrelation coefficient ρ. In particular, the phase distribution is described by a Pearson Type VII distribution in the limit $\rho \to 1$. Numerical simulation of a Gaussian random process was used to determine phase standard deviation and kurtosis for ensemble lengths ranging from 1 to 9 pulse-pairs. Validity of the Gaussian random process was confirmed using a high fidelity coherent Doppler sonar model. For ensemble lengths M less than 4 pulse-pairs, the ratio of phase standard deviation to that predicted by perturbation analysis differs from unity by at least 5% for all

values of the autocorrelation coefficient. However, for M greater than 6, perturbation analysis is within 5% when ρ lies in the interval from 0.62 to 0.96. Calculation of kurtosis demonstrated that the phase distribution is non-normal for M less than 6. For M greater than 6, kurtosis is within 5% of that of a normal distribution for ρ in the interval from 0.80 to 0.98. In the limit $\rho \to 1$ when pulse-pairs are perfectly correlated, kurtosis tends to infinity for all ensemble lengths considered.

4A Single pulse-pair phase distribution

The derivation follows a similar approach as Davenport and Root (1987, chap. 8), but makes use of a more direct evaluation of the joint PDF. To derive the distribution for the autocorrelation phase of a single pulse-pair,

$$\tilde{\phi} = \angle z_2 - \angle z_1, \tag{4.29}$$

let x and y represent real and imaginary parts of each complex backscatter sample $z = x + iy$. The real-valued random vector $\mathbf{X} = [x_1 \; x_2 \; y_1 \; y_2]^T$ is assumed to be described by a joint Gaussian distribution

$$p(\mathbf{X}) = \frac{1}{4\pi^2\sqrt{\det \mathbf{C}_X}} \exp\left(-\frac{1}{2}\mathbf{X}^T\mathbf{C}_X^{-1}\mathbf{X}\right) \tag{4.30}$$

with zero mean and covariance matrix $\mathbf{C}_X$ given by (Kay, 1993, chap. 15)

$$\mathbf{C}_X = \frac{\sigma^2}{2}\begin{bmatrix} 1 & \rho\cos\phi & 0 & \rho\sin\phi \\ \rho\cos\phi & 1 & -\rho\sin\phi & 0 \\ 0 & -\rho\sin\phi & 1 & \rho\cos\phi \\ \rho\sin\phi & 0 & \rho\cos\phi & 1 \end{bmatrix}. \tag{4.31}$$

It is assumed that $\rho < 1$ for the inverse of (4.31) to exist. Substituting (4.31) in (4.30) and transforming to polar coordinates results in the joint PDF

$$p(r_1, r_2, \theta_1, \theta_2) = \frac{r_1 r_2}{\pi^2 \sigma^4 \varepsilon^2} \exp\left(\frac{-r_1^2 - r_2^2 + 2Ar_1 r_2}{\sigma^2 \varepsilon^2}\right) \tag{4.32}$$

where $A = \rho\cos(\theta_2 - \theta_1 - \phi)$ and $\varepsilon^2 = 1 - \rho^2$. The joint distribution for θ_1 and θ_2 is obtained from

$$p(\theta_1, \theta_2) = \int_0^\infty \int_0^\infty p(r_1, r_2, \theta_1, \theta_2)\, dr_1 dr_2. \tag{4.33}$$

Integration over the (r_1, r_2) first quadrant is performed using the transformation $r_1 = R\cos\Theta$ and $r_2 = R\sin\Theta$,

$$p(\theta_1, \theta_2) = \frac{1}{2\pi^2 \sigma^4 \varepsilon^2} \int_0^{\frac{\pi}{2}} \int_0^\infty R^3 \sin 2\Theta\, e^{-\alpha R^2} dR\, d\Theta, \tag{4.34}$$

where α is a positive coefficient given by

$$\alpha = \frac{1 - A\sin 2\Theta}{\sigma^2 \varepsilon^2}. \tag{4.35}$$

Integrating by parts produces the identity

$$\int_0^\infty R^3 e^{-\alpha R^2} dR = \frac{1}{2\alpha^2}. \tag{4.36}$$

Applying (4.36) to (4.34) results in

$$p(\theta_1, \theta_2) = \frac{1-\rho^2}{4\pi^2} \int_0^{\pi/2} \frac{\sin 2\Theta}{(1 - A\sin 2\Theta)^2} \, d\Theta. \tag{4.37}$$

Let $t = \frac{\pi}{2} - 2\Theta$, so that

$$p(\theta_1, \theta_2) = \frac{1-\rho^2}{8\pi^2} \int_{-\pi/2}^{\pi/2} \frac{\cos t}{(1 - A\cos t)^2} \, dt. \tag{4.38}$$

The distribution for the difference $\hat{\phi} = (\theta_2 - \theta_1) \bmod 2\pi$ is given by (Pawula et al., 1982, eq. (6))

$$p(\hat{\phi}) = \int_{-\pi}^{\pi} p(\theta_1, \theta_1 + \hat{\phi}) \, d\theta_1. \tag{4.39}$$

Substituting (4.38) in (4.39) and changing the order of integration results in

$$p(\hat{\phi}) = \frac{1-\rho^2}{8\pi^2} \int_{-\pi/2}^{\pi/2} \int_{-\pi}^{\pi} \frac{\cos t}{(1 - a\cos t)^2} \, d\theta_1 \, dt \tag{4.40}$$

where $a = \rho\cos(\hat{\phi} - \phi)$. Since the integrand does not depend on θ_1, (4.40) simplifies to

$$p(\hat{\phi}) = \frac{1-\rho^2}{4\pi} \int_{-\pi/2}^{\pi/2} \frac{\cos t}{(1 - a\cos t)^2} \, dt. \tag{4.41}$$

Equation (4.41) is a special case of Pawula et al. (1982, eq. (B-6)). The distribution is a symmetric function of the phase difference $\psi = \hat{\phi} - \phi$. We therefore adopt the

notation $p(\psi)$ for $p(\tilde{\phi})$.

The integral in (4.41) is evaluated using the identity from Gradshteyn and Ryzhik (2007, eqs. (2.553-3), (2.554-1))

$$\int \frac{\cos x\, dx}{(1-a\cos x)^2} = \frac{1}{1-a^2}\left[\frac{\sin x}{1-a\cos x} + \frac{2a}{\sqrt{1-a^2}}\tan^{-1}\left(\frac{(1+a)\tan\frac{x}{2}}{\sqrt{1-a^2}}\right)\right]. \quad (4.42)$$

Applying (4.42) to (4.41) yields

$$p(\psi) = \frac{1-\rho^2}{2\pi(1-a^2)}\left[1 + \frac{2a}{\sqrt{1-a^2}}\tan^{-1}\left(\frac{1+a}{\sqrt{1-a^2}}\right)\right]. \quad (4.43)$$

The following identity is derived from Gradshteyn and Ryzhik (2007, eq. (1.628-2)):

$$2\tan^{-1}\left(\frac{1+a}{\sqrt{1-a^2}}\right) = \pi - \cos^{-1} a. \quad (4.44)$$

Substituting (4.44) in (4.43) produces the final result,

$$p(\psi) = \frac{1-\rho^2}{2\pi(1-a^2)}\left[1 + \frac{a}{\sqrt{1-a^2}}\left(\pi - \cos^{-1} a\right)\right]. \quad (4.45)$$

4B Limiting form of the phase distribution

To examine the limit $\rho \to 1$, let $\varepsilon = \sqrt{1-\rho^2}$ so that $\varepsilon \to 0$ as $\rho \to 1$. A small angle approximation is used for ψ since phase becomes concentrated in a narrow peak as

$\rho \to 1$. The left hand term in (4.45) is approximated as

$$\begin{aligned} \frac{1-\rho^2}{1-a^2} &= \frac{\varepsilon^2}{\varepsilon^2+\rho^2\sin^2\psi} \\ &\approx \frac{\varepsilon^2}{\varepsilon^2+\psi^2}. \end{aligned} \tag{4.46}$$

Likewise,

$$\frac{a}{\sqrt{1-a^2}} \approx \frac{1}{\sqrt{\varepsilon^2+\psi^2}}. \tag{4.47}$$

In the limit $\rho \to 1$, the following approximation holds:

$$\cos^{-1} a \approx |\psi|. \tag{4.48}$$

Therefore,

$$\pi - \cos^{-1} a \approx \pi \tag{4.49}$$

when ψ is a small angle. Substituting (4.46), (4.47), and (4.49) for the corresponding terms in (4.45) results in

$$p(\psi) \approx \frac{\varepsilon^2}{2\pi(\varepsilon^2+\psi^2)}\left[1+\frac{\pi}{\sqrt{\varepsilon^2+\psi^2}}\right]. \tag{4.50}$$

For $\varepsilon \to 0$ and small values of ψ, the right hand term of (4.50) dominates. The resulting expression is

$$p(\psi) \approx \frac{1}{2\varepsilon}\frac{1}{(1+(\psi/\varepsilon)^2)^{3/2}}. \tag{4.51}$$

Numerical evaluation indicates that in the interval $[-5\varepsilon, 5\varepsilon]$, (4.51) is within 1% of (4.45) for $\rho \geq 0.997$.

Bibliography

Abramowitz, M. and Stegun, I. A., editors (1972). *Handbook of Mathematical Functions with Formulas, Graphs, and Mathematical Tables.* Dover Publications.

Bamler, R. and Hartl, P. (1998). Synthetic aperture radar interferometry. *Inverse Problems*, 14(4):R1–R54.

Davenport, W. B. and Root, W. L. (1987). *An Introduction to the Theory of Random Signals and Noise.* Wiley–IEEE Press.

Dillon, J., Zedel, L., and Hay, A. E. (2011). Asymptotic properties of an autocorrelation coefficient for coherent Doppler sonar. *Journal of Atmospheric and Oceanic Technology*, 28(7):966–973.

Garbini, J. L., Forster, F. K., and Jorgensen, J. E. (1982). Measurement of fluid turbulence based on pulsed ultrasound techniques. Part 1. Analysis. *Journal of Fluid Mechanics*, 118:445–470.

Gradshteyn, I. S. and Ryzhik, I. M. (2007). *Tables of Integrals, Series, and Products.* Academic Press, seventh edition.

Hay, A. E., Zedel, L., Craig, R., and Paul, W. (2008). Multi-frequency, pulse-to-pulse coherent Doppler sonar profiler. In *Proceedings of the IEEE/OES 9th Working Conference on Current Measurement Technology*, pages 25–29.

Just, D. and Bamler, R. (1994). Phase statistics of interferograms with applications to synthetic aperture radar. *Applied Optics*, 33(20):4361–4368.

Kay, S. M. (1993). *Fundamentals of Statistical Signal Processing: Estimation Theory*, volume 1. Prentice-Hall PTR.

Lank, G. W., Reed, I. S., and Pollon, G. E. (1973). A semicoherent detection and Doppler estimation statistic. *IEEE Transactions on Aerospace and Electronic Systems*, AES-9(2):151–165.

Lhermitte, R. and Serafin, R. (1984). Pulse-to-pulse coherent Doppler sonar signal processing techniques. *Journal of Atmospheric and Oceanic Technology*, 1(4):293–308.

Lohrmann, A., Hackett, B., and Røed, L. P. (1990). High resolution measurements of turbulence, velocity and stress using a pulse-to-pulse coherent sonar. *Journal of Atmospheric and Oceanic Technology*, 7(1):19–37.

Miller, K. S. and Rochwarger, M. M. (1972). A covariance approach to spectral moment estimation. *IEEE Transactions on Information Theory*, IT-18(5):588–596.

Newhouse, V. L., Bendick, P. J., and Varner, L. W. (1976). Analysis of transit time effects on Doppler flow measurement. *IEEE Transactions on Biomedical Engineering*, BME-23(5):381–387.

Newhouse, V. L., Varner, L. W., and Bendick, P. J. (1977). Geometrical spectrum broadening in ultrasonic Doppler systems. *IEEE Transactions on Biomedical Engineering*, BME-24(5):478–480.

Nitzpon, H. J., Rajaonah, J. C., Burckhardt, C. B., Dousse, B., and Meister, J. J. (1995). A new pulsed wave Doppler ultrasound system to measure blood velocities beyond the Nyquist limit. *IEEE Transactions on Ultrasonics, Ferroelectrics, and Frequency Control*, 42(2):265–279.

Pawula, R. F., Rice, S. O., and Roberts, J. H. (1982). Distribution of the phase angle between two vectors perturbed by Gaussian noise. *IEEE Transactions on Communications*, COM-30(8):1828–1841.

Pearson, K. (1916). Mathematical contributions to the theory of evolution. XIX. Second supplement to a memoir on skew variation. *Philosophical Transactions of the Royal Society of London. Series A, Containing Papers of a Mathematical or Physical Character*, 216:429–457.

Rowe, F. D., Deines, K. L., and Gordon, R. L. (1986). High resolution current profiler. In *Proceedings of the IEEE 3rd Working Conference on Current Measurement*, volume 3, pages 184–189.

Woodman, R. F. and Hagfors, T. (1969). Methods for the measurement of vertical ionospheric motions near the magnetic equator by incoherent scattering. *Journal of Geophysical Research*, 74(5):1205–1212.

Zedel, L. (2008). Modeling pulse-to-pulse coherent Doppler sonar. *Journal of Atmospheric and Oceanic Technology*, 25(10):1834–1844.

Zedel, L. and Hay, A. E. (2010). Resolving velocity ambiguity in multifrequency, pulse-to-pulse coherent Doppler sonar. *IEEE Journal of Oceanic Engineering*, 35(4):847–851.

Zedel, L., Hay, A. E., Cabrera, R., and Lohrmann, A. (1996). Performance of a single-beam pulse-to-pulse coherent Doppler profiler. *IEEE Journal of Oceanic Engineering*, 21(3):290–297.

Zrnić, D. S. (1977). Spectral moment estimates from correlated pulse pairs. *IEEE Transactions on Aerospace and Electronic Systems*, AES-13(4):344–354.

Chapter 5 Preamble

This chapter describes the MAP velocity estimator and presents a method for automatically determining the smoothing parameter from examination of the measurement time series. In this chapter, three of the thesis objectives are achieved: (i) measurement noise is suppressed for turbulent flow, (ii) the estimator is validated using measurements from particle image velocimetry, and (iii) the estimator is free from empirically determined constants.

This chapter presents a paper titled "Automatic Tuning of a Velocity Estimator for Pulse-to-Pulse Coherent Doppler Sonar." It has been published in the *Proceedings of the IEEE/OES 10th Current, Waves, and Turbulence Measurement Workshop* (Dillon et al., 2011b).

Chapter 5

Measurement Noise Suppression

5.1 Abstract

Pulse-to-pulse coherent Doppler sonar is capable of measuring simultaneous profiles of veloctiy and sediment concentration in turbulent suspensions. However, the presence of measurement noise introduces biases when turbulence statistics are calculated from the fluctuating component of velocity. In order to further develop coherent Doppler sonar as a tool for turbulence measurement, a velocity estimator based on Maximum A Posteriori (MAP) estimation has been developed. The estimator optimally combines measurements from multiple acoustic carrier frequencies and multiple transducers. Data fusion is achieved using a probabilistic approach, whereby measurements are combined numerically to derive a velocity likelihood function. The only parameter which must be chosen by the user is a smoothing factor that describes the diffusion of velocity (in a probabilistic sense) from sample to sample in time. A method is presented for automatically determining the smoothing parameter from examination

of the spectrum of a representative segment of the measurement time series. Results are presented from a laboratory turbulent jet in which velocity was measured simultaneously with multi-frequency coherent Doppler sonar and particle image velocimetry (PIV). Time series and turbulence spectra from PIV are compared to those obtained with conventional Doppler signal processing and MAP velocity estimation. It is shown that automatic tuning of the estimator results in a velocity time series where measurement noise is suppressed while high frequency turbulent fluctuations are retained.

5.2 Introduction

Pulse-to-pulse coherent Doppler sonar has been widely used to study transport and mixing processes in the ocean. Applications include tidal flows (Lhermitte, 1983), surface boundary layer processes (Gargett, 1989), surface wave breaking (Veron and Melville, 1999), internal waves (Plueddemann, 1992), sediment transport (Smyth et al., 2002), and turbulence measurement (Lohrmann et al., 1990). High frequency (1 to 10 MHz) coherent Doppler sonar is a promising tool for obtaining near-bed profiles of shear stress and sediment flux in the ocean bottom boundary layer (Thorne and Hanes, 2002). Recent studies, for example, have focused on estimation of bottom friction from measurements of near-bed turbulence profiles (Hay, 2008).

The performance and limitations of coherent Doppler sonar have been extensively explored through numerical simulations (Zedel, 2008) and in the laboratory (Zedel et al., 1996). Measurement errors are caused by pulse-to-pulse backscatter decorrelation from (i) scatterer advection through the sample volume, (ii) velocity shear and

turbulence within the sample volume, (iii) phase distortion of the transmitted wave, and (iv) electronic noise in the receiver circuitry (Zedel et al., 1996; Hurther and Lemmin, 2001).

Doppler measurement errors consist of both large amplitude instantaneous spikes and continuous random fluctuations. Both types of error cause the measured velocity variance to exceed the true variance of scatterer velocity. In order to obtain accurate statistics, for example in turbulence measurement, random errors must be suppressed. While averaging and low pass filtering attenuate measurement errors, there is an undesirable reduction in sample rate and bandwidth, and high frequency turbulent fluctuations are also suppressed. Noise suppression methods aim to improve velocity estimates while preserving the sample rate and bandwidth of the original data.

Noise suppression is possible when redundant measurements with uncorrelated measurement errors are available. An example of this approach is the use of two partially overlapping or non-overlapping sample domains (Garbini et al., 1982). Velocity measurements from two closely spaced regions along the acoustic beam may be cross-correlated to attenuate uncorrelated noise sources. However, in turbulent flow, spatial decorrelation of velocity limits the allowable separation of the sample volumes.

Redundant measurements with uncorrelated errors may also be obtained with additional acoustic receivers. By using four receivers to measure three components of velocity, redundant vertical velocity calculations have been used to reduce the noise contribution in turbulence statistics (Hurther and Lemmin, 2001). Redundant receivers have also been used in four-beam acoustic Doppler current profilers (Rowe et al., 1986) and a five-transducer profiling sonar (Hay et al., 2008). Another method

for obtaining redundant velocity measurements with uncorrelated noise sources involves simultaneous transmission of two closely spaced acoustic carrier frequencies. Experiments in oscillating grid turbulence have shown that a carrier frequency shift of 10% is sufficient to achieve an order of magnitude in noise suppression (Hurther and Lemmin, 2008).

In order to further develop coherent Doppler sonar as a tool for turbulence measurement, a velocity estimator has been developed based on the Bayesian technique of Maximum A Posteriori (MAP) estimation (Kay, 1993). The MAP velocity estimator shares many similarities with a Kalman smoother: (i) the estimator processes a time series recursively, (ii) a model is used to provide prior statistical knowledge, (iii) the estimator produces its own performance measure, and (iv) estimator lag is eliminated via application both forward and backward in time. However, unlike a Kalman smoother, the MAP velocity estimator makes use of non-Gaussian probability density functions and is inherently nonlinear. The motivation for using MAP estimation is that velocity ambiguity causes the velocity likelihood function to be multi-modal; thus a Gaussian representation is inappropriate.

The MAP velocity estimator optimally combines measurements from multiple acoustic carrier frequencies and multiple transducers. Data fusion is achieved using a probabilistic approach, whereby measurements are combined numerically to derive a velocity likelihood function. The estimation framework accommodates commonly used sonar geometries such as one-dimensional single beam systems, acoustic Doppler current profilers (ADCPs) with divergent beams, three-dimensional velocity point sensors, and profiling sonars. While the focus of this chapter is on monostatic multi-frequency coherent Doppler sonar, the results are equally applicable to single-

frequency and staggered pulse repetition frequency (PRF) systems with multistatic geometries.

The algorithm is specified by physical parameters of the sonar and is free from empirically determined instrument-specific or application-specific thresholds or constants. The only parameter which must be chosen by the user is a smoothing factor that describes the diffusion of velocity (in a probabilistic sense) from sample to sample in time. In this chapter, a method is presented for automatically determining the smoothing parameter from examination of the spectrum of a representative segment of the measurement time series.

The method is evaluated using results from a laboratory turbulent jet experiment where velocity was measured simultaneously with multi-frequency coherent Doppler sonar and particle image velocimetry (PIV). Automatic tuning of the estimator results in a velocity time series where measurement noise is suppressed while high frequency turbulent fluctuations are retained.

5.3 MAP velocity estimation

Maximum A Posteriori (MAP) estimation is one of several parameter estimation methods based on Bayesian inference. In contrast with classical statistical estimation, Bayesian methods treat a parameter to be estimated as a random variable rather than a deterministic but unknown constant (Box and Tiao, 1973). The motivation for the Bayesian approach is that prior knowledge of the probability density function (PDF) may be used to improve estimator performance. Once observations have been made, Bayes' theorem permits calculation of the posterior PDF which expresses the

likelihood of a particular parameter value given the measurements that have been observed. An estimate is then calculated as a function of the posterior PDF, for example as the location of the maximum value in MAP estimation (Kay, 1993).

Backscatter autocorrelation is the fundamental measurement in pulse-to-pulse coherent Doppler sonar. For a sequence $\{z_n\}$ of complex-valued backscatter samples, the autocorrelation at a lag of one pulse-to-pulse interval is

$$R(\tau) = E(z_n^* z_{n+1}) \tag{5.1}$$

where E denotes expected value, * denotes complex conjugation, and τ is the time interval between successive acoustic transmissions. Velocity is proportional to the pulse-to-pulse phase shift $\phi = \angle R(\tau)$ (Lohrmann et al., 1990),

$$v = \frac{c}{4\pi f_0 \tau}\phi; \quad \phi \in [-\pi, \pi] \tag{5.2}$$

where c is the speed of acoustic wave propagation and f_0 is the carrier frequency of the transmitted signal.

In practice, autocorrelation is estimated from a finite sequence of M pulse-pairs (Zrnić, 1977),

$$\hat{R}(\tau) = \frac{1}{M}\sum_{n=1}^{M} z_n^* z_{n+1}. \tag{5.3}$$

The phase $\hat{\phi}$ of the autocorrelation estimate $\hat{R}(\tau)$ is determined from real and imaginary components as follows:

$$\hat{\phi} = \angle \hat{R}(\tau) = \tan^{-1}\frac{\mathcal{I}(\hat{R}(\tau))}{\mathcal{R}(\hat{R}(\tau))}. \tag{5.4}$$

Corresponding to each phase measurement, an autocorrelation coefficient $\hat{\rho}$ may also be defined (Zedel et al., 1996),

$$\hat{\rho} = \frac{\left| \sum_{n=1}^{M} z_n^* z_{n+1} \right|}{\sum_{n=1}^{M} |z_n^* z_{n+1}|}. \tag{5.5}$$

The coefficient $\hat{\rho}$ provides a measure of data quality. Equation (5.5) implies that $0 \leq \hat{\rho} \leq 1$.

The unknown parameter to be estimated is the radial speed v (for monostatic sonar) or a velocity vector $\mathbf{v}$ (for multistatic sonar). The one-dimensional case is described in this chapter; the generalization to multiple transducers is presented in Chapter 6. For a multi-frequency system with N_f carrier frequencies, measurements consist of autocorrelation phases $\hat{\phi}_i$ and coefficients $\hat{\rho}_i$ corresponding to carrier frequencies f_i. The MAP velocity estimate is the location of the maximum value of the posterior PDF, denoted by (Kay, 1993, chap. 11)

$$\hat{v} = \arg \max_{v} p(v) \prod_{i=1}^{N_f} p(\hat{\phi}_i, \hat{\rho}_i \,|\, v). \tag{5.6}$$

The term $p(v)$ describes any prior knowledge of v that exists before measurements have been observed. The measurement PDFs $p(\hat{\phi}_i, \hat{\rho}_i \,|\, v)$ express the probability of observing measurements $\{\hat{\phi}_i, \hat{\rho}_i\}$ when velocity takes the value v. For the results presented in this chapter, measurement PDFs were determined from simulations of a Gaussian random process as described in Chapter 4 (Dillon et al., 2011b), with a correction for the bias of the autocorrelation coefficient from Chapter 3 (Dillon et al., 2011a). Example measurement PDFs are shown in Figure 5.1a for the jet

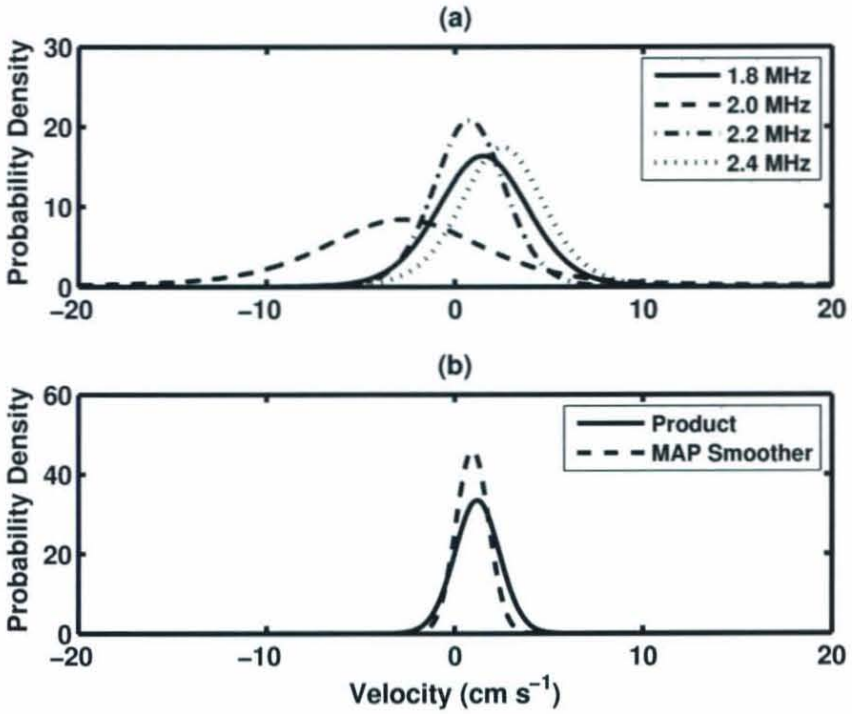

Figure 5.1: Example velocity likelihood functions from the jet tank experiment, showing: (a) multi-frequency measurement PDFs, and (b) product distribution and MAP smoother posterior PDF. In (a), the corresponding autocorrelation coefficients $\hat{\rho}$ are 0.73, 0.51, 0.84, and 0.82.

tank experiment described in Section 5.4. Autocorrelation coefficients in Figure 5.1a ranged from 0.51 to 0.84. The product PDF in Figure 5.1b represents the term $\prod p(\hat{\phi}_i, \hat{\rho}_i \,|\, v)$ in (5.6).

5.3.1 Velocity model

Prior information is derived from a model of the underlying random process. For velocity estimation, the model should express the inherent continuity of the time series in a simple and generic form to be applicable to many flows. It is not necessary to predict the long term evolution of velocity since the time series will ultimately be

determined by available measurements. The simplest continuous model for a velocity sequence $\{v_n\}$ is the diffusion process

$$v_{n+1} = v_n + \xi_n \tag{5.7}$$

where ξ is a discrete-time white Gaussian noise process with standard deviation σ. In order to apply (5.7) as a predictive model, the sonar sample interval must be less than the decorrelation time of the flow.

For each sample in the time series, measurements $\{\hat{\phi}_i, \hat{\rho}_i\}$ may be arranged as a vector $\boldsymbol{\mu}_n$. Let $\overline{p}_n^f(v)$ denote the forward time posterior PDF $p(v_n \mid \boldsymbol{\mu}_1, \ldots, \boldsymbol{\mu}_n)$ describing the likelihood of v_n occurring after the sequence of measurements $\{\boldsymbol{\mu}_1, \ldots, \boldsymbol{\mu}_n\}$. By assumption, the noise process ξ and velocity v are independent random variables. The probability distribution of a sum of independent variables is given by convolution of the distributions of the summands. Therefore, given a posterior PDF $\overline{p}_n^f(v)$, the predicted likelihood $p_{n+1}^f(v)$ is the convolution of $\overline{p}_n^f(v)$ with a Gaussian probability distribution,

$$p_{n+1}^f(v) = \frac{1}{\sigma\sqrt{2\pi}} \int \overline{p}_n^f(v-u) \exp\left(-\frac{u^2}{2\sigma^2}\right) du. \tag{5.8}$$

Convolution may be implemented on a discrete set of points by filtering the posterior PDF $\overline{p}_n^f(v)$ with a FIR filter having a Gaussian impulse response.

5.3.2 Filtering and smoothing

MAP velocity estimation can be implemented by filtering forward or backward in time, or by combining all available measurements in the form of a smoother. In each

case, the velocity likelihood function is initialized to be uniformly distributed on a finite interval that is assumed to include the expected range of observed velocities.

The forward time MAP velocity estimator is obtained by maximizing the posterior PDF as in (5.6),

$$\overrightarrow{p}_n^f(v) = p_n^f(v) \prod_{i=1}^{N_f} p(\tilde{\phi}_{n_i}, \tilde{\rho}_{n_i} \,|\, v), \tag{5.9}$$

$$\tilde{v}_n = \arg\max_v \overrightarrow{p}_n^f(v). \tag{5.10}$$

The forward time prior distribution $p_1^f(v)$ is initialized to be uniform and is updated using the convolution operation in (5.8).

The velocity model applies equally well to the time-reversed sequence since (5.7) implies that

$$v_{n-1} = v_n - \xi_{n-1}. \tag{5.11}$$

Let $\overleftarrow{p}_n^b(v)$ denote the backward time posterior PDF $p(v_n \,|\, \boldsymbol{\mu}_n, \ldots, \boldsymbol{\mu}_N)$ describing the likelihood of v_n occurring after the sequence of measurements $\{\boldsymbol{\mu}_N, \boldsymbol{\mu}_{N-1}, \ldots, \boldsymbol{\mu}_n\}$. Analogous to the forward time case, the backward time estimator is given by

$$\overleftarrow{p}_n^b(v) = p_n^b(v) \prod_{i=1}^{N_f} p(\tilde{\phi}_{n_i}, \tilde{\rho}_{n_i} \,|\, v), \tag{5.12}$$

$$\tilde{v}_n = \arg\max_v \overleftarrow{p}_n^b(v). \tag{5.13}$$

The backward time prior distribution $p_N^b(v)$ is initialized to be uniform and is updated as in (5.8),

$$p_{n-1}^b(v) = \frac{1}{\sigma\sqrt{2\pi}} \int \overleftarrow{p}_n^b(v-u) \exp\left(-\frac{u^2}{2\sigma^2}\right) du. \tag{5.14}$$

The terms $p_n^f(v)$ and $p_n^b(v)$ in (5.9) and (5.12) describe prior information gained from processing measurements $\{\boldsymbol{\mu}_1, \ldots, \boldsymbol{\mu}_{n-1}\}$ and $\{\boldsymbol{\mu}_{n+1}, \ldots, \boldsymbol{\mu}_N\}$, respectively.

Let $\overline{p}_n^s(v)$ denote the smoother posterior PDF $p(v_n \,|\, \boldsymbol{\mu}_1, \ldots, \boldsymbol{\mu}_N)$ describing the likelihood of v_n occurring after all measurements in the time series have been recorded. The MAP smoother is formed by combining the results from forward and backward filtering,

$$\overline{p}_n^s(v) = p_n^f(v)\, p_n^b(v) \prod_{i=1}^{N_f} p(\hat{\phi}_{n_i}, \hat{\rho}_{n_i} \,|\, v), \tag{5.15}$$

$$\hat{v}_n = \arg\max_v \overline{p}_n^s(v). \tag{5.16}$$

With this formulation, the smoother utilizes all available measurements to estimate v_n. The product $p_n^f(v)\, p_n^b(v)$ reflects the independence of two predictions for v_n derived from disjoint measurements sets $\{\boldsymbol{\mu}_1, \ldots, \boldsymbol{\mu}_{n-1}\}$ and $\{\boldsymbol{\mu}_{n+1}, \ldots, \boldsymbol{\mu}_N\}$.

An example smoother posterior PDF from the jet tank experiment is shown in Figure 5.1b. Compared to the product of measurement PDFs, the smoother has applied a correction of -0.2 cm s^{-1} to the velocity estimate by incorporating information from adjacent samples in time. Also, the width of the peak has decreased from 1.2 cm s^{-1} to 0.9 cm s^{-1}, reflecting an increase in measurement accuracy.

5.3.3 Automatic tuning

The noise standard deviation σ is a free parameter which controls the amount of smoothing applied by the estimator. The limit $\sigma \to \infty$ corresponds to maximum

likelihood estimation where no prior knowledge is used,

$$\hat{v} = \arg\max_{v} \prod_{i=1}^{N_f} p(\hat{\phi}_i, \hat{\rho}_i \,|\, v). \tag{5.17}$$

As σ decreases, the likelihood function is increasingly shaped by the assumption of temporal continuity. However, due to the random component ξ, the resulting velocity estimate is not constrained to obey the model precisely. The velocity estimate $\hat{v}$ is ultimately determined by available measurements, with the smoothing parameter affecting how measurements are temporally combined to form the MAP velocity estimate.

The measurement PDFs in (5.6) are determined by physical parameters of the sonar such as the carrier frequencies, pulse-to-pulse interval, and number of pulse-pairs per ensemble. For the jet tank experiment in Section 5.5, the smoothing parameter was automatically determined from the measurement time series via the following process.

1. Calculate velocity from multi-frequency phase measurements using (5.2) and evaluate the velocity spectrum;
2. Determine the lowest frequency f_N of the noise floor (e.g. see Figure 5.6 and the discussion in Section 5.5);
3. Choose a value for σ that is large compared to the velocity standard deviation;
4. Process measurements using the MAP velocity smoother with smoothing parameter σ;
5. Calculate the velocity spectrum for the time series produced by the smoother;

6. Decrease σ and iterate Steps 4 to 6 until the smoothed spectrum is linear in the interval $[0.5f_N, 2f_N]$.

In Step 6, the spectral slope is determined on a log-log plot, for example as shown in Figure 5.6. Once the tuning has been completed, the MAP velocity estimator is completely specified by sonar parameters and available measurements.

5.4 Instrumentation

5.4.1 Multi-frequency coherent Doppler sonar

Velocity measurements were collected using the multi-frequency coherent Doppler sonar described in Hay et al. (2008). The sonar employs a symmetric multistatic geometry as shown in Figure 5.2 with an angle of 14° between the centre transducer and transducers 1 and 2. Acoustic pulses are transmitted from the centre transducer and backscatter is received by all transducers. Each circular piezo-composite transducer has a diameter of 2 cm, a nominal centre frequency of 1.7 MHz, and a bandwidth of 1 MHz. Carrier frequencies, profiling range, range resolution, pulse length, pulse-to-pulse interval, and number of pulse-pairs per ensemble are configurable in software. Dimensions of each sample volume are determined by the beam pattern, carrier frequency, and range resolution. Nominally, each sample volume has a diameter of 2 cm and a height of 3 to 6 mm. Operating parameters for the sonar are listed in Table 5.1.

The sonar was installed in a rectangular jet tank with dimensions of 1.2 m on each side, as shown in Figure 5.3. A round jet emerged from a 1 cm inner diameter

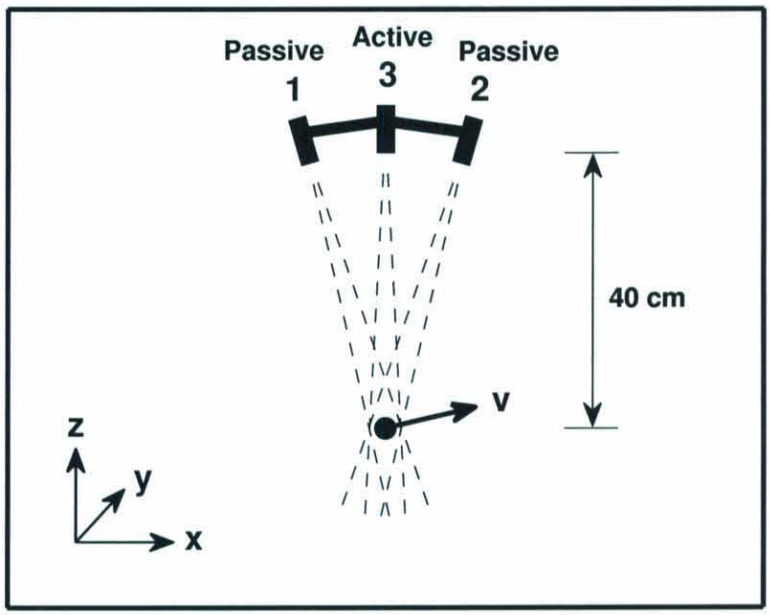

Figure 5.2: Schematic diagram of the symmetric multistatic sonar tested in the jet tank. Sound pulses are transmitted from transducer 3 and backscatter is received by all transducers. Beam patterns are indicated by dashed lines. The angle between the active transducer and transducers 1 and 2 is 14°.

Table 5.1: Coherent Doppler sonar parameters.

Parameter	**Value**
Transducer centre frequency	1.7 MHz
Transducer bandwidth	1.0 MHz
Transducer diameter	2 cm
Transmit pulse length	8 μs
Ping interval	0.88 ms
Pings per ensemble	10
Sample rate	113.6 Hz
Receiver bandwidth	125 kHz
Carrier frequencies	1.8, 2.0, 2.2, 2.4 MHz

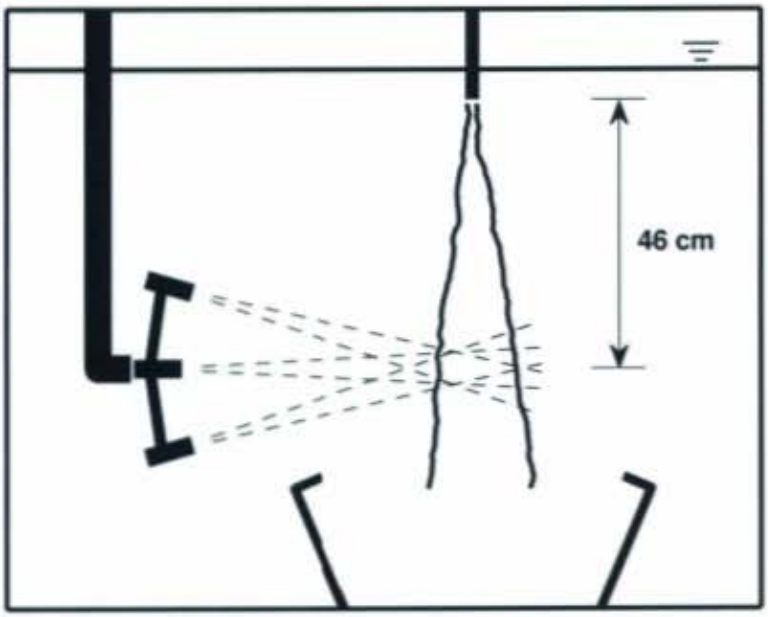

Figure 5.3: Side view schematic of the jet tank showing the multi-frequency coherent Doppler sonar. The jet flow was directed downward from the nozzle toward the capture cone. Sonar beam patterns intersected on the near side of the jet, as indicated with dashed lines.

nozzle that was directed downward just below the water surface. A capture cone at the bottom of the tank was connected to a recirculation pump. Steady flow rates were achieved by controlling the pump speed over a range of 600 to 3600 RPM.

Water in the tank was seeded with 50 μm diameter polyamide particles. The particles have a density of 1.03 g cm^{-3} and are thus approximately neutrally buoyant. Although the capture cone kept many of the particles in the recirculation circuit, particles tended to escape the cone and eventually settle on the tank bottom. Over the course of the experiment, seeding particles were added to maintain a concentration of approximately 1 g L^{-1} in the jet.

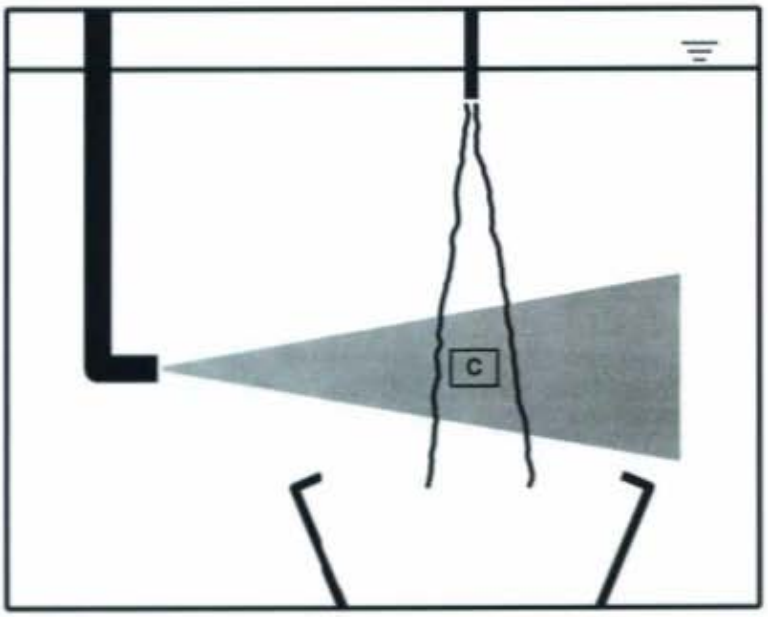

Figure 5.4: Side view schematic of the jet tank showing the laser periscope and light sheet. The intersection of the light sheet and camera field of view measured 5.3 cm by 4.0 cm, as indicated by the rectangle (C) located at the jet centre-line.

5.4.2 Particle image velocimetry

Particle illumination was provided by a dual-head Nd:YAG laser. The laser outputs two 120 mJ pulses at a wavelength of 532 nm with a pulse width of 5 ns and a repetition rate of up to 15 Hz. Laser light was directed toward the test area using an underwater periscope as shown in Figure 5.4. The width of the light sheet was approximately 5 mm.

The PIV data acquisition system consisted of a digital camera and a data acquisition computer containing a frame grabber board. Components of the data acquisition

system were obtained from Dantec Dynamics. Focus and aperture settings on the lens were adjusted manually for optimum exposure. Digital images at 1344×1024 pixel resolution were captured in a 5.3 cm by 4.0 cm rectangular region within the jet. Image pairs were recorded at 4 Hz using a timing signal to synchronize PIV and sonar data acquisition.

Velocity estimation was performed using the adaptive correlation method implemented in FlowManager software from Dantec Dynamics. The interrogation window size was set to 64×64 pixels with 50% overlap to ensure that each window contained a minimum of 5 particles (Raffel et al., 2007, chap. 5). Images were pre-processed to remove ambient illumination and to attenuate image noise. Outliers were detected and corrected using 3×3 local median validation. Additional information on PIV image processing and calibration is included in Appendix A.

Due to space constraints within the tank, the sonar and periscope were located as shown in the top view in Figure 5.5. The angle between the sonar and the light sheet was 18°. The camera was mounted outside the tank behind a glass wall. Intersection of the jet centre-line, light sheet, and sonar centre beam occurred in the centre of the camera field of view.

5.5 Experimental results

Horizontal velocity spectra from the jet tank are presented in Figure 5.6 for a jet discharge velocity of 118 cm s^{-1}. Spectra were calculated from 30 seconds of sonar measurements from the centre transducer range bin located on the jet centre-line. The spectrum for single frequency measurements is presented for the 2.2 MHz receiver

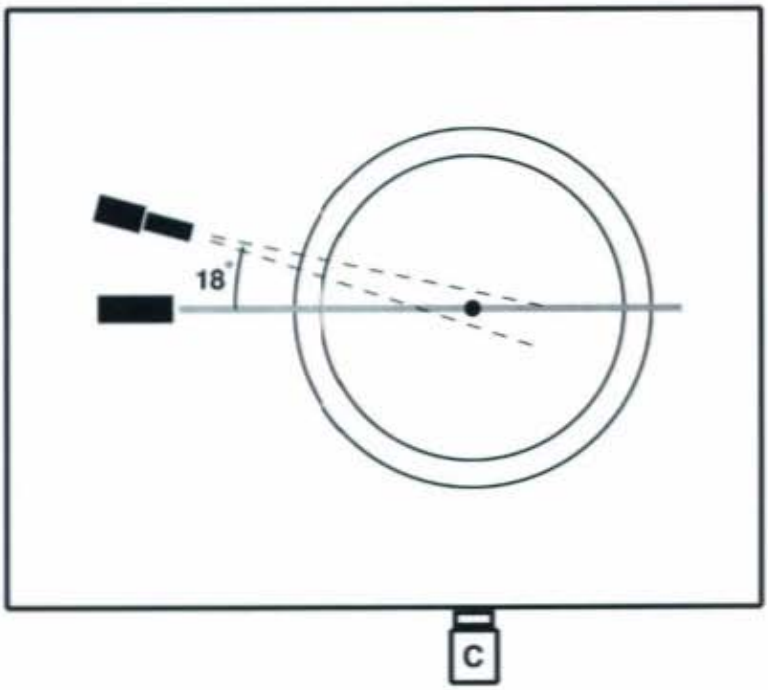

Figure 5.5: Top view schematic of the jet tank showing the multi-frequency coherent Doppler sonar and laser light sheet. The dot and concentric rings indicate the jet and the capture cone, respectively. The camera (C) was located outside the tank behind a glass wall.

channel only, as other channels show a similar result. The multi-frequency spectrum represents an average of measurements from each of the four carrier frequencies. For the maximum likelihood case, velocity was estimated from (5.17) where each measurement is weighted according to its measurement PDF. In other words, velocity was estimated from the location of the peak of the product PDF (e.g. as shown in Figure 5.1b).

Under-smoothed, auto-tuned, and over-smoothed results correspond to output from the MAP velocity smoother with σ equal to 3.2, 1.6, and 0.8 cm s^{-1}, respectively. The auto-tuned value of 1.6 cm s^{-1} was derived from the procedure outlined in

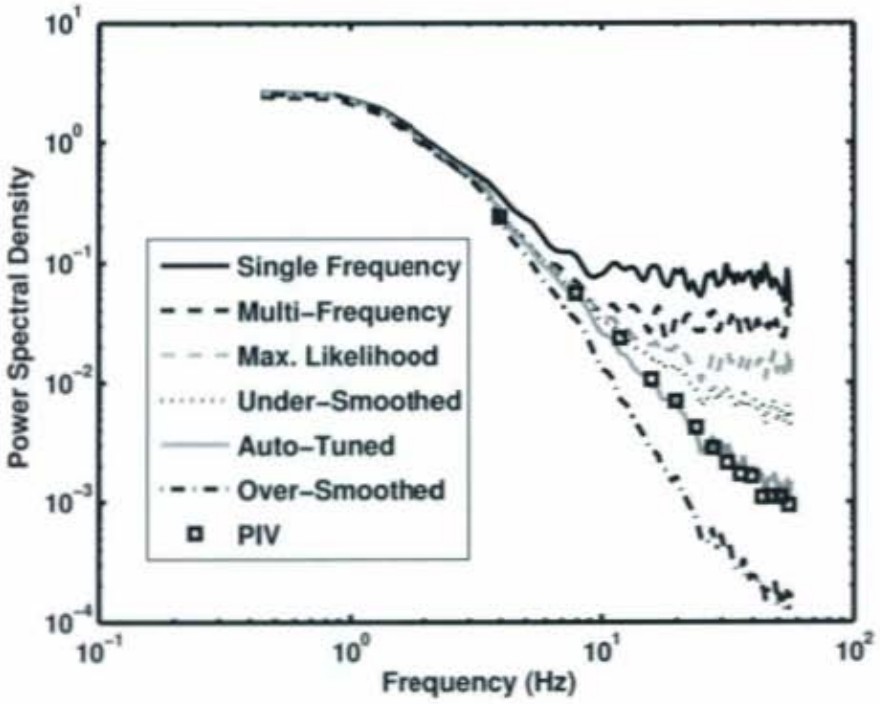

Figure 5.6: Horizontal velocity spectra for a turbulent round jet. Single frequency sonar measurements were derived from the 2.2 MHz receiver channel. The multi-frequency spectrum was produced by averaging measurements from all four carrier frequencies. The maximum likelihood estimate was derived from (5.17). Under-smoothed, auto-tuned, and over-smoothed results correspond to output from the MAP velocity smoother with σ equal to 3.2, 1.6, and 0.8 cm s^{-1}, respectively.

Section 5.3.3, where the noise floor of the multi-frequency spectrum was observed to begin at a frequency f_N of 10 Hz.

PIV velocity fields were recorded at 4 Hz, resulting in a total of 120 image pairs being recorded simultaneously with sonar measurements during the 30 second data acquisition interval. For the PIV results in Figure 5.6, horizontal velocity spectra were calculated in terms of spatial frequency for each image pair. Although the PIV system measures a different horizontal velocity component than the sonar, as indicated by the top view schematic in Figure 5.5, the results are expected to be statistically

similar due to the radial symmetry of the jet. Wavenumbers were multiplied by the mean downward velocity of 16.1 cm s^{-1} to transform spatial frequencies into temporal frequencies.

As expected, the noise floor in Figure 5.6 is highest for measurements made with a single carrier frequency. The spectrum for multi-frequency measurements demonstrates the noise reduction that is achievable when independent measurements are averaged. However, the noise floor was further reduced when measurements were weighted according to PDFs determined by the autocorrelation coefficients $\hat{\rho}$ for each measurement, as indicated by the maximum likelihood spectrum. Further noise reduction is possible when measurements are combined temporally rather than processing each sample independently. When MAP velocity smoothing was applied using the auto-tuned smoothing parameter, the smoothed, multi-frequency, and maximum likelihood (i.e. unsmoothed) spectra agree for frequencies less than 10 Hz. However, above 10 Hz, the MAP velocity estimator produces a power law velocity spectrum that agrees well with PIV measurements.

Horizontal velocity time series corresponding to the multi-frequency and auto-tuned smoother spectra are shown in Figure 5.7. Spikes in the multi-frequency time series would normally be removed with a despiking algorithm. However, lower amplitude measurement noise is difficult to separate from real turbulent fluctuations. The time series for the smoother follows the general trend of the multi-frequency measurements. The smoother suppresses measurement noise inherent in the raw measurements while retaining high frequency fluctuations that are characteristic of a turbulent flow.

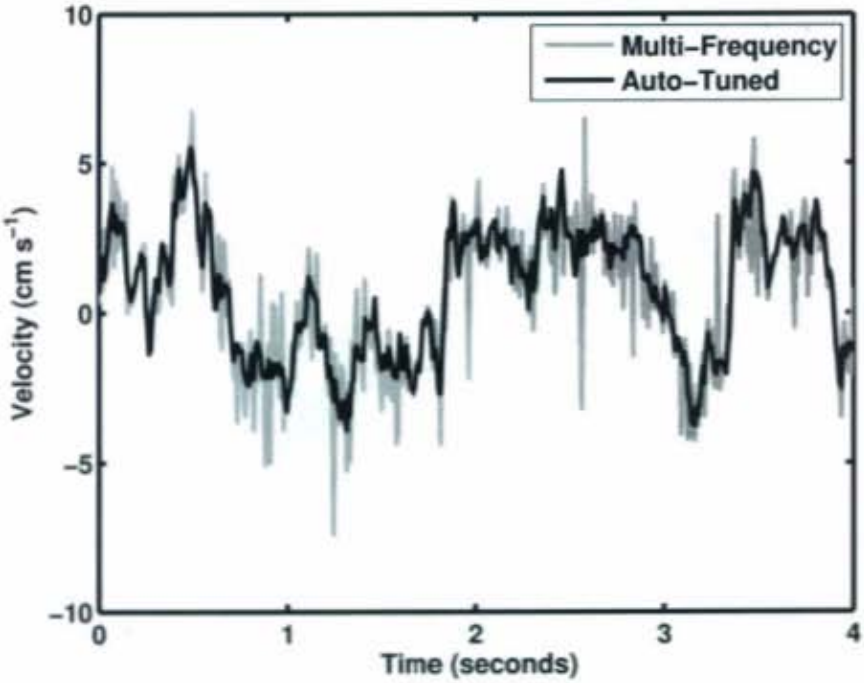

Figure 5.7: A representative four second interval of the horizontal velocity time series corresponding to multi-frequency and auto-tuned smoother spectra from Figure 5.6. The smoother attenuates measurement noise while retaining high frequency fluctuations characteristic of turbulent flow.

5.6 Conclusions

In this chapter, a velocity estimator for coherent Doppler sonar has been described. The estimator employs MAP estimation to optimally combine multi-frequency and multi-transducer measurements. The algorithm operates on a time series of measurements from a single point in space. Each phase measurement is weighted according to a PDF determined by a corresponding autocorrelation coefficient. A user-configurable smoothing parameter controls how measurements are combined in the time domain. A method was presented for automatically determining the smoothing parameter

from examination of the spectrum of a representative segment of the measurement time series. The method was evaluated using results from a laboratory turbulent jet where velocity was measured simultaneously with multi-frequency coherent Doppler sonar and particle image velocimetry. Automatic tuning of the estimator resulted in a velocity time series where measurement noise was suppressed while high frequency turbulence fluctuations were retained. Once a smoothing parameter has been chosen using the tuning procedure, the MAP velocity estimator is free from empirically determined thresholds or constants specific to a particular instrument or application.

Bibliography

Box, G. E. P. and Tiao, G. C. (1973). *Bayesian Inference in Statistical Analysis.* Addison-Wesley.

Dillon, J., Zedel, L., and Hay, A. E. (2011a). Asymptotic properties of an autocorrelation coefficient for coherent Doppler sonar. *Journal of Atmospheric and Oceanic Technology*, 28(7):966–973.

Dillon, J., Zedel, L., and Hay, A. E. (2011b). On the distribution of velocity measurements from pulse-to-pulse coherent Doppler sonar. *IEEE Journal of Oceanic Engineering, submitted.*

Garbini, J. L., Forster, F. K., and Jorgensen, J. E. (1982). Measurement of fluid turbulence based on pulsed ultrasound techniques. Part 1. Analysis. *Journal of Fluid Mechanics*, 118:445–470.

Gargett, A. E. (1989). Ocean turbulence. *Annual Review of Fluid Mechanics*, 21:419–451.

Hay, A. E. (2008). Near-bed turbulence and relict waveformed sand ripples: Observations from the inner shelf. *Journal of Geophysical Research*, 113(C04040), doi:10.1029/2006JC004013.

Hay, A. E., Zedel, L., Craig, R., and Paul, W. (2008). Multi-frequency, pulse-to-pulse coherent Doppler sonar profiler. In *Proceedings of the IEEE/OES 9th Working Conference on Current Measurement Technology*, pages 25–29.

Hurther, D. and Lemmin, U. (2001). A correction method for turbulence measurements with a 3D acoustic Doppler velocity profiler. *Journal of Atmospheric and Oceanic Technology*, 18(3):446–458.

Hurther, D. and Lemmin, U. (2008). Improved turbulence profiling with field-adapted acoustic Doppler velocimeters using a bifrequency Doppler noise suppression method. *Journal of Atmospheric and Oceanic Technology*, 25(3):452–463.

Kay, S. M. (1993). *Fundamentals of Statistical Signal Processing: Estimation Theory*, volume 1. Prentice-Hall PTR.

Lhermitte, R. (1983). Doppler sonar observation of tidal flow. *Journal of Geophysical Research*, 88(C1):725–742.

Lohrmann, A., Hackett, B., and Røed, L. P. (1990). High resolution measurements of turbulence, velocity and stress using a pulse-to-pulse coherent sonar. *Journal of Atmospheric and Oceanic Technology*, 7(1):19–37.

Plueddemann, A. J. (1992). Internal wave observations from the Arctic environmental drifting buoy. *Journal of Geophysical Research*, 97(C8):12619–12638.

Raffel, M., Willert, C. E., Wereley, S. T., and Kompenhans, J. (2007). *Particle Image Velocimetry: A Practical Guide*. Springer, second edition.

Rowe, F. D., Deines, K. L., and Gordon, R. L. (1986). High resolution current profiler. In *Proceedings of the IEEE 3rd Working Conference on Current Measurement*, volume 3, pages 184–189.

Smyth, C., Hay, A. E., and Zedel, L. (2002). Coherent Doppler profiler measurements of near-bed suspended sediment fluxes and the influence of bed forms. *Journal of Geophysical Research*, 107(C8), 3105, doi:10.1029/2000JC000760.

Thorne, P. D. and Hanes, D. M. (2002). A review of acoustic measurement of small-scale sediment processes. *Continental Shelf Research*, 22(4):603–632.

Veron, F. and Melville, W. K. (1999). Pulse-to-pulse coherent Doppler measurements of waves and turbulence. *Journal of Atmospheric and Oceanic Technology*, 16(11):1580–1597.

Zedel, L. (2008). Modeling pulse-to-pulse coherent Doppler sonar. *Journal of Atmospheric and Oceanic Technology*, 25(10):1834–1844.

Zedel, L., Hay, A. E., Cabrera, R., and Lohrmann, A. (1996). Performance of a single-beam pulse-to-pulse coherent Doppler profiler. *IEEE Journal of Oceanic Engineering*, 21(3):290–297.

Zrnić, D. S. (1977). Spectral moment estimates from correlated pulse pairs. *IEEE Transactions on Aerospace and Electronic Systems*, AES-13(4):344–354.

Chapter 6 Preamble

This chapter presents results from a towing tank experiment that used a rectangular grid to generate turbulence upstream of the sonar. In this chapter, two additional thesis objectives are achieved: (i) the MAP velocity estimator performs velocity ambiguity resolution and measurement noise suppression simultaneously, and (ii) the one-dimensional estimator from Chapter 5 is generalized to higher dimensions to combine measurements from multiple transducers.

This chapter presents a paper titled "Simultaneous Velocity Ambiguity Resolution and Noise Suppression for Multi-Frequency Coherent Doppler Sonar." It has been submitted to the *Journal of Atmospheric and Oceanic Technology* (Dillon et al., 2011d).

Chapter 6

Velocity Ambiguity Resolution

6.1 Abstract

Coherent Doppler sonar is a useful tool for non-invasive measurement of ocean currents, sediment transport, and turbulence in coastal environments. Various methods have been proposed to separately address two of its inherent limitations: velocity ambiguity and measurement noise. However, in energetic turbulent flows, both factors may be present simultaneously. The presence of measurement noise complicates velocity ambiguity resolution, and vice versa, velocity ambiguity presents a challenge for existing noise suppression methods. A velocity estimator based on Maximum A Posteriori (MAP) estimation has been developed to resolve velocity ambiguity and suppress measurement noise simultaneously rather than separately. The estimator optimally combines measurements from multiple acoustic carrier frequencies and multiple transducers. Data fusion is achieved using a probabilistic approach, whereby measurements are combined numerically to derive a velocity likelihood function. The

MAP velocity estimator is evaluated using a high fidelity coherent Doppler sonar simulation of oscillating flow, and with data from a towing tank grid turbulence experiment where both velocity ambiguity and backscatter decorrelation were present. Time series and spectra from MAP velocity estimation are compared to those obtained with conventional Doppler signal processing. In addition to robustly resolving velocity ambiguity, the MAP velocity estimator is shown to reduce high frequency noise in turbulence spectra.

6.2 Introduction

Pulse-to-pulse coherent Doppler sonar has been widely used to investigate oceanic transport and mixing processes. Applications include measurement of tidal flows (Lhermitte, 1983), surface wave breaking (Veron and Melville, 1999), internal waves (Plueddemann, 1992), sediment transport (Smyth et al., 2002), and near-bed turbulence (Hay, 2008).

Backscatter autocorrelation is the fundamental measurement in coherent Doppler sonar. For a sequence $\{z_n\}$ of backscatter samples, the autocorrelation at a lag of one pulse-to-pulse interval is

$$R(\tau) = E(z_n^* z_{n+1}) \tag{6.1}$$

where E denotes expected value, * denotes complex conjugation, and τ is the time interval between successive acoustic transmissions. The radial velocity component is

proportional to the pulse-to-pulse phase shift $\phi = \angle R(\tau)$ (Lohrmann et al., 1990),

$$v = \frac{c}{4\pi f_0 \tau}\phi; \quad \phi \in [-\pi, \pi] \tag{6.2}$$

where c is the speed of acoustic wave propagation and f_0 is the carrier frequency of the transmitted signal. In (6.2), the phase interval $[-\pi, \pi]$ corresponds to an ambiguity velocity

$$v_a = \frac{c}{4f_0\tau}. \tag{6.3}$$

In other words, scatterer velocities of v_a and $-v_a$ are indistinguishable since phase shifts of π and $-\pi$ are equivalent.

In practice, autocorrelation is estimated from a finite sequence of M pulse-pairs (Zrnić, 1977),

$$\hat{R}(\tau) = \frac{1}{M}\sum_{n=1}^{M} z_n^* z_{n+1}. \tag{6.4}$$

The phase $\hat{\phi}$ of the autocorrelation estimate is determined from real and imaginary components of $\hat{R}(\tau)$. Corresponding to each phase measurement, the autocorrelation magnitude $\hat{\rho}$ may also be defined (Zedel et al., 1996),

$$\hat{\rho} = \frac{\left|\sum_{n=1}^{M} z_n^* z_{n+1}\right|}{\sum_{n=1}^{M} |z_n^* z_{n+1}|}. \tag{6.5}$$

The coefficient $\hat{\rho}$ provides a measure of data quality and satisfies $0 \leq \hat{\rho} \leq 1$.

Measurement noise is caused by pulse-to-pulse backscatter decorrelation from (i) scatterer advection through the sample volume, (ii) velocity shear and turbulence within the sample volume, (iii) phase distortion of the transmitted wave, and (iv)

electronic noise in the receiver circuitry (Zedel et al., 1996; Hurther and Lemmin, 2001). Noise suppression is possible when redundant measurements with uncorrelated measurement errors are available. An example of this approach is the use of two non-overlapping sample domains (Garbini et al., 1982). Redundant measurements with uncorrelated errors may also be obtained using additional acoustic receivers (Rowe et al., 1986; Hurther and Lemmin, 2001) or by simultaneously transmitting two or more acoustic carrier frequencies (Hurther and Lemmin, 2008; Hay et al., 2008).

Coherent Doppler sonar measurements are also limited by the existence of velocity ambiguity. Velocity ambiguity may be resolved by cross-correlating broadband pulses (Brumley et al., 1991) or by invoking the assumption that the velocity field is continuous in time and space, e.g. by adding multiples of 2π to the autocorrelation phase to minimize discontinuities in time (Smyth and Hay, 2003), space (Ray and Ziegler, 1977), or both simultaneously (Franca and Lemmin, 2006). Another method for velocity ambiguity resolution involves varying the pulse-to-pulse interval τ to obtain two or more staggered pulse repetition frequencies (Lhermitte and Serafin, 1984; Lohrmann et al., 1990). Multi-frequency coherent Doppler sonar is a recent development where multiple acoustic carrier frequencies are transmitted simultaneously using a wide bandwidth acoustic transducer (Nitzpon et al., 1995; Hay et al., 2008). The use of multiple frequencies gives rise to different ambiguity velocities from which the true velocity can be determined (Zedel and Hay, 2010).

In order to resolve velocity ambiguity and suppress measurement noise *simultaneously*, a velocity estimator has been developed based on the Bayesian technique of Maximum A Posteriori (MAP) estimation (Kay, 1993). The MAP velocity estimator shares many similarities with a Kalman smoother: (i) the estimator processes a time

series recursively, (ii) a model is used to provide prior statistical knowledge, (iii) the estimator produces its own performance measure, and (iv) estimator lag is eliminated via application both forward and backward in time. However, unlike a Kalman smoother, the MAP velocity estimator makes use of non-Gaussian probability density functions and is inherently nonlinear. The motivation for using MAP estimation is that velocity ambiguity causes the velocity likelihood function to be multi-modal; thus a Gaussian representation is inappropriate.

The MAP velocity estimator optimally combines measurements from multiple acoustic carrier frequencies and multiple transducers. Data fusion is achieved using a probabilistic approach, whereby measurements are combined numerically to derive a velocity likelihood function. While the focus of this chapter is on multistatic multi-frequency coherent Doppler sonar, the results are equally applicable to single-frequency and staggered pulse repetition frequency systems with monostatic or multistatic geometries. Results are presented for a towing tank grid turbulence experiment where both velocity ambiguity and backscatter decorrelation were present. Time series and spectra from MAP velocity estimation are compared to those obtained with conventional Doppler signal processing. In addition to robustly resolving velocity ambiguity, the MAP velocity estimator is shown to reduce high frequency noise in turbulence spectra.

6.3 Theory

6.3.1 MAP estimation

Maximum A Posteriori (MAP) estimation is one of several parameter estimation methods based on Bayesian inference. In contrast with classical statistical estimation, Bayesian methods treat a parameter to be estimated as a random variable rather than a deterministic but unknown constant (Box and Tiao, 1973). The motivation for the Bayesian approach is that prior knowledge of the probability density function (PDF) may be used to improve estimator performance. Once observations have been made, Bayes' theorem permits calculation of the posterior PDF which expresses the likelihood of a particular parameter value given the measurements that have been observed. An estimate is then calculated as a function of the posterior PDF, for example as the location of the maximum value in MAP estimation (Kay, 1993).

The unknown parameter to be estimated is the radial speed v (for monostatic sonar) or the velocity vector $\mathbf{v}$ (for multistatic sonar). Let $\boldsymbol{\mu}$ denote a vector of measurements consisting of autocorrelation phase and autocorrelation magnitude for each carrier frequency and transducer. The MAP velocity estimate is the location of the maximum value of the posterior velocity PDF, denoted by (Kay, 1993, chap. 11)

$$\hat{\mathbf{v}} = \arg \max_{\mathbf{v}} p(\mathbf{v})\, p(\boldsymbol{\mu} \,|\, \mathbf{v}). \tag{6.6}$$

The term $p(\mathbf{v})$ describes any prior knowledge of $\mathbf{v}$ that exists before measurements have been observed. The measurement PDF $p(\boldsymbol{\mu} \,|\, \mathbf{v})$ expresses the probability of

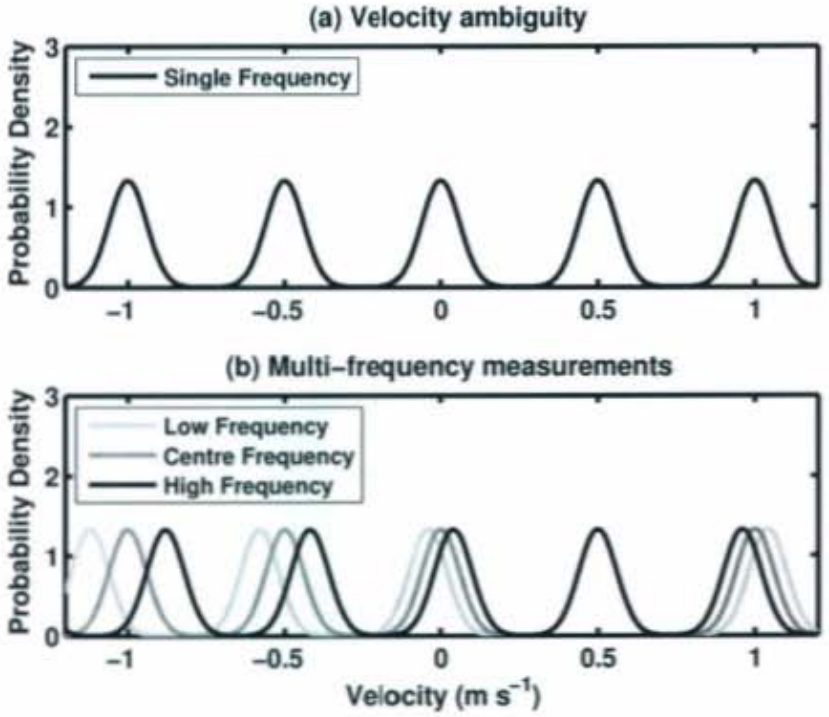

Figure 6.1: Velocity likelihood functions for single- and multi-frequency phase measurements. The true velocity 0.5 m s^{-1} has been measured using: (a) a single carrier frequency with an ambiguity velocity of 0.25 m s^{-1}, and (b) multiple carrier frequencies with ambiguity velocities of 0.23, 0.25, and 0.27 m s^{-1}.

observing measurements $\boldsymbol{\mu}$ when velocity takes the value $\mathbf{v}$.

Since autocorrelation phase can only be measured modulo 2π radians, the velocity likelihood function for a single phase measurement is periodic with period $2v_a$ determined by the ambiguity velocity. For example, a measurement with $\tilde{\phi} = 0$ and $v_a = 0.25$ m s^{-1} is illustrated in Figure 6.1a. From only a single measurement, it is not possible to determine the true velocity unless prior knowledge can be invoked to restrict the range of possible velocity values.

In a multi-frequency system, velocity ambiguity may be resolved by noting that ambiguity velocity is inversely proportional to each carrier frequency (Zedel and Hay,

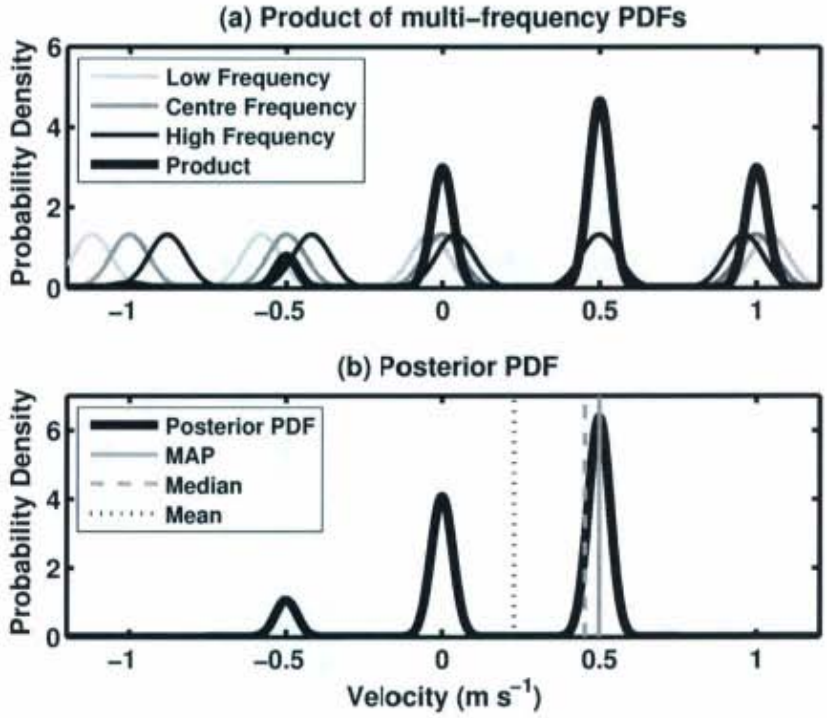

Figure 6.2: Velocity likelihood functions showing: (a) the product of PDFs from multiple carrier frequencies, and (b) the posterior mean, median, and MAP estimate. In (b), prior knowledge has been represented by restricting velocity to lie in the interval $|v| < 0.75$ m s^{-1}.

2010). For example, velocity likelihood functions are shown in Figure 6.1b for a true velocity of 0.5 m s^{-1} and carrier frequencies with ambiguity velocities of 0.23, 0.25, and 0.27 m s^{-1}. In this example, all three likelihood functions coincide in the vicinity of the true velocity. Although each function is periodic, periods differ according to the distinct ambiguity velocities.

Independent measurements in Figure 6.1b may be combined by multiplying the corresponding probability distributions, as shown in Figure 6.2a. No measurement errors have been introduced; the existence of multiple peaks in Figure 6.2a is solely the result of measurement uncertainty and the presence of velocity ambiguity.

Prior knowledge may be used to further constrain the velocity likelihood function. In the example posterior PDF shown in Figure 6.2b, prior knowledge has been represented by enforcing the restriction $|v| < 0.75$ m s^{-1}. In Figure 6.2b, the mean and median values for the posterior PDF are biased by the presence of multiple peaks. These two methods are therefore not suitable when the posterior PDF is multi-modal. In contrast, the MAP estimator correctly selects the most likely peak.

6.3.2 Bistatic Doppler shift

A bistatic geometry is depicted in Figure 6.3, where the scatterer, transmitter, and receiver positions are indicated by S, T, and R, respectively. Unit vectors directed from the scatterer to the transmitter and receiver are denoted by $\mathbf{r}_T$ and $\mathbf{r}_R$. The transmitter-receiver pair measures a velocity component in the direction of the bistatic baseline, i.e. toward the line segment RT and along the bisector of the angle $\angle RST$. Let $\mathbf{r}_B$ denote a unit vector directed toward the baseline in the direction $\mathbf{r}_T + \mathbf{r}_R$ as shown in Figure 6.3. The angle subtended by vectors $\mathbf{r}_T$ and $\mathbf{r}_R$ is denoted by 2θ.

If a sinusoidal acoustic source of frequency f_0 emanates from the transmitter, the observed frequency f_R at the receiver is given by

$$f_R = f_0 \left(\frac{c + \mathbf{v} \cdot \mathbf{r}_T}{c - \mathbf{v} \cdot \mathbf{r}_R} \right). \tag{6.7}$$

Since $|v| \ll c$ for oceanographic applications, (6.7) may be approximated with a first order Taylor series to obtain

$$f_R = f_0 \left(1 + \frac{\mathbf{v} \cdot \mathbf{r}_T + \mathbf{v} \cdot \mathbf{r}_R}{c} \right). \tag{6.8}$$

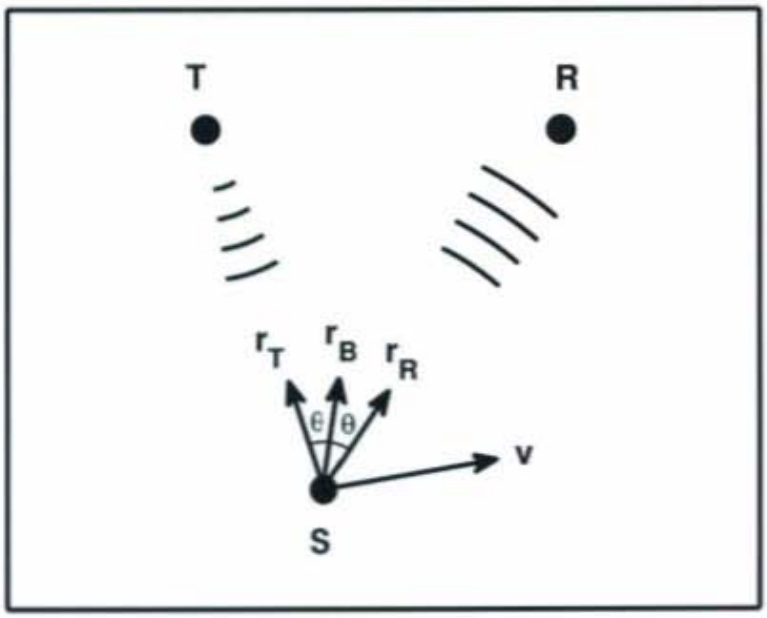

Figure 6.3: Schematic diagram of a scatterer S, transmitter T, and receiver R. The scatterer is moving with velocity vector $\mathbf{v}$. Unit vectors $\mathbf{r}_T$, $\mathbf{r}_R$, and $\mathbf{r}_B$ are directed from the scatterer to the transmitter, to the receiver, and toward the bistatic baseline RT, respectively. The angle between $\mathbf{r}_T$ and $\mathbf{r}_R$ is 2θ.

Since $\mathbf{r}_T + \mathbf{r}_R = 2\,\mathbf{r}_B \cos\theta$, the Doppler frequency shift $f_D = f_R - f_0$ is

$$f_D = f_0 \left(\frac{2\,\mathbf{v} \cdot \mathbf{r}_B \cos\theta}{c} \right). \tag{6.9}$$

Thus, a bistatic configuration measures the velocity component $v_B = \mathbf{v} \cdot \mathbf{r}_B$ toward the bistatic baseline. When the covariance method is used to estimate Doppler frequency, autocorrelation phase and the velocity component v_B are related by

$$\phi = 4\pi f_0 \tau \frac{v_B}{c} \cos\theta. \tag{6.10}$$

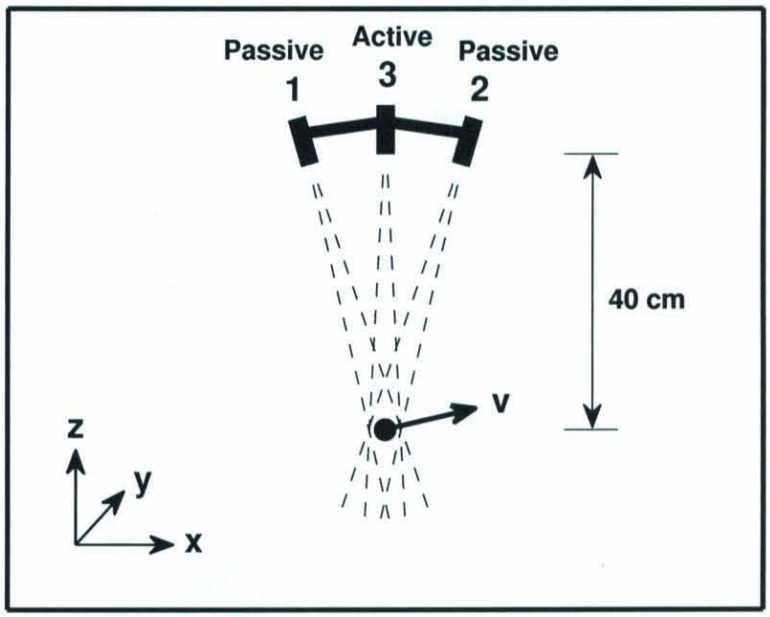

Figure 6.4: Schematic diagram of the symmetric multistatic sonar tested in the towing tank. Sound pulses are transmitted from transducer 3 and backscatter is received by all transducers. Beam patterns are indicated by dashed lines. The angle between the centre transducer and transducers 1 and 2 is 14°. Bistatic baselines are tilted 7° from the x-axis.

6.3.3 Velocity estimation

A symmetric two-dimensional multistatic sonar geometry is illustrated in Figure 6.4. Acoustic pulses are transmitted from transducer 3 and backscatter is received by all three transducers. Velocity measurement occurs in the region where transducer beam patterns overlap, as indicated with dashed lines in Figure 6.4, producing a velocity profile that extends above and below the nominal intersection point by approximately 10 cm (Hay et al., 2008).

Let γ denote the tilt angle of the transducer 1 and 2 baselines with respect to the x-axis in Figure 6.4. For the isosceles geometry in Figure 6.4, $\theta = \gamma$ for a scatterer at the beam intersection point. Velocity components measured by each receiver are denoted by v_j $(j = 1, 2, 3)$ with unit vectors $\mathbf{r}_j$ directed from the beam intersection point toward the corresponding baselines for $j = 1, 2$ and toward the centre transducer for $j = 3$. If the velocity vector is specified in Cartesian coordinates as $[v_x\ v_z]$, velocity measurements are given by

$$v_1 = -v_x \sin\gamma + v_z \cos\gamma \tag{6.11}$$

$$v_2 = v_x \sin\gamma + v_z \cos\gamma \tag{6.12}$$

$$v_3 = v_z. \tag{6.13}$$

For comparison with MAP estimation, a least squares inverse transformation will be used to determine Cartesian velocity components from transducer measurements,

$$v_x = \frac{v_2 - v_1}{2\sin\gamma} \tag{6.14}$$

$$v_z = \frac{v_3 + (v_1 + v_2)\cos\gamma}{1 + 2\cos^2\gamma}. \tag{6.15}$$

Division by $\sin\gamma$ in (6.14) indicates that the transverse velocity component v_x is more difficult to estimate than the radial component v_z. For a tilt angle γ of 7°, the measurement error ratio σ_x/σ_z is approximately equal to 10.

In the least squares formulation for v_x and v_z, each measurement is weighted equally. In contrast, the MAP velocity estimator uses (6.11)–(6.13) to project measurement PDFs onto a two-dimensional velocity space, thereby weighting each mea-

surement according to its PDF.

For a multi-frequency system with N_f carrier frequencies and N_t transducers, measurements consist of autocorrelation phase $\hat{\phi}_{ij}$ and autocorrelation magnitude $\hat{\rho}_{ij}$ corresponding to each carrier frequency f_i and transducer j. The MAP velocity estimator takes the form

$$\hat{\mathbf{v}} = \arg\max_{\mathbf{v}} p(\mathbf{v}) \prod_{i=1}^{N_f} \prod_{j=1}^{N_t} p(\hat{\phi}_{ij}, \hat{\rho}_{ij} \,|\, v_j). \tag{6.16}$$

For the results presented in this chapter, measurement PDFs were determined from simulations of a Gaussian random process as described in Chapter 4 (Dillon et al., 2011c), with a correction for the bias of the autocorrelation coefficient from Chapter 3 (Dillon et al., 2011a).

6.3.4 Filtering and smoothing

The following presentation extends the one-dimensional MAP velocity estimator described in Chapter 5 (Dillon et al., 2011b) to higher dimensions. Superscripts f, b, and s denote results from the forward filter, backward filter, and smoother, respectively. Let $\overline{p}_n^f(\mathbf{v})$ denote the forward time posterior PDF, i.e. $p(\mathbf{v}_n \,|\, \boldsymbol{\mu}_1, \ldots, \boldsymbol{\mu}_n)$, describing the likelihood of $\mathbf{v}_n$ occurring after the sequence of measurements $\{\boldsymbol{\mu}_1, \ldots, \boldsymbol{\mu}_n\}$. The sample-to-sample velocity increment is assumed to obey a Gaussian probability distribution. Therefore, given a posterior PDF $\overline{p}_n^f(\mathbf{v})$, the predicted likelihood $p_{n+1}^f(\mathbf{v})$ is the convolution of $\overline{p}_n^f(\mathbf{v})$ with a Gaussian distribution (Rosenthal, 2000),

$$p_{n+1}^f(\mathbf{v}) = \frac{1}{(2\pi)^{\frac{d}{2}} \det^{\frac{1}{2}} \mathbf{C}_\xi} \int_{\mathbb{R}^d} \overline{p}_n^f(\mathbf{v} - \mathbf{u})\, e^{-\frac{1}{2}\mathbf{u}^T \mathbf{C}_\xi^{-1} \mathbf{u}} d\mathbf{u}, \tag{6.17}$$

where d is the dimension of the velocity vector and $\mathbf{C}_\xi$ denotes the covariance matrix of the velocity increment.

The forward time MAP velocity estimator is obtained by maximizing the posterior PDF as in (6.16),

$$\overrightarrow{p}_n^f(\mathbf{v}) = p_n^f(\mathbf{v}) \prod_{i=1}^{N_f} \prod_{j=1}^{N_t} p(\tilde{\phi}_{n_{ij}}, \tilde{\rho}_{n_{ij}} \,|\, v_j) \tag{6.18}$$

$$\hat{\mathbf{v}}_n = \arg\max_{\mathbf{v}} \overrightarrow{p}_n^f(\mathbf{v}). \tag{6.19}$$

The forward time prior distribution $p_1^f(\mathbf{v})$ is initialized to be uniform and is updated using the convolution operation in (6.17).

Let $\overrightarrow{p}_n^b(\mathbf{v})$ denote the backward time posterior PDF, i.e. $p(\mathbf{v}_n \,|\, \boldsymbol{\mu}_n, \ldots, \boldsymbol{\mu}_N)$, describing the likelihood of $\mathbf{v}_n$ occurring after observation of the measurement sequence $\{\boldsymbol{\mu}_N, \boldsymbol{\mu}_{N-1}, \ldots, \boldsymbol{\mu}_n\}$. Analogous to the forward time case, the backward time estimator is given by

$$\overrightarrow{p}_n^b(\mathbf{v}) = p_n^b(\mathbf{v}) \prod_{i=1}^{N_f} \prod_{j=1}^{N_t} p(\tilde{\phi}_{n_{ij}}, \tilde{\rho}_{n_{ij}} \,|\, v_j) \tag{6.20}$$

$$\hat{\mathbf{v}}_n = \arg\max_{\mathbf{v}} \overrightarrow{p}_n^b(\mathbf{v}). \tag{6.21}$$

The backward time prior distribution $p_N^b(\mathbf{v})$ is initialized to be uniform and is updated as in (6.17),

$$p_{n-1}^b(\mathbf{v}) = \frac{1}{(2\pi)^{\frac{d}{2}} \det^{\frac{1}{2}} \mathbf{C}_\xi} \int_{\mathbb{R}^d} \overrightarrow{p}_n^b(\mathbf{v} - \mathbf{u})\, e^{-\frac{1}{2}\mathbf{u}^T \mathbf{C}_\xi^{-1} \mathbf{u}} d\mathbf{u}. \tag{6.22}$$

The terms $p_n^f(\mathbf{v})$ and $p_n^b(\mathbf{v})$ in (6.18) and (6.20) describe prior information gained

from measurements $\{\boldsymbol{\mu}_1, \ldots, \boldsymbol{\mu}_{n-1}\}$ and $\{\boldsymbol{\mu}_{n+1}, \ldots, \boldsymbol{\mu}_N\}$, respectively.

MAP estimation can also be implemented by combining all measurements in the form of a smoother. Let $\overline{p}_n^s(\mathbf{v})$ denote the smoother posterior PDF $p(\mathbf{v}_n \,|\, \boldsymbol{\mu}_1, \ldots, \boldsymbol{\mu}_N)$ describing the likelihood of $\mathbf{v}_n$ occurring after all measurements in the time series have been recorded. The MAP smoother is formed by combining the results from forward and backward filtering,

$$\overline{p}_n^s(\mathbf{v}) = p_n^f(\mathbf{v})\, p_n^b(\mathbf{v}) \prod_{i=1}^{N_f} \prod_{j=1}^{N_t} p(\hat{\phi}_{n_{ij}}, \hat{\rho}_{n_{ij}} \,|\, v_j) \tag{6.23}$$

$$\hat{\mathbf{v}}_n = \arg \max_{\mathbf{v}} \overline{p}_n^s(\mathbf{v}). \tag{6.24}$$

With this formulation, the smoother utilizes all available measurements to estimate $\mathbf{v}_n$. The product $p_n^f(\mathbf{v})\, p_n^b(\mathbf{v})$ reflects the independence of two predictions for $\mathbf{v}_n$ derived from disjoint measurements sets $\{\boldsymbol{\mu}_1, \ldots, \boldsymbol{\mu}_{n-1}\}$ and $\{\boldsymbol{\mu}_{n+1}, \ldots, \boldsymbol{\mu}_N\}$.

6.4 Numerical simulation

In order to evaluate MAP estimation of a known velocity, simulations of oscillating flow were performed using the coherent Doppler sonar model described in Zedel (2008). The model simulates pulse-to-pulse coherent scattering from a cloud of moving particles for arbitrary multistatic sonar geometries. Physical effects such as spherical spreading, acoustic absorption, frequency-dependent beam patterns, transducer frequency response, and receiver noise are included in the model. The model supports simulation of arbitrary pulse shapes, including the use of multiple carrier frequencies.

Oscillating horizontal flow was simulated with a sinusoidal amplitude of 4.0 m s^{-1} and a period of 10 seconds. Thirty seconds of simulated measurements were generated, representing three periods of oscillation. In the model, the multistatic configuration shown in Figure 6.4 was tilted 5° from vertical to reproduce the geometry of the grid turbulence experiment described in Section 6.5. Parameters for the coherent Doppler sonar simulation are listed in Table 6.1.

Table 6.1: Coherent Doppler sonar simulation parameters.

Parameter	**Value**
Transducer centre frequency	1.7 MHz
Transducer bandwidth	1.0 MHz
Transducer diameter	2 cm
Transmit pulse length	4 μs
Baseline tilt angle γ	7°
Ping interval τ	1.5 ms
Pulse-pairs per ensemble	10
Sample rate	66.7 Hz
Receiver bandwidth	250 kHz
Carrier frequencies	1.2, 1.5, 1.8, 2.1 MHz
Simulation time step	12.5 ns
Simulation time	30 s
Particle number density	4720 L^{-1}
Receiver signal-to-noise ratio	10 dB

In Figure 6.5a, the phase time series is presented for the 2.1 MHz receiver channel of the centre transducer in the oscillating flow simulation. Numerous phase discontinuities at $\pm\pi$ are present. Similar results were obtained for carrier frequencies at 1.2, 1.5, and 1.8 MHz, except that phase discontinuities occurred at higher speed for lower carrier frequencies. When velocity is near zero, for example at $t = 5$ and 10 seconds, phase measurement noise is minimal. However, when the velocity amplitude is high, for example at $t = 2.5$ and 7.5 seconds, phase measurement noise increases

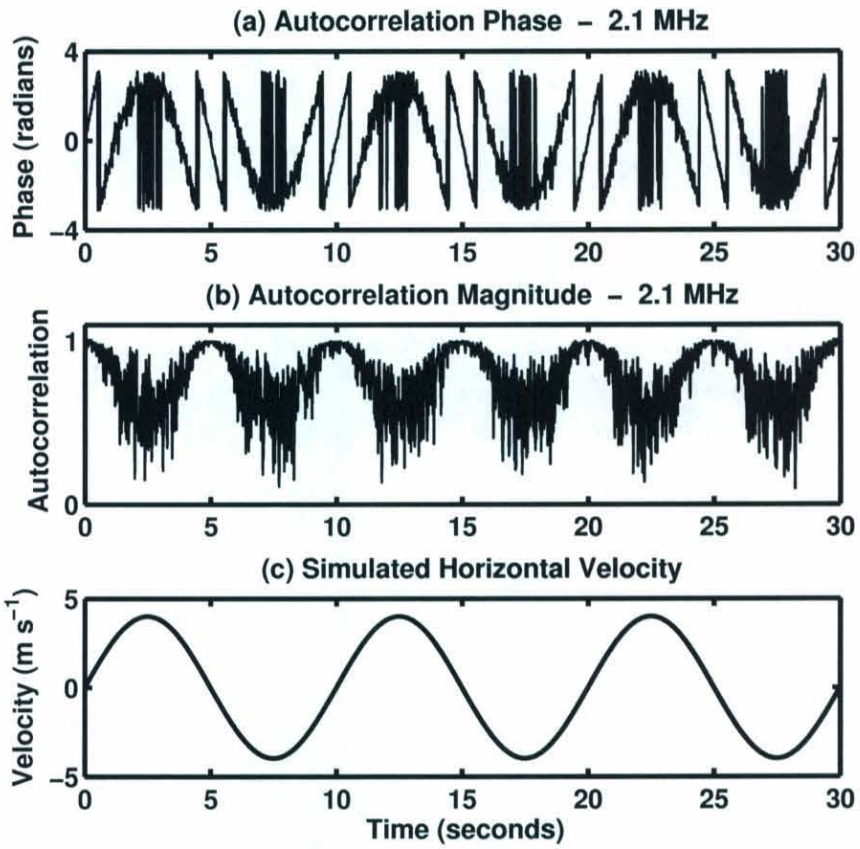

Figure 6.5: Simulated time series showing: (a) autocorrelation phase and (b) autocorrelation magnitude from the centre transducer 2.1 MHz receiver channel. The oscillating horizontal velocity is shown in (c).

due to backscatter decorrelation caused by scatterer advection through the sample volume. The oscillating flow simulation therefore provides a data set in which both velocity ambiguity and significant measurement noise are present.

The time series of autocorrelation magnitude is presented in Figure 6.5b for the 2.1 MHz receiver channel of the centre transducer in the oscillating flow simulation. Autocorrelation magnitude also exhibits periodic behaviour corresponding to the phase noise in Figure 6.5a. When velocity is near zero, autocorrelation magnitude

for all frequency channels approaches one. When the velocity amplitude is high, autocorrelation coefficients as low as 0.1 are observed. However, during periods of peak velocity, a wide range of coefficients are observed. Thus, accurate velocity estimates may be obtained if samples are combined in a way that emphasizes the higher quality measurements.

6.4.1 Radial velocity

The MAP velocity estimator was configured to calculate velocity likelihood functions on a one-dimensional grid extending over ± 1 m s^{-1} in increments of 0.01 m s^{-1}. Gaussian interpolation was used to refine the location of the likelihood peak (Appendix B). Velocity smoothing was performed as described in Section 6.3 with $\mathbf{C}_\xi = \sigma^2$ in (6.17) and (6.22) and σ equal to 0.01 m s^{-1}. The smoothing parameter σ is a user-configurable parameter that describes the expected amplitude of velocity increments from sample to sample. The value of σ was chosen to be less than the radial ambiguity velocity and greater than the maximum sinusoidal velocity increment in one ensemble interval $M\tau$. For the oscillating flow simulation, radial velocity varies as

$$v(t) = V \sin\left(\frac{2\pi t}{T_o}\right) \sin 5^\circ \tag{6.25}$$

where V is the peak horizontal velocity and T_o is the period of oscillation. Therefore, the maximum velocity increment is given by

$$\left.\frac{dv}{dt}\right|_{t=0} \Delta t = \frac{2\pi V \sin 5^\circ}{T_o} M\tau \tag{6.26}$$

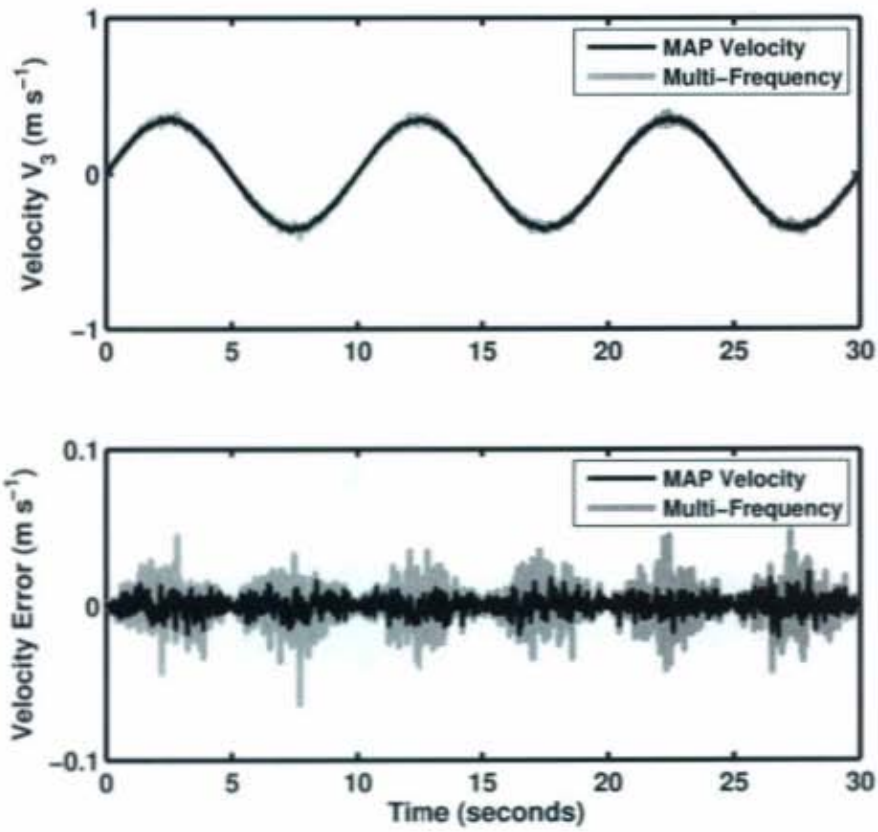

Figure 6.6: Comparison of MAP radial velocity estimation and averaged multi-frequency measurements. Velocity ambiguity has been removed from the multi-frequency (gray) curve by adding multiples of 2π to autocorrelation phase to minimize velocity error.

which is equal to 0.003 m s^{-1} for the parameters of the oscillating flow simulation.

In Figure 6.6, radial velocity from MAP velocity estimation is compared with the average of multi-frequency measurements from the centre transducer. Velocity ambiguity has been removed from the multi-frequency curve in Figure 6.6a by adding multiples of 2π to each phase measurement to minimize the difference between the measured and actual radial velocities. The MAP estimator, however, operates on raw

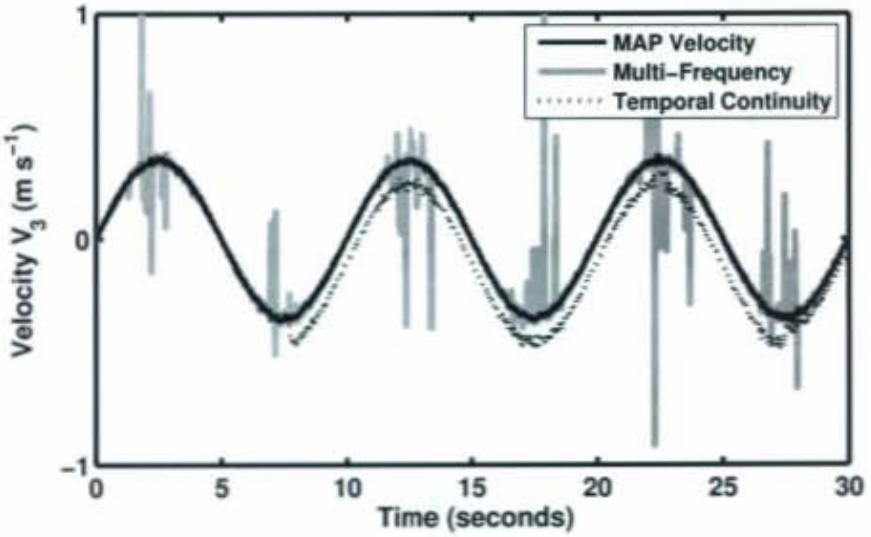

Figure 6.7: Comparison of radial velocity ambiguity resolution using MAP estimation, multi-frequency phase resolution, and temporal continuity.

phase measurements constrained to the interval $[-\pi, \pi]$.

The time series of velocity error in Figure 6.6b shows that measurement error for the multi-frequency measurements increases when the velocity amplitude is high. In addition to resolving velocity ambiguity, the MAP velocity estimator produces an error time series with a standard deviation of 0.005 m s^{-1} compared to 0.011 m s^{-1} for the average of multi-frequency measurements. Also, the multi-frequency error time series in Figure 6.6b is clearly periodic. Although the quality of raw measurements varies in time, reduced RMS error is possible using the MAP velocity estimator since each measurement is weighted according to its probability density function.

In practice, velocity ambiguity cannot be removed from individual measurements as in Figure 6.6a since the actual velocity would not be known. In Figure 6.7, radial velocity from the MAP velocity estimator is compared with two other methods

for velocity ambiguity resolution. All three algorithms operate on the same set of raw measurements. The multi-frequency phase resolution algorithm processes measurements from each sample in time to derive a linear relationship between phase and frequency based on an estimate of the slope $d\phi/df$, as described in Zedel and Hay (2010). For the temporal continuity algorithm, offsets of 2π were added to the phase time series for each frequency channel to minimize phase differences between successive samples. Occasional spikes occur in the multi-frequency phase resolution time series due to the difficulty of estimating $d\phi/df$ as $\Delta\phi/\Delta f$ when large amounts of phase noise are present. However, spikes could be removed with low pass filtering or a de-spiking algorithm.

The temporal continuity method shows a much more serious error occurring at $t = 7.7$ seconds. A series of poor quality measurements causes an ambiguity resolution error in the f_1 frequency channel. The error persists until $t = 22.3$ seconds when another error happens to cancel the f_1 error. However, an error occurs in the f_4 channel at $t = 22.5$ seconds, followed by an error in the f_3 channel at $t = 27.5$ seconds. The temporal continuity method is therefore not robust for bursts of low quality measurements such as those occurring at the peak horizontal velocity of 4.0 m s^{-1}. Ambiguity errors for both the multi-frequency phase resolution method and the temporal continuity method disappear when the complex autocorrelation sequence is low pass filtered with a 10 Hz Butterworth filter before calculating velocity measurements. However, low pass filtering leads to a reduction in bandwidth which may be unacceptable for applications in turbulent flow.

6.4.2 Transverse velocity

The MAP velocity estimator was also configured to calculate velocity likelihood functions on a two-dimensional grid extending over ± 5 m s^{-1} in the horizontal direction and ± 1 m s^{-1} in the vertical direction, with a grid spacing of 0.02 m s^{-1}. The rationale for choosing a smaller range for vertical velocity is that, in practice, one-dimensional MAP velocity estimation may be used with centre transducer data to quickly estimate the range of expected radial velocities. Velocity smoothing was performed using $\mathbf{C}_\xi = \sigma^2\mathbf{I}$ and $\sigma = 0.02$ m s^{-1}.

In Figure 6.8, the transverse velocity V_X (i.e. perpendicular to the centre transducer axis) from MAP velocity estimation is compared with the transformation given by (6.14) in Section 6.3. As for the radial case, velocity ambiguity has been removed from the multi-frequency curve in Figure 6.8a by adding multiples of 2π to autocorrelation phase to minimize velocity error.

As before, the MAP estimator operates on raw phase measurements constrained to the interval $[-\pi, \pi]$. The time series of velocity error in Figure 6.8b also shows a periodic increase in measurement error for multi-frequency measurements when velocity amplitude is high. Also, transverse error is greater than radial error from Figure 6.6b, since transverse velocity is more difficult to estimate than radial velocity using a multistatic geometry with small baseline tilt angle, as discussed in Section 6.3. In addition to resolving velocity ambiguity, the MAP velocity estimator produces an error time series in Figure 6.8b with a standard deviation of 0.018 m s^{-1} compared to 0.063 m s^{-1} for the average of multi-frequency measurements. As in Figure 6.6b, reduced RMS error is possible since the MAP velocity estimator weights each mea-

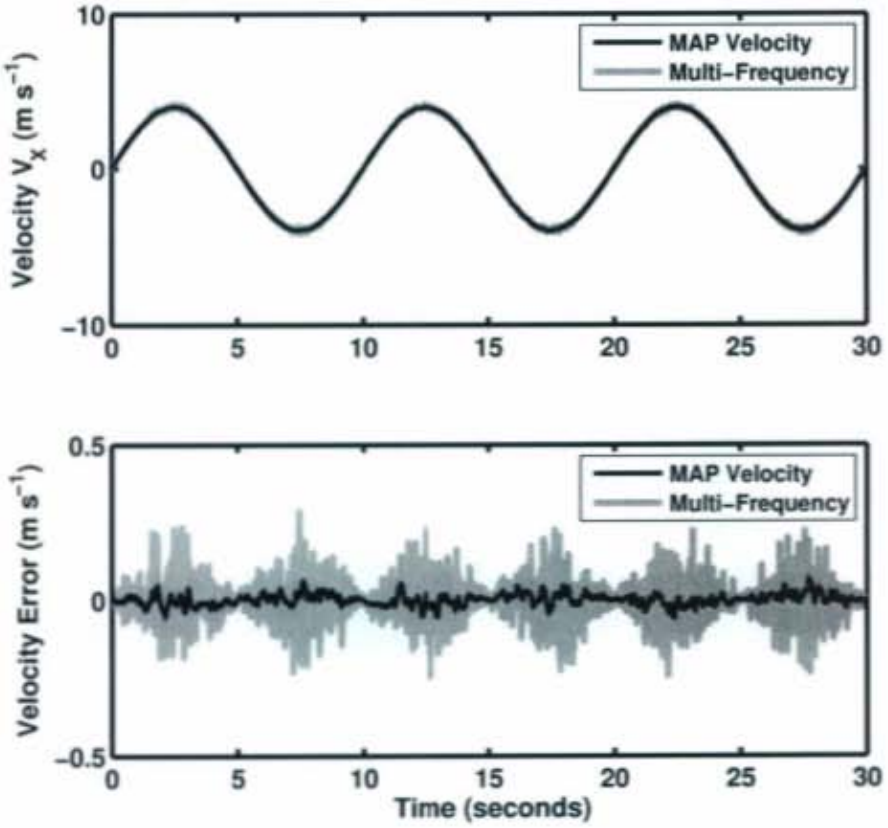

Figure 6.8: Comparison of MAP transverse velocity estimation and averaged multi-frequency measurements. Velocity ambiguity has been removed from the multi-frequency (gray) curve by adding multiples of 2π to autocorrelation phase to minimize velocity error.

surement according to its probability density function.

6.5 Experimental instrumentation

A grid turbulence experiment was performed in the Marine Craft Model Towing Tank at Dalhousie University. The tank has horizontal dimensions of 30 m × 1 m and a

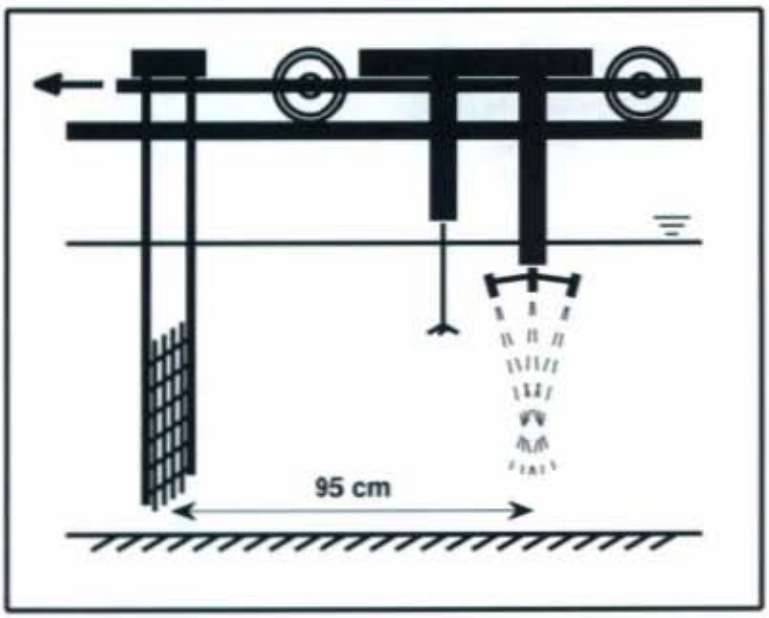

Figure 6.9: Side view schematic of the towing tank showing the MFDop, Vectrino, and rectangular grid. Instrumentation was attached to a carriage that moved along rails mounted above the water. MFDop beam patterns are indicated with dashed lines.

depth of 1 m. An instrumented carriage is propelled by an electric motor along rails mounted above the tank. Carriage speed is computer-controlled and programmable over a range of 0 to 3.0 m s^{-1}. Constant speed is sustained over a rail length of approximately 25 m. The towing carriage, rectangular grid, and instrumentation are shown schematically in Figure 6.9.

Velocity was measured using the MFDop, a multi-frequency coherent Doppler sonar described in Hay et al. (2008). The sonar employs a symmetric multistatic geometry as shown in Figure 6.4 with an angle of 14° between the centre transducer and transducers 1 and 2. The beam intersection point is located 40 cm from the face

of transducer 3. Each transducer has a diameter of 2 cm, a nominal centre frequency of 1.7 MHz, and a bandwidth of approximately 1 MHz. Carrier frequencies, profiling range, range resolution, pulse length, pulse-to-pulse interval, and ensemble length are configurable in software. Nominally, each sample point has a diameter of 2 cm and a height of 3 mm. The parameters in Table 6.1 also apply for the MFDop. The sonar was rotated to point 5° aft (i.e. counter-clockwise in Figure 6.9) to avoid receiving multiple reflections from the tank bottom and water surface. The sonar was located on the tank centre line with the centre transducer 56 cm above the bottom.

Measurements were also collected with a 10 MHz Nortek Vectrino acoustic velocimeter to independently measure carriage speed. The centre transducer of the Vectrino was located 45 cm above the bottom, 16 cm forward of the MFDop centre transducer, and 19 cm to the left side of the tank centre line. Vectrino measurements were recorded at 100 Hz using Vectrino$^+$ firmware. Accuracy is quoted by the manufacturer to be $\pm 0.5\%$ of the measured value.

A rectangular grid was installed 79 cm forward of the Vectrino and 95 cm forward of the MFDop, as indicated in Figure 6.9. The grid consisted of 11×11 aluminum bars with 1 cm square cross-section. Each of the openings between grid elements was square with size $D = 4$ cm. Therefore, the Vectrino was located approximately $20D$ downstream of the grid, corresponding to the beginning of the homogeneous initial period of decay for grid turbulence (Batchelor and Townsend, 1948).

Water in the tank was seeded with agricultural lime. Prior to each run, approximately 0.5 kg of lime was added to replace scatterers lost to settling. An order of magnitude estimate of sediment concentration was 1 g L^{-1}.

Carriage speed was varied from 0.1 to 1.0 m s^{-1} by programming the desired speed

into the control system. Results are presented in Section 6.6 for a nominal speed of 1 m s^{-1}. Due to additional drag from the grid, actual carriage speed was less than the requested value by approximately 10% as determined from velocity measurements with the Vectrino. The control system software automatically calculated an acceleration and deceleration profile to maximize the time at constant speed subject to the tank length constraint.

6.6 Experimental results

Time series of autocorrelation phase and magnitude are shown in Figures 6.10a and 6.10b. MFDop results are presented for transducer 1 at a range of 40 cm for the 2.1 MHz carrier frequency. The towing carriage accelerated to a nominal speed of 1 m s^{-1}, as shown by the time series of horizontal velocity measured by the Vectrino in Figure 6.10c. A phase discontinuity due to velocity ambiguity is evident at the one second mark in Figure 6.10a. Similar results were obtained for carrier frequencies at 1.2, 1.5, and 1.8 MHz, except that the phase discontinuity occurred later (i.e. at a higher carriage speed) for lower carrier frequencies. The time series of autocorrelation magnitude in Figure 6.10b shows a decreasing trend during carriage acceleration. Furthermore, measurement noise increased abruptly as the MFDop entered the turbulent wake of the grid at approximately the two second mark.

Three methods for velocity ambiguity resolution are compared in Figure 6.11a for measurements from a single MFDop receiver in a bistatic configuration. For a sonar tilt angle of 5°, the velocity component V_1 measured by transducer 1 is inclined 12° to the vertical. Therefore, for a carriage speed of 1 m s^{-1}, the V_1 component is nominally

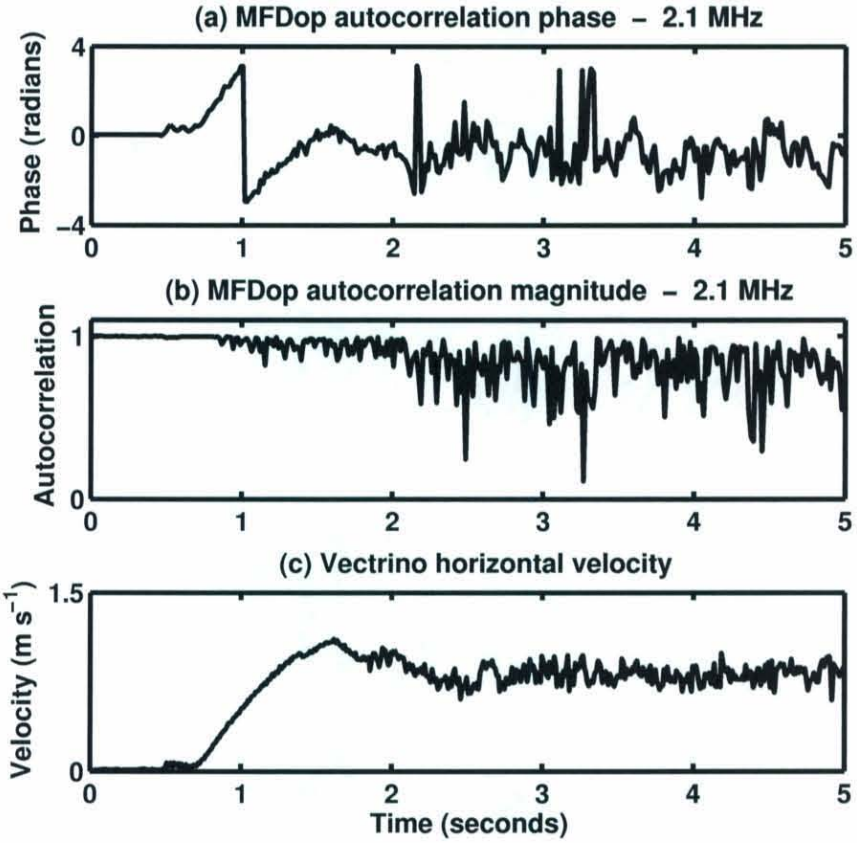

Figure 6.10: Towing carriage acceleration showing: (a) autocorrelation phase from the MFDop, (b) MFDop autocorrelation magnitude, and (c) Vectrino horizontal velocity. MFDop results from transducer 1 are shown for the 40 cm range bin and 2.1 MHz carrier frequency.

0.2 m s^{-1}. In Figure 6.11b, horizontal and vertical Vectrino measurements were rotated by 12° to obtain the V_1 velocity component. Results from one-dimensional MAP velocity estimation in Figure 6.11a were obtained by evaluating velocity likelihood functions over a range of ± 1 m s^{-1} with a grid point spacing of 0.01 m s^{-1} and a smoothing parameter σ of 0.08 m s^{-1}. The multi-frequency time series is the result of applying the method in Zedel and Hay (2010) for velocity ambiguity

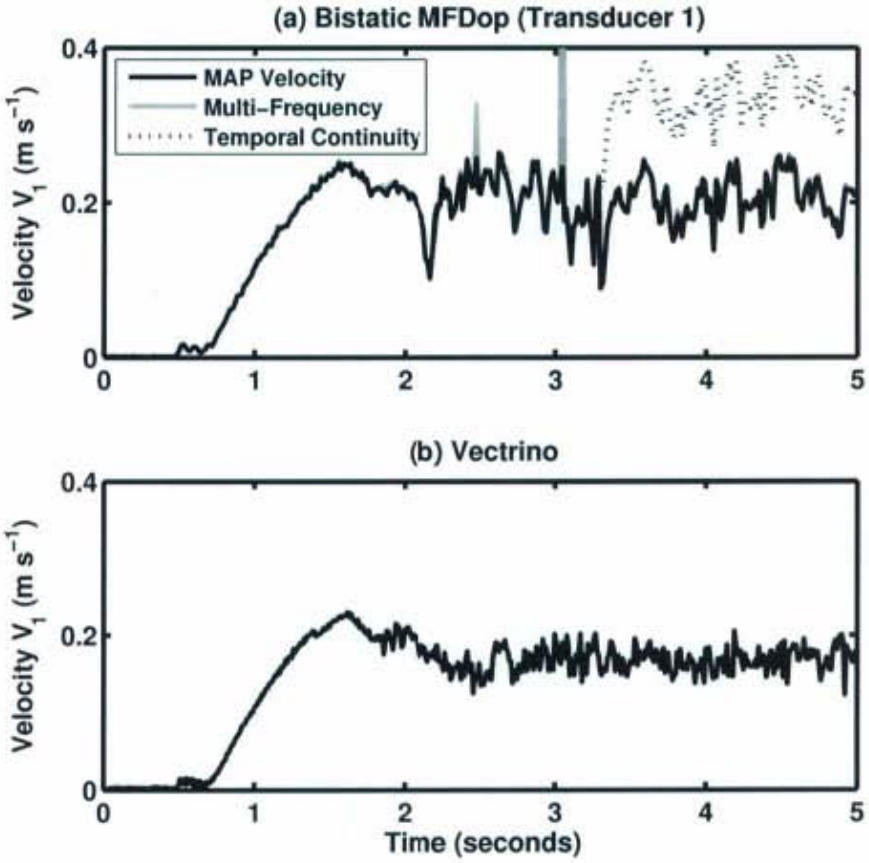

Figure 6.11: Velocity estimation of the V_1 component directed toward the bistatic baseline between transducers 1 and 3 showing: (a) comparison of three methods for velocity ambiguity resolution, and (b) Vectrino measurements rotated by 12° to obtain the V_1 component.

resolution. For the temporal continuity method, multiples of 2π radians were added to the autocorrelation phase of each carrier frequency to minimize discontinuities in time before averaging the results from all carrier frequencies.

Velocity spectra for the multi-frequency and MAP velocity V_1 time series are shown in Figure 6.12 for the steady-state portion of towing carriage motion. Spikes in the multi-frequency time series were removed prior to calculation of the spectrum

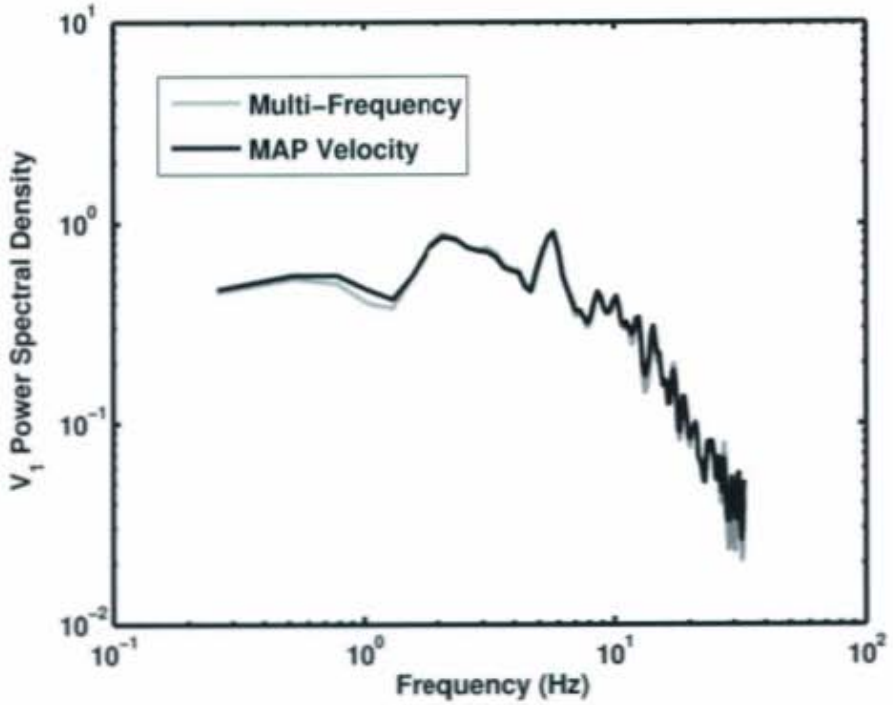

Figure 6.12: Comparison of multi-frequency and MAP velocity spectra for one-dimensional estimation of the V_1 velocity component directed toward the transducer 1 baseline.

by shifting phase measurements by multiples of 2π to best match the MAP velocity time series. Since there is no high frequency noise floor in Figure 6.12, the automatic tuning algorithm in Dillon et al. (2011b) does not apply. Instead, the smoothing parameter of $\sigma = 0.08$ m s^{-1} was obtained by decreasing σ as much as possible without introducing high frequency attenuation in the velocity spectrum. Results similar to Figure 6.12 were obtained when MAP velocity smoothing was applied to measurements from transducers 2 and 3.

In Figure 6.13, the V_X velocity component (i.e. transverse to the MFDop, as shown in Figure 6.4) is estimated from measurements from all three MFDop transducers.

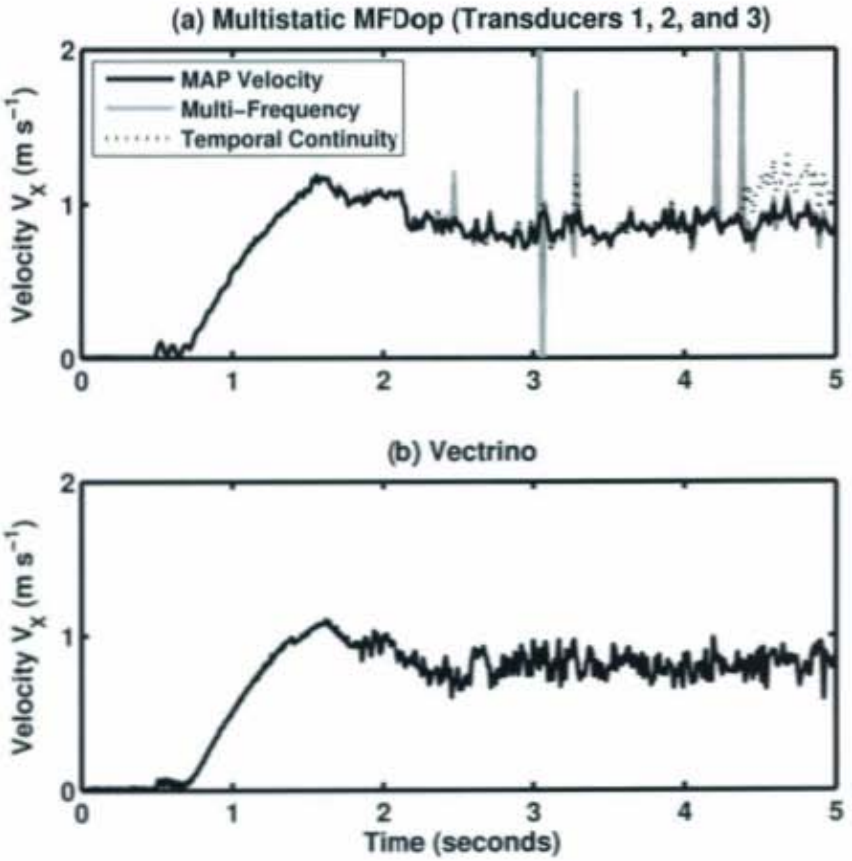

Figure 6.13: Estimation of transverse velocity V_X using multistatic measurements from transducers 1, 2, and 3 showing: (a) comparison of three methods for velocity ambiguity resolution, and (b) Vectrino measurements rotated by 5° to obtain the V_X component.

Results are shown for the range bin at 40 cm. The centre transducer is inclined 5° to the vertical. In Figure 6.13b, horizontal and vertical Vectrino measurements were rotated by 5° to obtain the V_X velocity component. Results from two-dimensional MAP velocity estimation in Figure 6.13a were obtained by evaluating velocity likelihood functions over a horizontal range of 0 to 2 m s^{-1} and a vertical range of ± 1 m s^{-1} with a grid point spacing of 0.01 m s^{-1} and a smoothing parameter σ of

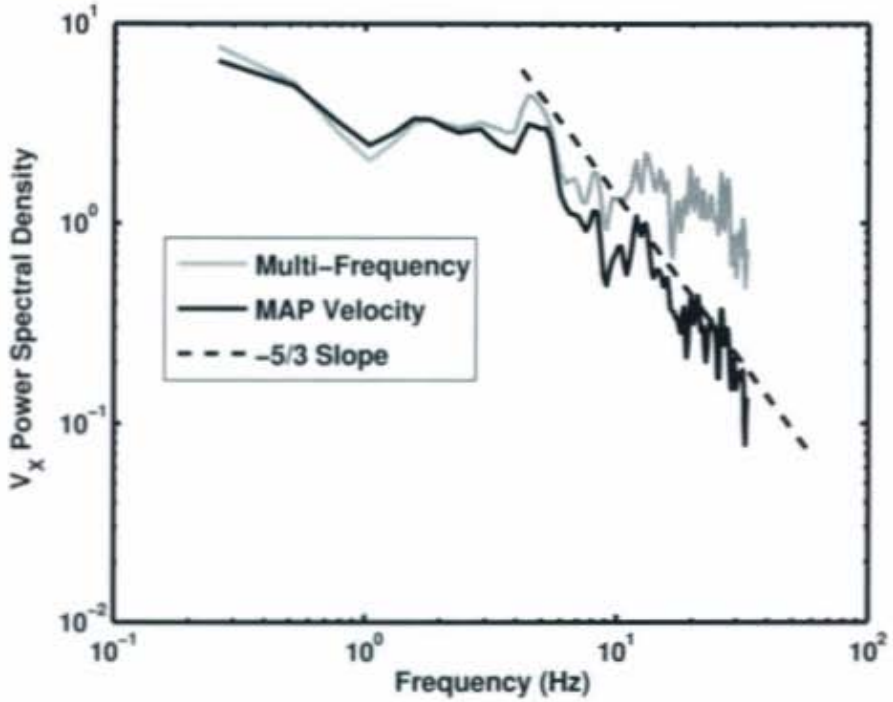

Figure 6.14: Comparison of multi-frequency and MAP velocity spectra for two-dimensional estimation of the V_X component from transducers 1, 2, and 3.

0.08 m s^{-1}, where $\mathbf{C}_\xi = \sigma^2\mathbf{I}$. For multi-frequency and temporal continuity time series, the respective methods were applied to measurements from each transducer before estimating V_X using (6.14).

Velocity spectra for the multi-frequency and MAP velocity V_X time series are shown in Figure 6.14 for the steady-state portion of towing carriage motion. As for the one-dimensional case, spikes in the multi-frequency time series were removed prior to calculation of the spectrum. Also shown in Figure 6.14 is a spectral slope of $-5/3$ corresponding to the inertial subrange of homogeneous isotropic turbulence (Pope, 2000). The Nyquist frequency occurs at 33.3 Hz for a pulse-to-pulse interval of 1.5 ms and ensembles of 10 pulse-pairs. The velocity spectrum for the V_Z component

was similar to Figure 6.12.

6.7 Discussion

An illustrative example was presented in Section 6.3 to show how multi-modal velocity likelihood functions may occur when velocity ambiguity is present. It was shown that estimators based on the posterior mean and median can be biased when the velocity likelihood function is multi-modal. When velocity ambiguity is present, estimators that assume Gaussian statistics (e.g. Kalman filters) are also inappropriate and will lead to biases in velocity estimates. In contrast with classical statistical estimation, MAP estimation makes use of prior knowledge to identify the most likely peak. Two types of prior knowledge result if it is known that (i) velocity lies in some pre-defined range, or (ii) velocity is continuous in time and/or space.

The MAP velocity estimator was developed in Section 6.3. Although the discussion focused on the two-dimensional multistatic geometry shown in Figure 6.4, estimator equations were presented in a way that applies for one-, two-, or three-dimensional velocity estimation. The MAP velocity smoother combines results from forward and backward filtering to eliminate estimator lag and reduce measurement uncertainty. Prior knowledge is derived from a model where the velocity increment from sample to sample is assumed to be discrete-time white Gaussian noise. As the smoothing parameter σ decreases, the likelihood function is increasingly shaped by the assumption of temporal continuity. However, the resulting velocity estimate is not constrained to obey the model precisely since the estimate is ultimately determined by available measurements.

In the prediction step, convolution is implemented by filtering the posterior PDF of the previous sample with a FIR filter having a Gaussian impulse response. MAP velocity estimation could also be applied in the spatial domain. However, spatial smoothing would require an assumption of spatial continuity which may not be valid for shear flows.

A simulation of multi-frequency coherent Doppler sonar measuring an oscillating flow was used to evaluate the MAP velocity estimator via a comparison with the known simulated velocity. Measurement noise was caused by scatterer advection through the sample volume. Numerous phase wraps at $\pm\pi$ were also present due to velocity ambiguity. The one- and two-dimensional MAP velocity estimators were shown to correctly resolve velocity ambiguity while suppressing measurement noise during periods of peak velocity amplitude. The key observation was that although autocorrelation coefficients as low as 0.1 were observed, low quality measurements tended not to occur simultaneously on all frequency channels and for all transducers. Thus, by combining measurements according to their corresponding probability density functions, it was possible to suppress spurious measurements, resulting in an error amplitude that was approximately constant in time despite the varying quality of raw measurements.

The grid turbulence experiment also provided a data set where velocity ambiguity and backscatter decorrelation were present. Time series of autocorrelation phase and magnitude in Figure 6.10 indicate that there was an increase in measurement noise during carriage acceleration, with additional measurement noise occurring as the MFDop entered the turbulent wake of the grid. The Vectrino and MFDop velocity time series in Figures 6.11 and 6.13 are not directly comparable due to the spatial

separation of the sensors, as indicated in Figure 6.9. However, the Vectrino provides an independent measurement of carriage speed which is useful for evaluating the performance of algorithms for velocity ambiguity resolution.

Figures 6.11a and 6.13a show that backscatter decorrelation leads to velocity ambiguity resolution errors for the multi-frequency and temporal continuity methods. Since the multi-frequency method processes each point of the time series independently, occasional errors appear as velocity spikes. The algorithm has no "memory" and therefore spikes can be removed with a de-spiking algorithm. The temporal continuity method, on the other hand, has infinite memory, in the sense that ambiguity resolution errors persist indefinitely unless two errors happen to cancel. MAP velocity smoothing can be interpreted as a compromise between these two extremes where the best features of each approach are retained. The estimator incorporates temporal information to help choose the correct peak in a multi-modal velocity likelihood function. However, temporal continuity is not enforced in a strict sense, and the estimator is able to recover if an error occurs. The two-dimensional MAP velocity estimator is more tolerant of measurement noise than one-dimensional methods since probability distributions from all three transducers are combined before estimating velocity.

While large amplitude spikes may be removed from the velocity time series, lower amplitude measurement noise is difficult to separate from real turbulent fluctuations. Averaging and low pass filtering are frequently applied to reduce measurement errors; however, there is a corresponding reduction in effective sample rate and bandwidth. Ideally, noise suppression methods would improve velocity estimates while preserving the sample rate and bandwidth of the original data. Figures 6.11 and 6.12 show an

example where one-dimensional MAP velocity estimation robustly resolved velocity ambiguity without introducing high frequency attenuation in the velocity spectrum. If a noise floor had been present in the velocity spectrum, the one-dimensional estimator could also be used to suppress noise, as demonstrated in Dillon et al. (2011b). Since the MAP velocity estimator operates in the time domain, a smoothed time series at the full sonar sample rate is produced (e.g. Figures 6.11a and 6.13a) in addition to the smoothed spectra shown in Figures 6.12 and 6.14.

For transverse velocity measurement, the component V_X is more difficult to estimate than radial velocity using a multistatic geometry with small baseline tilt angle. Figures 6.13 and 6.14 show that two-dimensional MAP velocity estimation suppresses high frequency noise inherent in transverse velocity measurement while resolving velocity ambiguity and retaining high frequency fluctuations characteristic of turbulent flow. Comparison of Figures 6.12 and 6.14 illustrates how two-dimensional MAP velocity estimation differs from the one-dimensional case. The two-dimensional estimator projects measurements from each transducer onto the space of Cartesian components $[v_x, v_z]$ so that each measurement is weighted according to the geometry of the sonar in addition to the corresponding autocorrelation coefficient. Smoothing is then applied to $[v_x, v_z]$ rather than to the time series from each transducer.

Velocity likelihood functions were evaluated on a discrete set of grid points to estimate the maximum value of the posterior PDF. Although the grid search is not computationally efficient, there are no convergence issues and the search produces the global maximum when the grid spacing is small compared to the width of peaks in the posterior PDF. Velocity estimates were refined by fitting a Gaussian peak to a 3×3 grid of points in the vicinity of the maximum value, as is typically performed

for sub-pixel estimation in particle image velocimetry (Raffel et al., 2007, chap. 5). Using the peak fitting algorithm, velocity results were not sensitive to the choice of grid point spacing. Future work will investigate the use of an adaptive mesh and more sophisticated optimization algorithms to improve computational efficiency.

6.8 Conclusions

In this chapter, a velocity estimator for coherent Doppler sonar has been described. The estimator employs MAP estimation to optimally combine multi-frequency and multi-transducer measurements. The estimation framework accommodates monostatic, bistatic, and multistatic sonar configurations. The algorithm operates on a time series of measurements from a single point in space. Spatial smoothing is also possible if the flow can be assumed to be spatially continuous. Each phase measurement is weighted according to a PDF determined by a corresponding autocorrelation coefficient. A user-configurable smoothing parameter controls how measurements are combined in the time domain. The MAP velocity estimator was evaluated using a high fidelity coherent Doppler sonar simulation of oscillating flow. Results were also presented from a towing tank grid turbulence experiment where both velocity ambiguity and backscatter decorrelation were present. Time series and spectra from MAP velocity estimation were compared to those obtained with conventional Doppler signal processing. In addition to robustly resolving velocity ambiguity, the MAP velocity estimator was shown to reduce high frequency noise in turbulence spectra.

Bibliography

Batchelor, G. K. and Townsend, A. A. (1948). Decay of isotropic turbulence in the initial period. *Proceedings of the Royal Society of London. Series A, Mathematical and Physical Sciences*, 193(1035):539–558.

Box, G. E. P. and Tiao, G. C. (1973). *Bayesian Inference in Statistical Analysis.* Addison-Wesley.

Brumley, B. H., Cabrera, R. G., Deines, K. L., and Terray, E. A. (1991). Performance of a broad-band acoustic Doppler current profiler. *IEEE Journal of Oceanic Engineering*, 16(4):402–407.

Dillon, J., Zedel, L., and Hay, A. E. (2011a). Asymptotic properties of an autocorrelation coefficient for coherent Doppler sonar. *Journal of Atmospheric and Oceanic Technology*, 28(7):966–973.

Dillon, J., Zedel, L., and Hay, A. E. (2011b). Automatic tuning of a velocity estimator for pulse-to-pulse coherent Doppler sonar. In *Proceedings of the IEEE/OES 10th Current, Waves, and Turbulence Measurement Workshop*, pages 230–236.

Dillon, J., Zedel, L., and Hay, A. E. (2011c). On the distribution of velocity measurements from pulse-to-pulse coherent Doppler sonar. *IEEE Journal of Oceanic Engineering, submitted.*

Franca, M. J. and Lemmin, U. (2006). Eliminating velocity aliasing in acoustic

Doppler velocity profiler data. *Measurement Science and Technology*, 17(2):313–322.

Garbini, J. L., Forster, F. K., and Jorgensen, J. E. (1982). Measurement of fluid turbulence based on pulsed ultrasound techniques. Part 1. Analysis. *Journal of Fluid Mechanics*, 118:445–470.

Hay, A. E. (2008). Near-bed turbulence and relict waveformed sand ripples: Observations from the inner shelf. *Journal of Geophysical Research*, 113(C04040), doi:10.1029/2006JC004013.

Hay, A. E., Zedel, L., Craig, R., and Paul, W. (2008). Multi-frequency, pulse-to-pulse coherent Doppler sonar profiler. In *Proceedings of the IEEE/OES 9th Working Conference on Current Measurement Technology*, pages 25–29.

Hurther, D. and Lemmin, U. (2001). A correction method for turbulence measurements with a 3D acoustic Doppler velocity profiler. *Journal of Atmospheric and Oceanic Technology*, 18(3):446–458.

Hurther, D. and Lemmin, U. (2008). Improved turbulence profiling with field-adapted acoustic Doppler velocimeters using a bifrequency Doppler noise suppression method. *Journal of Atmospheric and Oceanic Technology*, 25(3):452–463.

Kay, S. M. (1993). *Fundamentals of Statistical Signal Processing: Estimation Theory*, volume 1. Prentice-Hall PTR.

Lhermitte, R. (1983). Doppler sonar observation of tidal flow. *Journal of Geophysical Research*, 88(C1):725–742.

Lhermitte, R. and Serafin, R. (1984). Pulse-to-pulse coherent Doppler sonar signal processing techniques. *Journal of Atmospheric and Oceanic Technology*, 1(4):293–308.

Lohrmann, A., Hackett, B., and Røed, L. P. (1990). High resolution measurements of turbulence, velocity and stress using a pulse-to-pulse coherent sonar. *Journal of Atmospheric and Oceanic Technology*, 7(1):19–37.

Nitzpon, H. J., Rajaonah, J. C., Burckhardt, C. B., Dousse, B., and Meister, J. J. (1995). A new pulsed wave Doppler ultrasound system to measure blood velocities beyond the Nyquist limit. *IEEE Transactions on Ultrasonics, Ferroelectrics, and Frequency Control*, 42(2):265–279.

Plueddemann, A. J. (1992). Internal wave observations from the Arctic environmental drifting buoy. *Journal of Geophysical Research*, 97(C8):12619–12638.

Pope, S. B. (2000). *Turbulent Flows*. Cambridge University Press.

Raffel, M., Willert, C. E., Wereley, S. T., and Kompenhans, J. (2007). *Particle Image Velocimetry: A Practical Guide*. Springer, second edition.

Ray, P. S. and Ziegler, C. (1977). De-aliasing first moment Doppler estimates. *Journal of Applied Meteorology*, 15(5):563–564.

Rosenthal, J. S. (2000). *A First Look at Rigorous Probability Theory*. World Scientific.

Rowe, F. D., Deines, K. L., and Gordon, R. L. (1986). High resolution current profiler. In *Proceedings of the IEEE 3rd Working Conference on Current Measurement*, volume 3, pages 184–189.

Smyth, C. and Hay, A. E. (2003). Near-bed turbulence and bottom friction during SandyDuck97. *Journal of Geophysical Research*, 108(C6), 3197, doi:10.1029/2001JC000952.

Smyth, C., Hay, A. E., and Zedel, L. (2002). Coherent Doppler profiler measurements of near-bed suspended sediment fluxes and the influence of bed forms. *Journal of Geophysical Research*, 107(C8), 3105, doi:10.1029/2000JC000760.

Veron, F. and Melville, W. K. (1999). Pulse-to-pulse coherent Doppler measurements of waves and turbulence. *Journal of Atmospheric and Oceanic Technology*, 16(11):1580–1597.

Zedel, L. (2008). Modeling pulse-to-pulse coherent Doppler sonar. *Journal of Atmospheric and Oceanic Technology*, 25(10):1834–1844.

Zedel, L. and Hay, A. E. (2010). Resolving velocity ambiguity in multifrequency, pulse-to-pulse coherent Doppler sonar. *IEEE Journal of Oceanic Engineering*, 35(4):847–851.

Zedel, L., Hay, A. E., Cabrera, R., and Lohrmann, A. (1996). Performance of a single-beam pulse-to-pulse coherent Doppler profiler. *IEEE Journal of Oceanic Engineering*, 21(3):290–297.

Zrnić, D. S. (1977). Spectral moment estimates from correlated pulse pairs. *IEEE Transactions on Aerospace and Electronic Systems*, AES-13(4):344–354.

Chapter 7

Conclusions

7.1 Summary

The following thesis objectives were outlined in Section 1.4:

1. To apply MAP estimation to multi-frequency coherent Doppler sonar for the purpose of resolving velocity ambiguity and suppressing measurement noise simultaneously rather than separately;

2. To develop an estimation framework that accommodates commonly used sonar geometries such as one-dimensional single beam systems, ADCPs with divergent beams, three-dimensional velocity point sensors, and profiling sonars;

3. To ensure that the estimator depends solely on physical parameters of the sonar and is free from instrument-specific and application-specific constants;

4. To evaluate MAP velocity estimation using numerical simulation and laboratory experiments under realistic and challenging operating conditions.

The above objectives have been successfully achieved, culminating in the development of the multi-dimensional MAP velocity estimator in Chapter 6. The approach taken in this thesis to resolve objectives 1–4 is summarized below.

A new formula was derived in Chapter 3 for the asymptotic form of an autocorrelation coefficient that provides a measure of data quality for coherent Doppler sonar. Theoretical analysis and numerical simulation showed that the autocorrelation coefficient is a biased estimator for finite pulse-pair averages and in the limit of infinite ensemble length. Validity of the results from a Gaussian random process was confirmed using a high fidelity coherent Doppler sonar model, and using sonar measurements in a towing tank where the towing carriage travelled at constant speed. The experiment showed that the distribution of observed autocorrelation coefficients is well-predicted by a Gaussian random process once the autocorrelation bias has been removed. The results of Chapter 3 served to relate the observed coefficient from a finite ensemble to the actual pulse-to-pulse backscatter autocorrelation.

In Chapter 4, numerical simulation of a Gaussian random process was used to investigate dependence of the velocity measurement distribution on ensemble length and the degree of backscatter autocorrelation. A formula was presented for the distribution of a single pulse-pair phase measurement. In the limit of perfect pulse-to-pulse autocorrelation, the phase distribution tended to a Pearson Type VII distribution which has a higher peak and broader tails compared to a normal distribution. Evaluation of second and fourth moments showed that the phase distribution exhibits non-normal behaviour over a range of parameter values. Simulation results also indicated the range of values for which perturbation analysis fails to accurately predict velocity variance. For example, for ensemble lengths less than 4 pulse-pairs, the ratio of phase

standard deviation to that predicted by perturbation analysis differs from unity by at least 5% for all values of the autocorrelation coefficient. Thus, for short ensemble lengths, e.g. between 2 and 10 pulse-pairs, the measurement PDF must be determined from numerical simulation. Results from a coherent Doppler sonar model showed that simulation of a Gaussian random process is sufficient to predict the distribution of velocity measurements.

In Chapter 5, the one-dimensional MAP velocity estimator was developed for multi-frequency measurements from a monostatic sonar. Using results from Chapters 3 and 4, each phase measurement was weighted according to a PDF determined by its corresponding autocorrelation magnitude. A user-configurable smoothing parameter controlled how measurements were combined in the time domain. A method was presented for automatically determining the smoothing parameter from examination of the spectrum of a representative segment of the measurement time series. The method was evaluated using results from a laboratory turbulent jet where velocity was measured simultaneously with multi-frequency coherent Doppler sonar and particle image velocimetry. Automatic tuning of the estimator resulted in a velocity time series where measurement noise was suppressed while high frequency turbulence fluctuations were retained. Once the smoothing parameter was chosen using the tuning procedure, the MAP velocity estimator was free from empirically determined constants specific to a particular instrument or application, satisfying objective 3.

MAP velocity estimation was generalized to multistatic geometries in Chapter 6 to satisfy objective 2. The estimator was evaluated using numerical simulation of oscillating flow and results from a towing tank grid turbulence experiment. For simulation and experiment, both velocity ambiguity and backscatter decorrelation

were present, thereby satisfying objective 4 with a challenging test of the estimator under realistic conditions. Time series and spectra from MAP velocity estimation were compared to those obtained with conventional Doppler signal processing. Objective 1 was satisfied since the MAP velocity estimator was shown to reduce high frequency noise while robustly resolving velocity ambiguity.

7.2 Future work

The long-term goal of this work is to develop improved signal processing for oceanographic and hydraulic instrumentation that will contribute to new insights into the dynamics of near-bed turbulence and sediment transport. In this thesis, the MAP velocity estimator has been developed and evaluated using numerical simulation and laboratory tests in steady and turbulent flows. The next logical step is to collect sonar measurements in the ocean bottom boundary layer under conditions where the mean flow is sufficient to induce velocity ambiguity, and where boundary layer turbulence results in backscatter decorrelation. A field experiment involving the multi-frequency coherent Doppler sonar described in Hay et al. (2008) is planned for Fall 2011 in a tidal passage in the Bay of Fundy. It would be useful to compare MAP estimates of velocity and shear stress with results from conventional Doppler signal processing, boundary layer theory, and other sensors.

The MAP velocity algorithm is expected to always perform at least as well as conventional Doppler signal processing since the MAP framework always includes the maximum likelihood estimate ($\sigma \rightarrow \infty$) as a possibility. The relevant question for practical applications is whether or not the benefits justify the increase in com-

putational cost. For example, processing times for one- and two-dimensional MAP velocity estimation are listed in Table 7.1 for the MFDop simulations of oscillating flow in Section 6.4. Clearly, processing time increases rapidly with the dimension of the velocity vector (the so-called "curse of dimensionality"). A reasonable compromise may be to perform one-dimensional MAP velocity estimation for each receiver and then transform the results to obtain Cartesian velocity components.

Table 7.1: Processing time for conventional Doppler signal processing and MAP velocity estimation for 30 seconds of simulated MFDop measurements.

Dimension	Conventional	MAP Velocity
1D	0.01 s	3 s
2D	0.03 s	200 s

The estimator has been coded as a proof-of-concept in MATLAB with an emphasis on ease of implementation rather than computational efficiency. Also, no effort has been made to parallelize the algorithm to make use of multi-core processors. Velocity likelihood functions were evaluated on a discrete grid of evenly spaced points. A more efficient approach would be to use an adaptive mesh, coded in C or FORTRAN, with sample points concentrated in the region of highest likelihood. An adaptive mesh would take advantage of the fact that the distribution of velocity likelihood tends to be sparse, especially in higher dimensions. If the results from field experiments are promising, it may be worthwhile to develop a commercial software package for post-processing of coherent Doppler sonar measurements.

While the focus of this work has been on measurement of sediment-laden flows for laboratory and oceanographic applications, the results are immediately applicable to other systems that employ the coherent Doppler measurement principle. For exam-

ple, as discussed in Chapter 1, a bi-frequency acoustic Doppler system for medical ultrasound has been developed and tested (Nitzpon et al., 1995). For applications in Doppler weather radar, dual pulse repetition frequencies (PRFs) have been more widely used than multiple carrier frequencies (Holleman and Beekhuis, 2003; Joe and May, 2003). However, the principles of MAP velocity estimation apply equally well for staggered PRF systems since variation of the pulse-to-pulse interval and variation of the carrier frequency produce equivalent changes in the ambiguity velocity.

The idea of combining measurements probabilistically according to some measure of data quality is a useful and powerful concept that has been applied in other fields such as multi-sensor data fusion (Hall and Llinas, 1997) and radio direction finding (Elsaesser, 2007). An approach analogous to MAP velocity estimation could be useful for applications that seek to estimate a time series from uncertain and possibly ambiguous measurements. Research areas which could lead to fruitful new results include the resolution of carrier phase ambiguities in differential GPS (Cannon et al., 1993), angle-of-arrival estimation for array signal processing (Kraeutner and Bird, 1999), phase ambiguities in interferometric sonar/radar (Budillon et al., 2005), and estimation of directional wave spectra from high frequency surface wave radar (Hashimoto and Tokuda, 1999).

Appendix A

Particle Image Velocimetry

A.1 Image processing

In particle image velocimetry (PIV), velocity components are measured in the plane of the laser light sheet by observing the mean particle displacement $\mathbf{d}$ in a region of the camera field of view known as an interrogation window (Raffel et al., 2007, chap. 1). Velocity is related to particle displacement via

$$\mathbf{v} = \frac{\mathbf{d}}{T_p} \tag{A.1}$$

where T_p is the time between laser pulses. Mean displacement is determined by cross-correlating a pair of images and estimating the location of the peak of the 2D cross-correlation function. Displacements in units of pixels are converted to spatial units by applying a length scale that is determined by the calibration process described in Section A.2.

PIV velocity estimation was performed using the adaptive correlation method

in version 4.71 of the Dantec Dynamics FlowManager software (Dantec Dynamics, 2002). Interrogation window size was set to 64×64 pixels with 50% overlap to ensure that each window contains a minimum of 5 particles (Raffel et al., 2007, chap. 5). The following Gaussian window function was applied to each image:

$$G(m,n) = \exp\left[-\frac{1}{k^2}\left(\left(\frac{2m}{W}\right)^2 + \left(\frac{2n}{W}\right)^2\right)\right] \tag{A.2}$$

where $k = 0.71$ corresponds to 50% overlap and $W = 64$ is the window size in pixels. The window function acts as a low pass filter to remove high frequency image noise and to ensure that each particle diameter appears as a minimum of two pixels in the filtered image (Raffel et al., 2007, chap. 5). The FlowManager software implements image cross-correlation using a 2D Fast Fourier Transform (FFT). Background illumination was removed with the high pass "No-DC" filter

$$H(u,v) = \begin{cases} 0 & \text{for } (u,v) = (0,0) \\ 1 & \text{otherwise} \end{cases} \tag{A.3}$$

where (u, v) denotes horizontal and vertical components of the Fourier transform.

Image noise and the random distribution of seeding particles cause occasional spurious measurements. Outliers were detected using 3×3 local median validation with a normalized threshold of 0.1 (Dantec Dynamics, 2002, chap. 9). Each vector field was also inspected visually to identify any obviously incorrect measurements that had passed the local median test. Spurious values were replaced with interpolated values. The overall rate of spurious vectors was below 0.5%, which is considered

acceptable for high quality PIV measurements (Raffel et al., 2007, chap. 6).

A.2 Calibration

The jet centre-line was located by suspending a $^3/_{32}$ inch diameter rod from the centre of the nozzle. Alignment of the laser light sheet with the jet centre-line was achieved by firing the laser on its low power setting and positioning the periscope to achieve maximum brightness on the rod. The length scale was calibrated by photographing the rod with the PIV camera and measuring the rod diameter in pixels. A reference mark was placed on the rod to indicate a vertical distance from the nozzle. The location of the mark within the calibration image provided a vertical reference to locate PIV measurements relative to the nozzle. The intersection point between the jet centre-line, the light sheet, and sonar centre transducer beam pattern was located 44 cm below the nozzle.

Appendix B

Gaussian Interpolation

MAP velocity estimation is implemented by evaluating the velocity likelihood function on a grid of points. Once the maximum value has been identified, estimation of the peak location may be refined via Gaussian interpolation, as indicated in Figure B.1. Equations for peak location and peak width (i.e. standard deviation) are derived in Sections B.1 and B.2 for estimation of one and two velocity components. One- and two-dimensional estimators are widely used in particle image velocimetry for improved measurement accuracy (Raffel et al., 2007, chap. 5).

B.1 One-dimensional interpolation

Let p_-, p_0, and p_+ denote values of the PDF sampled at points $-\Delta v$, 0, and Δv relative to the location v_0 of the maximum value. The function $p(v)$ is assumed to be described a Gaussian function

$$p(v) = A\, e^{-\frac{(v-v_p)^2}{2\sigma_v^2}} \tag{B.1}$$

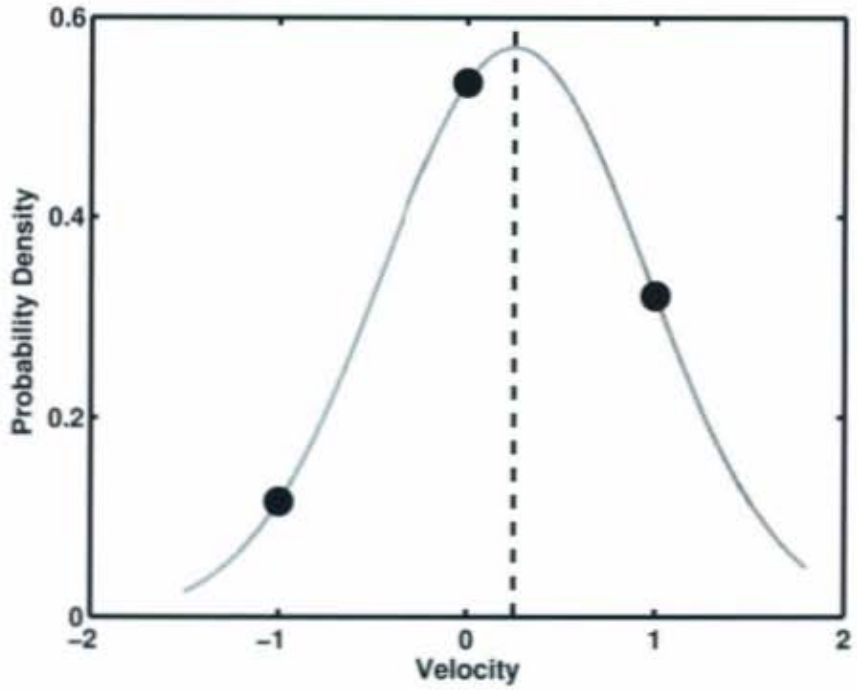

Figure B.1: Example three point Gaussian interpolation. The peak is located at $v = 0.25$, as indicated by the dashed vertical line.

where v_p is the location of the peak and σ_v^2 describes the peak width. Equation (B.1) is equivalent to

$$\ln p = \ln A - \frac{(v - v_p)^2}{2\sigma_v^2}. \tag{B.2}$$

Therefore, peak estimation may be performed by fitting values of $\ln p$ to a quadratic function

$$\ln p = a_0 + a_1 v + a_2 v^2 \tag{B.3}$$

where coefficients a_i are to be determined. In matrix form, the following equation is satisfied:

$$\begin{bmatrix} 1 & -\Delta v & (\Delta v)^2 \\ 1 & 0 & 0 \\ 1 & \Delta v & (\Delta v)^2 \end{bmatrix} \begin{bmatrix} a_0 \\ a_1 \\ a_2 \end{bmatrix} = \begin{bmatrix} \ln p_- \\ \ln p_0 \\ \ln p_+ \end{bmatrix}. \tag{B.4}$$

Inversion of the 3×3 matrix in (B.4) results in

$$\begin{bmatrix} a_0 \\ a_1 \\ a_2 \end{bmatrix} = \begin{bmatrix} \ln p_0 \\ \frac{\ln p_+ - \ln p_-}{2\Delta v} \\ \frac{\ln p_+ - 2\ln p_0 + \ln p_-}{2(\Delta v)^2} \end{bmatrix}. \tag{B.5}$$

Comparison of (B.2) and (B.3) reveals that

$$\sigma_v^2 = -\frac{1}{2a_2} = -\frac{(\Delta v)^2}{\ln p_+ - 2\ln p_0 + \ln p_-}. \tag{B.6}$$

Setting the derivative of (B.3) equal to zero produces

$$\frac{\partial}{\partial v} \ln p(v) = a_1 + 2a_2 v = 0. \tag{B.7}$$

The estimate of the peak location is given by

$$v_p = -\frac{a_1}{2a_2} = \frac{(\Delta v)(\ln p_- - \ln p_+)}{2(\ln p_+ - 2\ln p_0 + \ln p_-)} \tag{B.8}$$

which is in agreement with Raffel et al. (2007, chap. 5).

B.2 Two-dimensional interpolation

The two-dimensional equation for a Gaussian peak is

$$\begin{aligned}\ln p &= \ln A - \frac{1}{2}\begin{bmatrix} u-u_p \\ v-v_p \end{bmatrix}^T \begin{bmatrix} \sigma_u^2 & \kappa\sigma_u\sigma_v \\ \kappa\sigma_u\sigma_v & \sigma_v^2 \end{bmatrix}^{-1} \begin{bmatrix} u-u_p \\ v-v_p \end{bmatrix} \\ &= \ln A - \frac{1}{2(1-\kappa^2)}\left[\frac{(u-u_p)^2}{\sigma_u^2} - \frac{2\kappa(u-u_p)(v-v_p)}{\sigma_u\sigma_v} + \frac{(v-v_p)^2}{\sigma_v^2}\right] \end{aligned} \tag{B.9}$$

where κ is the skewness of the distribution. The corresponding quadratic form is

$$\ln p = a_{00} + a_{10}u + a_{01}v + a_{11}uv + a_{20}u^2 + a_{02}v^2. \tag{B.10}$$

When $p(u, v)$ is sampled on a 3×3 neighbourhood of the maximum value, the matrix form of (B.10) is given by

$$\begin{bmatrix} 1 & -\Delta u & -\Delta v & \Delta u\Delta v & (\Delta u)^2 & (\Delta v)^2 \\ 1 & -\Delta u & 0 & 0 & (\Delta u)^2 & 0 \\ 1 & -\Delta u & \Delta v & -\Delta u\Delta v & (\Delta u)^2 & (\Delta v)^2 \\ 1 & 0 & -\Delta v & 0 & 0 & (\Delta v)^2 \\ 1 & 0 & 0 & 0 & 0 & 0 \\ 1 & 0 & \Delta v & 0 & 0 & (\Delta v)^2 \\ 1 & \Delta u & -\Delta v & -\Delta u\Delta v & (\Delta u)^2 & (\Delta v)^2 \\ 1 & \Delta u & 0 & 0 & (\Delta u)^2 & 0 \\ 1 & \Delta u & \Delta v & \Delta u\Delta v & (\Delta u)^2 & (\Delta v)^2 \end{bmatrix} \begin{bmatrix} a_{00} \\ a_{10} \\ a_{01} \\ a_{11} \\ a_{20} \\ a_{02} \end{bmatrix} = \begin{bmatrix} \ln p_{--} \\ \ln p_{-0} \\ \ln p_{-+} \\ \ln p_{0-} \\ \ln p_{00} \\ \ln p_{0+} \\ \ln p_{+-} \\ \ln p_{+0} \\ \ln p_{++} \end{bmatrix}, \tag{B.11}$$

or, in symbolic form,

$$\mathbf{Ha} = \ln \mathbf{p}. \tag{B.12}$$

The vector $\mathbf{a}$ is found by least squares estimation (Luenberger, 1969, chap. 4),

$$\mathbf{a} = (\mathbf{H}^T\mathbf{H})^{-1}\mathbf{H}^T \ln \mathbf{p}. \tag{B.13}$$

An explicit solution for the case $\Delta u = \Delta v$ is presented in Nobach and Honkanen (2005). Alternatively, (B.13) may be evaluated numerically. Comparison of (B.9) and (B.10) reveals that

$$\begin{bmatrix} \sigma_u^2 & \kappa\sigma_u\sigma_v \\ \kappa\sigma_u\sigma_v & \sigma_v^2 \end{bmatrix} = -\frac{1}{2}\begin{bmatrix} a_{20} & \frac{1}{2}a_{11} \\ \frac{1}{2}a_{11} & a_{02} \end{bmatrix}^{-1}. \tag{B.14}$$

Therefore,

$$\sigma_u^2 = \frac{2a_{02}}{(a_{11})^2 - 4a_{20}a_{02}}, \tag{B.15}$$

$$\sigma_v^2 = \frac{2a_{20}}{(a_{11})^2 - 4a_{20}a_{02}}. \tag{B.16}$$

Setting the partial derivatives of (B.10) equal to zero produces

$$\frac{\partial}{\partial u}\ln p = a_{10} + a_{11}v + 2a_{20}u = 0, \tag{B.17}$$

$$\frac{\partial}{\partial v}\ln p = a_{01} + a_{11}u + 2a_{02}v = 0. \tag{B.18}$$

The estimate of the peak location is given by

$$u_p = \frac{2a_{02}a_{10} - a_{01}a_{11}}{(a_{11})^2 - 4a_{20}a_{02}}, \tag{B.19}$$

$$v_p = \frac{2a_{20}a_{01} - a_{10}a_{11}}{(a_{11})^2 - 4a_{20}a_{02}}. \tag{B.20}$$

The above expression is in agreement with Nobach and Honkanen (2005).

Bibliography

Ahn, Y. B. and Park, S. B. (1991). Estimation of mean frequency and variance of ultrasonic Doppler signal by using second-order autoregressive model. *IEEE Transactions on Ultrasonics, Ferroelectrics, and Frequency Control*, 38(3):172–182.

Barber, W. D., Eberhard, J. W., and Karr, S. G. (1985). A new time domain technique for velocity measurements using Doppler ultrasound. *IEEE Transactions on Biomedical Engineering*, BME-32(3):213–229.

Barclay, P. J., Hayes, M. P., and Gough, P. T. (2003). Reconstructing seafloor bathymetry with a multi-frequency, multi-channel broadband InSAS using belief propagation. In *Proceedings of the MTS/IEEE OCEANS Conference*, volume 4, pages 2149–2155.

Batchelor, G. K. and Townsend, A. A. (1947). Decay of vorticity in isotropic turbulence. *Proceedings of the Royal Society of London. Series A, Mathematical and Physical Sciences*, 190(1023):534–550.

Batchelor, G. K. and Townsend, A. A. (1948a). Decay of isotropic turbulence in the initial period. *Proceedings of the Royal Society of London. Series A, Mathematical and Physical Sciences*, 193(1035):539–558.

Batchelor, G. K. and Townsend, A. A. (1948b). Decay of turbulence in the final period. *Proceedings of the Royal Society of London. Series A, Mathematical and Physical Sciences*, 194(1039):527–543.

Bergen, W. R. and Albers, S. C. (1988). Two- and three-dimensional de-aliasing of Doppler radar velocities. *Journal of Atmospheric and Oceanic Technology*, 5(2):305–319.

Blanckaert, K. and Lemmin, U. (2006). Means of noise reduction in acoustic turbulence measurements. *Journal of Hydraulic Research*, 44(1):3–17.

Bonnefous, O., Pesqué, P., and Bernard, X. (1986). A new velocity estimator for color flow mapping. In *Proceedings of the IEEE Ultrasonics Symposium*, pages 855–860.

Boudreau, B. P. and Jørgensen, B. B., editors (2001). *The Benthic Boundary Layer: Transport Processes and Biogeochemistry.* Oxford University Press.

Bourgault, D., Blokhina, M. D., Mirshak, R., and Kelley, D. E. (2007). Evolution of a shoaling internal solitary wavetrain. *Geophysical Research Letters*, 34(L03601), doi:10.1029/2006GL028462.

Box, G. E. P. and Tiao, G. C. (1973). *Bayesian Inference in Statistical Analysis.* Addison-Wesley.

Budillon, A., Ferraiuolo, G., Pascazio, V., and Schirinzi, G. (2005). Multichannel SAR interferometry via classical and Bayesian estimation techniques. *EURASIP Journal on Applied Signal Processing*, 20:3180–3193.

Cannon, M. E., Lachapelle, G., and Lu, G. (1993). Kinematic ambiguity resolution with highprecision C/A code receiver. *Journal of Surveying Engineering*, 119(4):147–155.

Chien, N. and Wan, Z. (1999). *Mechanics of Sediment Transport.* ASCE Press.

Cobbold, R. S. C. (2007). *Foundations of Biomedical Ultrasound.* Oxford University Press.

Comte-Bellot, G. and Corrsin, S. (1966). The use of a contraction to improve the isotropy of grid-generated turbulence. *Journal of Fluid Mechanics*, 25(4):657–682.

Crow, S. C. and Champagne, F. H. (1971). Orderly structure in jet turbulence. *Journal of Fluid Mechanics*, 48(3):547–591.

Dantec Dynamics (2002). *FlowManager Software and Introduction to PIV Instrumentation: Software User's Guide.* `http://www.dantecdynamics.com/Default.aspx?ID=1680`.

David, J.-Y., Jones, S. A., and Giddens, D. P. (1991). Modern spectral analysis techniques for blood flow velocity and spectral measurements with pulsed Doppler ultrasound. *IEEE Transactions on Biomedical Engineering*, 38(6):589–596.

Dillon, J., Zedel, L., and Hay, A. E. (2011a). Asymptotic properties of an autocorrelation coefficient for coherent Doppler sonar. *Journal of Atmospheric and Oceanic Technology*, 28(7):966–973.

Dillon, J., Zedel, L., and Hay, A. E. (2011b). Automatic tuning of a velocity estimator for pulse-to-pulse coherent Doppler sonar. In *Proceedings of the IEEE/OES 10th Current, Waves, and Turbulence Measurement Workshop*, pages 230–236.

Dillon, J., Zedel, L., and Hay, A. E. (2011c). On the distribution of velocity measurements from pulse-to-pulse coherent Doppler sonar. *IEEE Journal of Oceanic Engineering, submitted.*

Dillon, J., Zedel, L., and Hay, A. E. (2011d). Simultaneous velocity ambiguity resolution and noise suppression for multi-frequency coherent Doppler sonar. *Journal of Atmospheric and Oceanic Technology, submitted.*

Dotti, D., Gatti, E., Svelto, V., Uggè, A., and Vidali, P. (1976). Blood flow measurements by ultrasound correlation techniques. *Energia Nucleare*, 23:571–575.

Doviak, R. J., Zrnić, D. S., and Sirmans, D. S. (1979). Doppler weather radar. *Proceedings of the IEEE*, 67(11):1522–1553.

Eilts, M. D. and Smith, S. D. (1990). Efficient dealiasing of Doppler velocities using local environment constraints. *Journal of Atmospheric and Oceanic Technology*, 7(1):118–128.

Elgar, S., Raubenheimer, B., and Guza, R. T. (2005). Quality control of acoustic Doppler velocimeter data in the surfzone. *Measurement Science and Technology*, 16(10):1889–1893.

Elsaesser, D. (2007). Sensor data fusion using a probability density grid. In *Proceedings of the 10th International Conference on Data Fusion*, pages 1–8.

Eriksson, R., Persson, H. W., Dymling, S. O., and Lindström, K. (1995). Blood perfusion measurement with multifrequency Doppler ultrasound. *Ultrasound in Medicine and Biology*, 21(1):49–57.

Fox, M. D. and Gardiner, W. M. (1988). Three-dimensional Doppler velocimetry of flow jets. *IEEE Transactions On Biomedical Engineering*, 35(10):834–841.

Franca, M. J. and Lemmin, U. (2006). Eliminating velocity aliasing in acoustic Doppler velocity profiler data. *Measurement Science and Technology*, 17(2):313–322.

Fraser, D. C. and Potter, J. E. (1969). The optimum linear smoother as a combination of two optimum linear filters. *IEEE Transactions on Automatic Control*, 14(4):387–390.

Fredsøe, J. and Deigaard, R. (1992). *Mechanics of Coastal Sediment Transport*. World Scientific Publishing.

Gao, J. and Droegemeier, K. K. (2004). A variational technique for dealiasing Doppler radial velocity data. *Journal of Applied Meteorology*, 43(6):934–940.

Garbini, J. L., Forster, F. K., and Jorgensen, J. E. (1982a). Measurement of fluid turbulence based on pulsed ultrasound techniques. Part 1. Analysis. *Journal of Fluid Mechanics*, 118:445–470.

Garbini, J. L., Forster, F. K., and Jorgensen, J. E. (1982b). Measurement of fluid turbulence based on pulsed ultrasound techniques. Part 2. Experimental investigation. *Journal of Fluid Mechanics*, 118:471–505.

Gargett, A. E. (1989). Ocean turbulence. *Annual Review of Fluid Mechanics*, 21:419–451.

Gelb, A., editor (1974). *Applied Optimal Estimation.* M.I.T. Press.

Gemmrich, J. R. and Farmer, D. M. (2004). Near-surface turbulence in the presence of breaking waves. *Journal of Physical Oceanography*, 34(5):1067–1086.

George, W. K. and Lumley, J. L. (1973). The laser-Doppler velocimeter and its application to the measurement of turbulence. *Journal of Fluid Mechanics*, 60(2):321–362.

Gibson, M. M. (1963). Spectra of turbulence in a round jet. *Journal of Fluid Mechanics*, 15(2):161–173.

Gong, J., Wang, L., and Xu, Q. (2003). A three-step dealiasing method for Doppler velocity data quality control. *Journal of Atmospheric and Oceanic Technology*, 20(12):1738–1748.

Goring, D. G. and Nikora, V. I. (2002). Despiking acoustic Doppler velocimeter data. *Journal of Hydraulic Engineering*, 128(1):117–126.

Graf, W. H. (1971). *Hydraulics of Sediment Transport.* McGraw-Hill.

Grant, W. D. and Madsen, O. S. (1986). The continental-shelf bottom boundary layer. *Annual Review of Fluid Mechanics*, 18:265–305.

Hall, D. L. and Llinas, J. (1997). An introduction to multisensor data fusion. *Proceedings of the IEEE*, 85(1):6–23.

Hashimoto, N. and Tokuda, M. (1999). A Bayesian approach for estimation of directional wave spectra from HF radar. *Coastal Engineering Journal*, 41(2):137–149.

Hay, A. E. (1991). Sound scattering from a particle-laden turbulent jet. *Journal of the Acoustical Society of America*, 90(4):2055–2074.

Hay, A. E. (2008). Near-bed turbulence and relict waveformed sand ripples: Observations from the inner shelf. *Journal of Geophysical Research*, 113(C04040), doi:10.1029/2006JC004013.

Hay, A. E. and Sheng, J. (1992). Vertical profiles of suspended sand concentration and size from multifrequency acoustic backscatter. *Journal of Geophysical Research*, 97(C10):15661–15677.

Hay, A. E., Zedel, L., Craig, R., and Paul, W. (2008). Multi-frequency, pulse-to-pulse coherent Doppler sonar profiler. In *Proceedings of the IEEE/OES 9th Working Conference on Current Measurement Technology*, pages 25–29.

Hayes, M. and Barclay, P. (2003). The effects of multipath on a bathymetric synthetic aperture sonar using belief propagation. In *Proceedings of the Image and Vision Computing NZ Conference*, pages 66–71.

Holleman, I. and Beekhuis, H. (2003). Analysis and correction of dual PRF velocity data. *Journal of Atmospheric and Oceanic Technology*, 20(4):443–453.

Hurther, D. and Lemmin, U. (2001). A correction method for turbulence measurements with a 3D acoustic Doppler velocity profiler. *Journal of Atmospheric and Oceanic Technology*, 18(3):446–458.

Hurther, D. and Lemmin, U. (2008). Improved turbulence profiling with field-adapted acoustic Doppler velocimeters using a bifrequency Doppler noise suppression method. *Journal of Atmospheric and Oceanic Technology*, 25(3):452–463.

Hussein, H. J., Capp, S. P., and George, W. K. (1994). Velocity measurements in a high-Reynolds-number, momentum-conserving, axisymmetric, turbulent jet. *Journal of Fluid Mechanics*, 258:31–75.

Jackson, D. R., Williams, K. L., Thorsos, E. I., and Kargl, S. G. (2002). High-frequency subcritical acoustic penetration into a sandy sediment. *IEEE Journal of Oceanic Engineering*, 27(3):346–361.

James, C. N. and Houze, R. A. (2001). A real-time four-dimensional Doppler dealiasing scheme. *Journal of Atmospheric and Oceanic Technology*, 18(10):1674–1683.

Jensen, J. A. (1993). Range/velocity limitations for time-domain blood velocity estimation. *Ultrasound in Medicine and Biology*, 19(9):741–749.

Joe, P. and May, P. T. (2003). Correction of dual PRF velocity errors for operational Doppler weather radars. *Journal of Atmospheric and Oceanic Technology*, 20(4):429–442.

Jones, S. A. and Krishnamurthy, K. (2002). Reduction of coherent scattering noise with multiple receiver Doppler. *Ultrasound in Medicine and Biology*, 28(5):647–653.

Kalman, R. E. (1960). A new approach to linear filtering and prediction problems. *Transactions of the ASME. Series D, Journal of Basic Engineering*, 82:35–45.

Kay, S. M. (1993). *Fundamentals of Statistical Signal Processing: Estimation Theory*, volume 1. Prentice-Hall PTR.

Kraeutner, P. H. and Bird, J. S. (1999). Beyond interferometry, resolving multiple angles-of-arrival in swath bathymetric imaging. In *Proceedings of the OCEANS MTS/IEEE Conference: Riding the Crest into the 21st Century*, pages 37–45.

Kraus, N. C., Lohrmann, A., and Cabrera, R. (1994). New acoustic meter for measuring 3D laboratory flows. *Journal of Hydraulic Engineering*, 120(3):406–412.

Lane, S. N., Biron, P. M., Bradbrook, K. F., Butler, J. B., Chandler, J. H., Crowell, M. D., McLelland, S. J., Richards, K. S., and Roy, A. G. (1998). Three-dimensional measurement of river channel flow processes using acoustic Doppler velocimetry. *Earth Surface Processes and Landforms*, 23(13):1247–1267.

Lemmin, U. and Rolland, T. (1997). Acoustic velocity profiler for laboratory and field studies. *Journal of Hydraulic Engineering*, 123(12):1089–1098.

Lhermitte, R. (1983). Doppler sonar observation of tidal flow. *Journal of Geophysical Research*, 88(C1):725–742.

Lhermitte, R. and Lemmin, U. (1994). Open-channel flow and turbulence measurement by high-resolution Doppler sonar. *Journal of Atmospheric and Oceanic Technology*, 11(5):1295–1308.

Lhermitte, R. and Serafin, R. (1984). Pulse-to-pulse coherent Doppler sonar signal processing techniques. *Journal of Atmospheric and Oceanic Technology*, 1(4):293–308.

Lisle, T. E. (1989). Sediment transport and resulting deposition in spawning gravels, north coastal California. *Water Resources Research*, 25(6):1303–1319.

Lohrmann, A., Hackett, B., and Røed, L. P. (1990). High resolution measurements of turbulence, velocity and stress using a pulse-to-pulse coherent sonar. *Journal of Atmospheric and Oceanic Technology*, 7(1):19–37.

Lu, Y. and Lueck, R. G. (1999a). Using a broadband ADCP in a tidal channel. Part I: Mean flow and shear. *Journal of Atmospheric and Oceanic Technology*, 16(11):1556–1567.

Lu, Y. and Lueck, R. G. (1999b). Using a broadband ADCP in a tidal channel. Part II: Turbulence. *Journal of Atmospheric and Oceanic Technology*, 16(11):1568–1579.

Luenberger, D. G. (1969). *Optimization by Vector Space Methods.* John Wiley & Sons.

Marple, L. (1980). A new autoregressive spectrum analysis algorithm. *IEEE Transactions on Acoustics, Speech, and Signal Processing*, ASSP-28(4):441–454.

McNutt, M. (2002). Ocean exploration. *Oceanography*, 15(1):112–121.

Medwin, H. and Clay, C. S. (1998). *Fundamentals of Acoustical Oceanography.* Academic Press.

Meinhold, R. J. and Singpurwalla, N. D. (1983). Understanding the Kalman filter. *The American Statistician*, 37(2):123–127.

Menzies, R. T. and Hardesty, R. M. (1989). Coherent Doppler lidar for measurements of wind fields. *Proceedings of the IEEE*, 77(3):449–462.

Miller, K. S. and Rochwarger, M. M. (1972). A covariance approach to spectral moment estimation. *IEEE Transactions on Information Theory*, IT-18(5):588–596.

Mitra, S. K. (1998). *Digital Signal Processing: A Computer-Based Approach.* McGraw-Hill.

Mo, L. Y. L. and Cobbold, R. S. C. (1992). A unified approach to modeling the backscattered Doppler ultrasound from blood. *IEEE Transactions on Biomedical Engineering*, 39(5):450–461.

Mohamed, M. H. and LaRue, J. C. (1990). The decay power law in grid-generated turbulence. *Journal of Fluid Mechanics*, 219:195–214.

National Oceanic and Atmospheric Administration (2000). Discovering Earth's final frontier: A U.S. strategy for ocean exploration. `http://explore.noaa.gov/`

media/http/pubs/pres_panel_rpt.pdf. The Report of the President's Panel on Ocean Exploration.

Newgard, J. P. and Hay, A. E. (2007). Turbulence intensity in the wave boundary layer and bottom friction under (mainly) flat bed conditions. *Journal of Geophysical Research*, 112(C09024), doi:10.1029/2006JC003881.

Newhouse, V. L. and Amir, I. (1983). Time dilation and inversion properties and the output spectrum of pulsed Doppler flowmeters. *IEEE Transactions On Sonics and Ultrasonics*, 30(3):174–179.

Nielsen, P. (1992). *Coastal Bottom Boundary Layers and Sediment Transport.* World Scientific Publishing.

Nitzpon, H. J., Rajaonah, J. C., Burckhardt, C. B., Dousse, B., and Meister, J. J. (1995). A new pulsed wave Doppler ultrasound system to measure blood velocities beyond the Nyquist limit. *IEEE Transactions on Ultrasonics, Ferroelectrics, and Frequency Control*, 42(2):265–279.

Nobach, H. and Honkanen, M. (2005). Two-dimensional Gaussian regression for sub-pixel displacement estimation in particle image velocimetry or particle position estimation in particle tracking velocimetry. *Experiments in Fluids*, 38(4):511–515.

Nortek (2009). *Vectrino Velocimeter User Manual.* http://www.nortek-as.com/en/support/manuals.

Panchapakesan, N. R. and Lumley, J. L. (1993). Turbulence measurements in axisymmetric jets of air and helium. Part 1. Air jet. *Journal of Fluid Mechanics*, 246:197–223.

Pearl, J. (1986). Fusion, propagation, and structuring in belief networks. *Artificial Intelligence*, 29(3):241–288.

Petrovic, N., Cohen, I., Frey, B. J., Koetter, R., and Huang, T. S. (2001). Enforcing integrability for surface reconstruction algorithms using belief propagation in graphical models. In *Proceedings of the IEEE Computer Society Conference on Computer Vision and Pattern Recognition*, volume 1, pages I–743–I–748.

Pierce, A. D. (1989). *Acoustics: An Introduction to Its Physical Principles and Applications*. Acoustical Society of America.

Plueddemann, A. J. (1992). Internal wave observations from the Arctic environmental drifting buoy. *Journal of Geophysical Research*, 97(C8):12619–12638.

Rabiner, L. R. and Juang, B. H. (1986). An introduction to hidden Markov models. *IEEE ASSP Magazine*, 3(1):4–16.

Raffel, M., Willert, C. E., Wereley, S. T., and Kompenhans, J. (2007). *Particle Image Velocimetry: A Practical Guide*. Springer, second edition.

Rippeth, T. P., Williams, E., and Simpson, J. H. (2002). Reynolds stress and turbulent energy production in a tidal channel. *Journal of Physical Oceanography*, 32(4):1242–1251.

Rowe, F. D., Deines, K. L., and Gordon, R. L. (1986). High resolution current profiler. In *Proceedings of the IEEE 3rd Working Conference on Current Measurement*, volume 3, pages 184–189.

Sachidananda, M. and Zrnić, D. S. (1999). Systematic phase codes for resolving range overlaid signals in a Doppler weather radar. *Journal of Atmospheric and Oceanic Technology*, 16(10):1351–1363.

Scotti, A. and Pineda, J. (2004). Observation of very large and steep internal waves of elevation near the Massachusetts coast. *Geophysical Research Letters*, 31(L22307), doi:10.1029/2004GL021052.

Shalash, S. (1982). Effects of sedimentation on the storage capacity of the High Aswan Dam reservoir. *Hydrobiologia*, 92(1):623–639.

Sirmans, D. and Bumgarner, B. (1975). Numerical comparison of five mean frequency estimators. *Journal of Applied Meteorology*, 14(6):991–1003.

Smyth, C. and Hay, A. E. (2003). Near-bed turbulence and bottom friction during SandyDuck97. *Journal of Geophysical Research*, 108(C6), 3197, doi:10.1029/2001JC000952.

Smyth, C., Hay, A. E., and Zedel, L. (2002). Coherent Doppler profiler measurements of near-bed suspended sediment fluxes and the influence of bed forms. *Journal of Geophysical Research*, 107(C8), 3105, doi:10.1029/2000JC000760.

Souza, A. J., Alvarez, L. G., and Dickey, T. D. (2004). Tidally induced turbulence and suspended sediment. *Geophysical Research Letters*, 31(L20309), doi:10.1029/2004GL021186.

Stacey, M. T., Monismith, S. G., and Burau, J. R. (1999). Measurements of Reynolds stress profiles in unstratified tidal flow. *Journal of Geophysical Research*, 104(C5):10933–10949.

Tabray, P., Scialom, G., and Germann, U. (2001). Real-time retrieval of the wind from aliased velocities measured by Doppler radars. *Journal of Atmospheric and Oceanic Technology*, 18(6):875–882.

Taylor, G. I. (1935a). Statistical theory of turbulence – I. *Proceedings of the Royal Society of London. Series A, Mathematical and Physical Sciences*, 151(873):421–444.

Taylor, G. I. (1935b). Statistical theory of turbulence – II. *Proceedings of the Royal Society of London. Series A, Mathematical and Physical Sciences*, 151(873):444–454.

Thomas, N. and Leeman, S. (1993). The double Doppler effect. In *Proceedings of the 1993 International Conference on Acoustic Sensing and Imaging*, pages 164–168.

Thorne, P. D. and Hanes, D. M. (2002). A review of acoustic measurement of small-scale sediment processes. *Continental Shelf Research*, 22(4):603–632.

Torp, H. and Kristoffersen, K. (1995). Velocity matched spectrum analysis: A new method for suppressing velocity ambiguity in pulsed-wave Doppler. *Ultrasound in Medicine and Biology*, 21(7):937–944.

Tortoli, P. (1989). A tracking FFT processor for pulsed Doppler analysis beyond the Nyquist limit. *IEEE Transactions on Biomedical Engineering*, 36(2):232–237.

Trowbridge, J. and Elgar, S. (2001). Turbulence measurements in the surf zone. *Journal of Physical Oceanography*, 31(8):2403–2417.

Umlauf, L. and Lemmin, U. (2005). Interbasin exchange and mixing in the hypolimnion of a large lake: The role of long internal waves. *Limnology and Oceanography*, 50(5):1601–1611.

Urick, R. J. (1983). *Principles of Underwater Sound.* McGraw-Hill, third edition.

Vaitkus, P. J. and Cobbold, R. S. C. (1988). A comparative study and assessment of Doppler ultrasound spectral estimation techniques. Part I: Estimation methods. *Ultrasound in Medicine and Biology*, 14(8):661–672.

Vaitkus, P. J., Cobbold, R. S. C., and Johnston, K. W. (1988). A comparative study and assessment of Doppler ultrasound spectral estimation techniques. Part II: Methods and results. *Ultrasound in Medicine and Biology*, 14(8):673–688.

Van Rijn, L. C. (1984). Sediment pick-up functions. *Journal of Hydraulic Engineering*, 110(10):1494–1502.

Van Rijn, L. C. (2007). *Manual Sediment Transport Measurements in Rivers, Estuaries, and Coastal Seas.* Delft Hydraulics Laboratory.

Veron, F. and Melville, W. K. (1999). Pulse-to-pulse coherent Doppler measurements of waves and turbulence. *Journal of Atmospheric and Oceanic Technology*, 16(11):1580–1597.

Voulgaris, G. and Trowbridge, J. H. (1998). Evaluation of the acoustic Doppler velocimeter (ADV) for turbulence measurements. *Journal of Atmospheric and Oceanic Technology*, 15(1):272–289.

Westerweel, J., Dabiri, D., and Gharib, M. (1997). The effect of a discrete window offset on the accuracy of cross-correlation analysis of digital PIV recordings. *Experiments in Fluids*, 23(1):20–28.

Westerweel, J., Hofmann, T., Fukushima, C., and Hunt, J. C. R. (2002). The turbulent/non-turbulent interface at the outer boundary of a self-similar turbulent jet. *Experiments in Fluids*, 33(6):873–878.

Williams, J. J., Bell, P. S., Humphrey, J. D., Hardcastle, P. J., and Thorne, P. D. (2003). New approach to measurement of sediment processes in a tidal inlet. *Continental Shelf Research*, 23(14-15):1239–1254.

Woodman, R. F. and Hagfors, T. (1969). Methods for the measurement of vertical ionospheric motions near the magnetic equator by incoherent scattering. *Journal of Geophysical Research*, 74(5):1205–1212.

Wygnanski, I. and Fiedler, H. (1969). Some measurements in the self-preserving jet. *Journal of Fluid Mechanics*, 38(3):577–612.

York, G. and Kim, Y. (1999). Ultrasound processing and computing: Review and future directions. *Annual Review of Biomedical Engineering*, 1:559–588.

Zedel, L. (2008). Modeling pulse-to-pulse coherent Doppler sonar. *Journal of Atmospheric and Oceanic Technology*, 25(10):1834–1844.

Zedel, L. and Hay, A. E. (1999). A coherent Doppler profiler for high-resolution particle velocimetry in the ocean: Laboratory measurements of turbulence and particle flux. *Journal of Atmospheric and Oceanic Technology*, 16(8):1102–1117.

Zedel, L. and Hay, A. E. (2002). A three-component bistatic coherent Doppler velocity profiler: Error sensitivity and system accuracy. *IEEE Journal of Oceanic Engineering*, 27(3):717–725.

Zedel, L. and Hay, A. E. (2010). Resolving velocity ambiguity in multifrequency, pulse-to-pulse coherent Doppler sonar. *IEEE Journal of Oceanic Engineering*, 35(4):847–851.

Zedel, L., Hay, A. E., Cabrera, R., and Lohrmann, A. (1996). Performance of a single-beam pulse-to-pulse coherent Doppler profiler. *IEEE Journal of Oceanic Engineering*, 21(3):290–297.

Zhang, J., Rose, J. L., and Shung, K. K. (1994). A computer model for simulating ultrasonic scattering in biological tissues with high scatterer concentration. *Ultrasound in Medicine and Biology*, 20(9):903–913.

Zhang, Z., Jakobsson, A., Nikolov, S., and Chambers, J. A. (2004). A novel velocity estimator using multiple frequency carriers. In *Proceedings of the SPIE Medical Imaging 2004: Ultrasonic Imaging and Signal Processing*, pages 281–289.

Zhang, Z., Jakobsson, A., Nikolov, S., and Chambers, J. A. (2005). Extending the unambiguous velocity range using multiple carrier frequencies. *Electronics Letters*, 41(22):1206–1208.

Zrnić, D. S. (1977). Spectral moment estimates from correlated pulse pairs. *IEEE Transactions on Aerospace and Electronic Systems*, AES-13(4):344–354.